University of Strathclyde
Department of Mechanical Engineering

Modelling and simulation of droplet dynamics in microfluidic devices

Haihu Liu

A thesis presented in fulfilment of the requirements
for the degree of Doctor of Philosophy

2010

Declaration of Author's Rights

This thesis is the result of the author's original research. It has been composed by the author and has not been previously submitted for examination which has led to the award of a degree.

Abstract

Manipulation of microscopic droplets in microfluidic devices is important to many research areas and associated industries such as pharmaceutical and chemical industries. Many underlying mechanisms for droplet formation, transportation and interactions with other droplets or surface are still poorly understood, theoretical models and numerical simulations are urgently required to improve our knowledge of droplet behavior in microdevices. In recent years, the lattice Boltzmann method (LBM) has emerged as a novel numerical method for multiphase flow simulations. It is built upon the resolution of physics at a mesoscopic level and thus can provide many advantages of molecular dynamics while having many favorable features such as simplification of nonlinear modeling, computational efficiency and accuracy, and the capability of dealing with complex boundaries. In this thesis, the lattice Boltzmann phase-filed models are developed and applied to investigate the droplet dynamical behavior in microfluidic systems with and without surfactants, with the focuses on the influence of physical parameters on droplet formation in confined microchannels, and how the surfactant adsorption influences the droplet deformation, breakup and coalescence.

First, we present an improved lattice Boltzmann model for a binary fluid, using the phase-field theory to describe the interfacial interactions, with the purpose of reducing the spurious velocities and easily incorporating the wetting boundary conditions. After extensive model analysis and validations, the model is applied to simulate the droplet formation in a microfluidic T-junction. The influence of capillary number, flow rate ratio, viscosity ratio and contact angle is systematically examined in the droplet generation process. Regardless of flow rate ratio, viscosity ratio and contact angle, it is clearly observed that the transition from the squeezing regime to the dripping regime occurs at a critical capillary number of 0.018. In the squeezing regime, the squeezing pressure plays a dominant role in the droplet breakup process, which arises when the emerging interface obstructs the main channel. The droplet size depends on both the capillary number and the flow rate ratio, but is independent of the viscosity ratio under completely hydrophobic wetting conditions. In the dripping regime, the droplet size is significantly influenced by the viscosity ratio as well as the built-up squeezing pressure. When the capillary number increases, the droplet size becomes less dependent on

the flow rate ratio. The contact angle also affects the droplet shape, size and detachment point, especially at small capillary numbers. More hydrophobic wetting properties are expected to produce smaller droplets. Interestingly, the droplet size is dependent on the viscosity ratio only for less hydrophobic wetting conditions.

Considering the difference in channel geometry, the numerical simulations are also performed to understand the dynamics of droplet formation in a microfluidic cross-junction. Two different regimes, namely the squeezing-like regime and the dripping regime, are clearly identified with the transition occurring at a critical capillary number $Ca_{cr} = 0.01$. Generally, large flow rate ratio is expected to produce big droplets, while increasing capillary number will reduce droplet size. In the squeezing-like regime ($Ca \leq Ca_{cr}$), droplet breakup process is dominated by the squeezing pressure and the viscous force. The droplet size exhibits a power-law dependence on the capillary number with the power-law exponent independent of the flow rate ratio. In the dripping regime ($Ca > Ca_{cr}$), the viscous force is dominant and the droplet size becomes quickly independent of the flow rate ratio as the capillary number increases. In addition, the droplet size weakly depends on the viscosity ratio in both regimes and decreases when the viscosity of the continuous phase increases. Finally, a scaling law is established to predict the droplet size.

It has been found by a number of experiments that the presence of surfactants can significantly affect the droplet dynamical behavior in a microfluidic system. A lattice Boltzmann phase-field model, with a generalized free energy functional to describe the system, is proposed for simulating droplet motion with soluble surfactants. The model can recover the Langmuir and Frumkin adsorption isotherms in equilibrium. From the equilibrium equation of state, one can determine the interfacial tension lowering scale according to the interface surfactant concentration. The model is able to capture short-time and long-time adsorption dynamics of surfactants. The model is also applied to examine the effect of soluble surfactants on droplet deformation, breakup and coalescence. The increase of surfactant concentration and attractive lateral interaction can enhance droplet deformation, promote droplet breakup, and inhibit droplet coalescence. We also demonstrate that the Marangoni stresses can reduce the interface mobility and slow down the film drainage process, thus acting as an additional repulsive force to prevent the droplet coalescence.

Acknowledgements

First of all, I would like to express my sincere gratitude to my supervisor Dr. Yonghao Zhang for continuously inspiring me to approach new problems, overcome challenges and for allowing me the freedom and confidence to explore the research topics that I am interested in. It was his unwavering support and faith in my work that helped me to successfully complete my research and made this challenging journey a smooth and memorable one. Dr. Zhang has served as a true mentor—as much in my academic activities, as in the non-academic ones. I also owe a debt of gratitude to Dr. Jianping Meng and Dr. Guihua Tang for their instructions and valuable discussions.

I am indebted to Prof. Jason Reese and Dr. Tom Scanlon for their suggestions and kind help. I would also like to thank the other members in my research group. Particularly, I would like to thank Abdul Ahmad for his assistance in my study and life in Glasgow.

The help and friendship from Dr. Hongjun Li, Dr. Jun Hong, Dr. He Zheng, Liu Yang and Haizhen Liu have made my study and life in Glasgow a joyful experience. Thank you for being my family in Glasgow and thank you for all the wonderful memories. I hope this is only the beginning of our life-long friendships.

I would like to thank SORSAS and the University of Strathclyde for the financial support throughout my Ph.D programme.

Finally I would like to thank, from the bottom of my heart, my family for their everlasting love, understanding and encouragement.

Contents

List of Figures

Nomenclature

Greek symbols

α	Fitting parameter; also parameter in equilibrium equation of state
β	Fitting parameter; also surfactant concentration ratio in the oil and water bulk phases
$\Delta\rho$	Density difference between the dispersed phase and the continuous phase
$\Delta\sigma$	Interfacial tension lowering due to surfactant adsorption
δf	Mass modification for rest particle distribution function
Δp	Pressure difference across the droplet interface
δ_t	Lattice grid size
δ_x	Lattice time step
$\delta_{\alpha\beta}$	Kronecker delta ($\boldsymbol{I}$ in subscript form)
ϵ	Small parameter in Chapman-Enskog expansion
η	Fluid dynamic viscosity
Γ	Dimensionless constant related to mobility M
γ	Shear rate
κ	Interface curvature; also parameter related to the interfacial tension in the phase-field model
Λ	Dispersed-to-continuous channel width ratio
λ	Viscosity ratio
λ_w	Wavelength of the capillary wave
μ	Chemical potential
μ_ϕ	Chemical potential for order parameter ϕ

μ_ψ	Chemical potential for surfactant concentration ψ
ν	Kinematic viscosity
ϕ	Order parameter
ϕ_w	Order parameter at solid wall
$\Pi^{(1)}_{\alpha\beta}$	Non-equilibrium stress tensor at the first order
Ψ	Bulk free energy density for a homogeneous system
ψ	Surfactant concentration
ψ_s	Surfactant concentration at the subsurface
ψ_{eq}	Equilibrium surfactant concentration at the interface, which is derived from the Frumkin adsorption isotherm
ρ	Density
σ	Interfacial tension
σ_0	Interfacial tension of a “clean” droplet $= 4\kappa\phi_b^2/3\xi$
σ_e	Effective interfacial tension for a stationary droplet at equilibrium
τ	Time; also nondimensional time defined in Ward and Tordai problem
τ_f, τ_g, τ_h	Relaxation parameters in lattice Boltzmann equations
θ	Droplet inclination angle
θ_A	Advancing contact angle
θ_R	Receding contact angle
θ_w	Equilibrium contact angle
ε	Parameter dependent on the geometry of the channel
ξ	Measure for the thickness of diffuse interface
w_i	Weight factor with $\vec{e}_i$

Latin symbols

$\bar{b}$	Dimensionless length of the emerging droplet
$\bar{d}$	Droplet diameter scaled by the inner diameter of the capillary tube
$\bar{l}$	Dimensionless length of droplet $= \frac{l}{w_c}$

$\boldsymbol{I}$	Second order unit tensor
$\boldsymbol{P}$	Pressure tensor in Navier-Stokes equation
Γ_ϕ, Γ_ψ	Dimensionless constants related to mobilities M_ϕ, M_ψ
$\tilde{f}_i$	Intermediate distribution functions in deriving stress-free boundary conditions
$\vec{e}_i$	Lattice velocity (vector) set
$\vec{F}_S$	Interfacial force vector $= \mu \nabla \phi$
$\vec{f}_V$	Thermodynamic force vector
$\vec{j}_\psi$	Surfactant flux
$\vec{u}$	Velocity vector
$\vec{x}$	Spatial coordinates
A	Cross-sectional area of the channel; also coefficient controlling the interaction energy between two fluids
a	Major axis of an ellipse
A_i, B_i, F_i, G_i, H_i	Coefficients in equilibrium distribution functions
B	Coefficient in bulk free energy density
b	Minor axis of an ellipse
Bo	Bond number
C	Volume fraction of one of the fluid phases or components; also coefficient of attractive lateral interaction
c	Lattice speed
c_s	Lattice speed of sound
Ca	Capillary number
Ca_e	Effective capillary number defined by σ_e
D	Coefficient of the nonlocal coupling term $\psi(\nabla\phi)^2$ in free energy
d	Horizontal gap of two droplets; also droplet diameter
d_c	Characteristic diameter of the T-shaped microchannel
d_i	Inner diameter of the capillary tube

D_ϕ	Interface diffusivity
D_ψ	Surfactant diffusion coefficient in the bulk phase
$D_{H,c}$	Hydraulic diameter of the continuous-phase channel
Df	Taylor deformation parameter
E	Coefficient of the asymmetric term $\psi\phi$ in free energy
Ex	Dimensionless number defined by $Ex = \frac{D}{W\xi^2}$
f	Free energy density
f_i'	Post-collision particle distribution function for f_i
F_i	Interfacial force distribution along $\vec{e}_i$ in the lattice space
f_i	Particle distribution function with $\vec{e}_i$ for ρ, $\vec{u}$
$f_i^{(1)}$	Particle distribution function at the first order for f_i
$f_i^{(2)}$	Particle distribution function at the second order for f_i
f_i^{eq}	Equilibrium distribution function of f_i
G	Shear rate
g	Magnitude of gravity acceleration
g_i'	Post-collision particle distribution function for g_i
g_i	Particle distribution function with $\vec{e}_i$ for ϕ
$g_i^{(1)}$	Particle distribution function at the first order for g_i
$g_i^{(2)}$	Particle distribution function at the second order for g_i
g_i^{eq}	Equilibrium distribution function of g_i
H	Channel height
h	Depth of microfluidic geometries
h_i	Particle distribution function with $\vec{e}_i$ for ψ
h_i^{eq}	Equilibrium distribution function of h_i
K	Constant
k	Fitting parameter
k_B	Boltzmann constant

L	Characteristic length of a microfluidic geometry
l	Droplet length
L_0	Length scale for conversion between lattice units and physical units
l_s	Effective slip length at the three phase contact line
L_{ad}	Adsorption length of surfactants
M	Mobility in Cahn-Hilliard equation
m	Fitting constant
m	Outgoing mass distribution at the outflow boundary
M_0	Mass scale for conversion between lattice units and physical units
m_s	Total mass of surfactants in a closed finite domain
M_ϕ, M_ψ	Mobilities for ϕ and ψ in Cahn-Hilliard equations
m_{tot}	Total net flux at the inflow boundary
Ma	Mach number
n	Fitting constant
p	Pressure
p_0	Scalar part of the pressure tensor
Pe	Peclet number based on the characteristic length of the system
Pe_ϕ	Peclet number defined by ξ
Pe_ψ	Peclet number associated with the Cahn-Hilliard equation for surfactant concentration
Q	Volumetric flow rate; also flow rate ratio
R	Droplet radius
r	Distance away from the droplet center
Re	Reynolds number
T	Temperature; also dimensionless time used for the droplet formation in the cross-junction
t	Time
T_0	Time scale for conversion between lattice units and physical units

U	Magnitude of flow velocity
u	Velocity
u_d	Droplet velocity in x-direction under steady state
u_w	Velocity of the upper wall in the study of a shear driven droplet
u_x	Velocity component along x-direction
V	Droplet volume; also velocity
W	Coefficient of the term $\psi^2\phi^2$ ($\psi\phi^2$) in free energy
w	Excess free energy per unit interface area
w	Inlet channel width
w_m	Neck width of droplet
We	Weber number
x	x-coordinate; also spatial coordinate normal to the interface
X_c, Y_c	(Initial) Droplet centre position
y	y-coordinate
z	spatial coordinate normal to the interface

Mathematical operators

$\frac{\mathrm{d}}{\mathrm{d}z}$	First order derivative with respect to the spatial coordinate z
$\mathcal{O}()$	Order of ()
$\nabla\cdot$	Divergence operator
∇	Gradient operator
$\nabla^2/\partial_{\alpha\alpha}$	Laplacian operator
∂_t	Partial derivative with respect to time
∂_α	Partial derivative with respect to the spatial coordinate x_α
∂_{t_0}	Partial derivative with respect to time at the zeroth order
∂_{t_1}	Partial derivative with respect to time at the first order
$\sum_i$	Summation over the discrete velocity directions
$^{\mathrm{T}}$	Matrix transpose

Other symbols

$\mathscr{F}$	Free energy functional
$N(\phi)$	A function defined to calculate the averages

Superscripts

eq	Equilibrium
phy	Physical unit
$+$, -	Oil and water bulk phases

Subscripts

0	Interface
α, β, γ	Indices for spatial coordinates
c	Continuous phase; also critical
cl	Contact line
cr	Critical
d	Dispersed phase
i	Index of the lattice velocity
in	Inlet
max	Maximum
min	Minimum
n	Necking
o	Oil
ref	Reference
S	Static
tot	Total
w	Water; also wall

Chapter 1

Introduction

1.1 Background

Microfluidics is a research area that studies dynamics of fluids that are geometrically restricted to small, typically sub-millimeter scales. It has developed rapidly since the 1980s. Historically, the first applications of microfluidics were initiated by the generalization of ink jet printing, and also to some extent by space applications, in which droplets are used to feed micro-motors. Today, rapid development of microfabrication technologies has facilitated a broad range of microfluidic applications especially in biological and chemical analysis/synthesis and associated industries. Microdroplet technology has recently emerged as a promising flexible platform for microfluidic functions. As samples/reagents are confined in the droplets so that sample dilution caused by Taylor dispersion [1] can be avoided, and mixing performance can be improved [2]. In addition, it can avoid sample/surface interaction and thus eliminate surface adsorption and cross sample contamination. The miniaturization of the entire process enables the rapid analysis of very small quantities of droplet samples in a portable, automated and inexpensive format [3]. Recently, microdroplet technology has enabled droplets to be used as microreactors for chemical analysis and protein crystallization [4,5], as molds for curing polymeric microspheres [6, 7]. Furthermore, programmable fluidic assays for sampling glucose concentration of human physiological fluids [8] and DNA analysis [9] have been individually demonstrated using a microdroplet system. For all these applications, it is crucial to control and predict the flow behavior. Unlike in conventional devices, droplets rarely coalesce with each other in microfluidic systems. So the flow behavior is mainly located in the region where various phases meet. In other words, all the important phenomena occur in the region of the droplet formation.

Over the past few years, numerous experiments have highlighted the advances being made in the field of droplet formation using a variety of microfluidic devices, including geometry-dominated devices [10, 11], flow-focusing devices [12–16], T-junctions based on cross-flowing rupturing technique [17–23] and co-flowing devices [24, 25]. Due to the small length scales involved, the flow of the dissimilar fluids falls in the laminar regime, which enables a higher degree of control of the droplet generation process. The large surface area to volume ratio enhances the role of surface effects. These unique characteristics can offer broad prospects in the development of novel applications exploiting the benefits of miniaturization. However, the droplet dynamics in microfluidic devices is very complicated. Many coupled factors will affect the droplet generation, transportation and interaction, e.g. the interfacial tension, the wetting properties of solid walls, the confinement of channel geometry, the flow rates of both fluids and their viscosities. In order to gain a full understanding of flow physics and thus improve designs of microfluidic devices, it is essential to have comprehensive studies of such multiphase systems.

Although significant efforts have been made to understand the underlying mechanisms of droplet generation, transportation and interaction in these confined microfluidic geometries, the currently available experimental data are still sporadic. Various materials are used to fabricate the channels with different dimensions, while the experiments are operated under a wide range of flow conditions with different fluids. Consequently, the information is fragmented, which leads to inconclusive and even contradictory findings. In addition, experiments at such small scale are still difficult. For example, it is challenging to accurately measure droplet size, pressure and velocity fields, and droplet deformation, breakup, and coalescence. As the surfactants are deliberately introduced into the microfluidic system to keep the droplets stable, it is impractical to dynamically measure the local surfactant concentration or interfacial tension. Theoretical approaches (e.g. lubrication theories) can only describe the limiting droplet behavior (e.g. pinching or film-drainage rates) of the geometrical and field variables at the onset of breakup and coalescence transitions based on simplified assumptions on geometry (e.g. one-dimensionality), fluid and flow conditions. Direct numerical simulations can accurately simulate the droplet dynamics in principle without relying upon simplifying assumptions, and provide more detailed information on various factors which influence the droplet behavior, and their interactions. Hopefully, deeper insights into the mechanisms will be gained at a lower cost especially with the fast development of computing power.

To numerically simulate the droplet dynamics in microfluidic devices, typically, either an interface-tracking or an interface-capturing method is applied. In these approaches, the multiphase flows are usually simulated by solving the Navier-Stokes equations coupled with a scalar equation to track or capture the interface. Interface-tracking methods are not suitable for simulating droplet breakup and coalescence, because the interface must be manually ruptured based upon some ad-hoc criteria [26]. Interface-capturing methods can naturally deal with droplet breakup and coalescence. Among these methods, the volume-of-fluid (VOF) and the level set method are most common. Both of them solve a pure advection equation for the interface in the Eulerian frame. However, the interface reconstruction is required in VOF to determine the interfacial tension force and calculate the flux across the interface. This process can be time-consuming and not always physically consistent [28]. Also, most of the VOF interface reconstruction schemes only have first order of accuracy. The level set method uses a signed distance function to represent the interface. It requires a re-initialization procedure to keep the distance property when large topological changes occur around the interface. This may violate the mass conservation for each phase or component. In addition, VOF and level set methods will experience numerical instability at the interface region when the interfacial tension is dominant in interfacial dynamics for small droplets [27]. As to the modelling the fluid-surface interactions, VOF and level set methods often rely on explicitly finding the interface position and impose the contact angle or some sophisticated predetermined model on the interface near the wall surface, which usually has little physical basis or needs a complicated numerical scheme.

Surfactant molecules typically consist of a hydrophilic head and a hydrophobic tail. They accumulate at the fluid interfaces forming a buffer zone between the continuous phase fluid and the droplet fluid molecules, thereby lowering the interfacial tension. In the droplet formation, surfactants can increase the droplet stability and are also a means of modifying the surface properties which can result in control of which phase will constitute the dispersed and continuous phase. Besides, the addition of surfactants can also result in better monodispersity, this is due to a more focused point of necking of the liquid thread entering the main channel. These benefits have enabled the surfactants to be widely used in numerous important scientific and engineering applications [29–31]. Computational modelling interfacial dynamics with soluble surfactants in a multiphase system is a daunting task, because the interaction between the surfactants and the flowfield is highly non-linear. Most previous numerical work on surfactants has utilized the sharp interface models with an equilibrium equation of state relating dynamic interfacial tension to local surfactant concentration, which require complicated algorithms and extremely high computational cost. Also, these methods are all built upon the conservation laws at the macroscopic level, which have been developed from the original model proposed by Stone and Leal [32]. Although these methods have been successfully applied to simulate interfacial flows in a ternary system, i.e. oil/water emulsions with surfactants, they commonly suffer from several drawbacks: (i) dynamic interfacial tension relies on an asserted equilibrium equation of state, which is also assumed to be valid beyond the equilibrium states; (ii) for interfacial flows with soluble surfactants, mass transfer between the interface and the bulk fluids requires an external boundary condition, which cannot uniquely arise from the model itself; (iii) model extension for more complicated systems, such as ionic surfactant solutions, is not easy [33]; (iv) numerical stability becomes a serious challenge for the flows with large topological changes, such as droplet breakup and coalescence.

As one of the interface-capturing methods, the phase-field method resolves the interface structure via an appropriate free energy functional based on Cahn-Hilliard theory [81]. Interfacial events evolve naturally based on the minimization of the interface free energy and the interface sharpness is preserved automatically. The numerical solution does not suffer from the drawbacks of other interface-capturing methods, such as interface reconstruction, re-initialization and mass loss, and thus it does not require additional algorithms to correct interface features or to remove oscillations. Meanwhile, the smooth representation of the interface as a transition region prevents the numerical difficulties caused by the interface singularities. Therefore, the droplet breakup, coalescence and the contact line dynamics can be modelled with much ease in the phase-field model. It also allows stable discretization of the gradient terms in the interfacial tension force in momentum equations, which provides a numerical advantage in dealing with small droplets in comparison with VOF and level set methods. As a mesoscopic-level model, phase-field model provides the flexibility of using a free energy based description to model complex material properties and the interaction between these materials. This is of great potential for modelling the interfacial flows with surfactants. Due to these notable features, we aim to develop phase-field models to describe and understand the droplet dynamics in microfluidic devices. The phase-field models will be solved using a recently developed computational approach, i.e. the lattice Boltzmann method (LBM). LBM is a pseudo-molecular method tracking evolutions of the distribution function of an assembly of molecules and built upon microscopic models and mesoscopic kinetic equations. Due to its kinetic nature, the LBM has several advantages over the traditional computational fluid dynamics (CFD) methods: reduction from second order to first order partial equations, simplification of nonlinear modelling, computational efficiency and accuracy, simple fluid interface boundary conditions, and a mathematical framework allowing molecular level modelling. Therefore, the LBM has developed to be a very efficient numerical tool to simulate the droplet dynamics in microfluidic devices in which the interface between different phases and the contact line dynamics on the solid surface are essentially at the mesoscopic level [34], bridging the gap between the microscopic molecular world to the macroscopic hydrodynamics.

1.2 Objectives

To describe a binary fluid, the free energy model proposed by Swift et al. [35] violates the Galilean invariance, produces large spurious velocities near the interface, and can lead to incorrect prediction for the equilibrium contact angle when both fluids have different viscosities [36]. To overcome these limitations, an improved LB phase-field model will be proposed to simulate the binary fluid with a simple wetting boundary treatment. It has been found theoretically and experimentally that the droplet dynamical behavior can be characterized by some dimensionless parameters in microfluidic devices. The improved lattice Boltzmann model will be applied to investigate the influence of these dimensionless parameters on the droplet formation in a microfluidic T-junction and cross-junction, respectively. The simulation results will be qualitatively and quantitatively compared with some existing experimental and simulation results with some scaling models examined. Using the traditional CFD methods for soluble surfactants is challenging and has a few major shortcomings. Due to its intrinsic physics basis, the phase-field model has shown promise to model and simulate the interfacial flows with surfactants. However, significant effort is still required to improve this model for a realistic oil/water/surfactants system. We will present a generalized phase-field model in the framework of LBM to simulate the adsorption of surfactants at the interface and its effect on the droplet dynamics. In summary, the objectives of this thesis mainly are:

1. Establishing an improved LB phase-field model for a binary fluid;
2. Investigating the droplet formation in a microfluidic T-junction and a cross-junction and identifying the breakup mechanisms of droplets in confined geometries;
3. Developing a generalized phase-field model for interfacial flows with soluble surfactants, and understanding the role of surfactants in droplet deformation, breakup and coalescence.

1.3 Outline of thesis

In Chapter 2, we will first review the microfluidic methods for generating uniform dispersed-phase droplets, focusing on those that utilize pressure-driven flows. We will report the experimental and numerical observations with particular emphasis on the results in the context of physical mechanisms for droplet breakup and simple theoretical models that have been proposed. Also, we will emphasize the influence of surfactant adsorption on droplet formation in microfluidic geometries. Then, we will discuss the various numerical methods which have been employed to model interfacial two-phase flows, and interfacial flows with surfactants. Finally, this chapter will conclude with a summary of remaining challenges, and how we are going to tackle them.

In Chapter 3, we will describe the phase-field lattice Boltzmann model for a binary fluid. We will address the improvements in reducing the spurious velocities and implementing the wetting boundary conditions. Also, a stress-free outflow boundary condition will be proposed to conserve the total mass of flow in the system and improve the numerical stability for flows with low Reynolds number. In Chapter 4, the model will be extensively validated by the benchmark cases including the Laplace's law, the static contact angles at solid surface, the merging and non-merging behavior of two stationary droplets without collision. Afterwards, this model will be employed to simulate the droplet deformation, breakup, glancing collision with coalescence and separation under simple shear flow. Finally, we will carry out the simulations of a droplet attached on a solid wall in simple shear. These simulations will demonstrate that our improved LB model is able to model contact-line motion.

In Chapter 5, 2D numerical simulations will be performed to understand the mechanisms of droplet formation in a microfluidic T-junction. We will systematically examine the influence of capillary number, flow rate ratio, viscosity ratio, and contact angle in the droplet generation process. In addition, we will investigate how droplet generation transits from the squeezing regime to the dripping regime.

Experimental observations have identified that the mechanisms of droplet formation are discrepant in a microfluidic T-junction and cross-junction. As a flow-focusing device, a cross-junction has also shown to generate highly uniform droplets/bubbles. In Chapter 6, our model will be used to further study the influence of capillary number, flow rate ratio, viscosity ratio, and viscosity of the continuous phase on droplet formation in a microfluidic cross-junction. A scaling law will be established to predict the size of droplets.

The capillary effect usually plays a dominant role in a microfluidic system, and the presence of surfactants at the interface will greatly modify interfacial tension. Therefore, surfactants are expected to significantly alter droplet dynamical behavior in microfluidic devices. In Chapter 7, a generalized phase-field model will be proposed for simulating droplet motion with soluble surfactants, which can have different solubility in immiscible bulk phases. The model will be shown to recover the well-known Langmuir and Frumkin adsorption isotherms in equilibrium. From the equilibrium equation of state, we can determine the interfacial tension lowering scale according to the interface surfactant concentration. The model will also be tested against the classical Ward-Tordai problem. The model will then be applied to examine the effect of soluble surfactants on droplet deformation, breakup and coalescence in a simple shear flow. It will be shown that the increase of surfactant concentration and attractive lateral interaction can enhance droplet deformation, promote droplet breakup, and inhibit droplet coalescence. We will also demonstrate that the Marangoni stresses can reduce the interface mobility and slow down the film drainage process, thus acting as an additional repulsive force to prevent the droplet coalescence.

The thesis will be summarized in Chapter 8, and discussions for future research in this field are provided.

Chapter 2

Literature review

The currently available studies on droplet dynamics in microfluidic devices are predominantly experimental. In Section 2.1, we first present a review of previous studies of microfluidic methods for generating uniform streams of droplets, focusing on those that utilize pressure-driven flows. In Section 2.2, the types of droplet breakup are characterised and some parameters clarifying the mechanisms of breakup in the confined microfluidic geometries are discussed. In Section 2.3, we summarise the experimental and numerical work with particular emphasis on the ones revealing the underlying physical mechanisms for droplet breakup and simple theoretical models that have been proposed. Section 2.4 discusses the computational problems related to the interfacial flows with and without surfactants. The remaining research challenges to understand the droplet breakup process are covered in Section 2.5. Section 2.6 briefly reviews the lattice Boltzmann method and several popular LB multiphase models. Section 2.7 describes the major contributions of our work.

2.1 Microfluidic methods for forming droplets

Microfluidic methods for generating droplets can be either passive or active. The widely-used passive methods use the flowfield to deform the interface of droplets and promote the natural growth of interface instability, which can avoid moving parts and explicit external actuation. Based on the characteristics of the flowfield near pinchoff, the passive microfluidic methods generally can be divided into three categories [3]: (1) co-flowing streams, (2) cross-flowing streams in a T-shaped junction, and (3) elongational flow in a flow-focusing geometry. Schematic illustrations of the three geometries are shown in Fig. 2.1. In general, the dispersed phase fluid is injected into a microchannel via a pressure-driven flow in which either volumetric flow rate or pressure is controlled. A second immiscible fluid is introduced into a separate microchannel via an independently controlled flow. The two fluids meet at a junction, where the dispersed phase fluid extends to form a “finger” or “jet”. The geometry of junction, the volumetric flow rates of the two fluids and their material properties determine the local flowfield, which deforms the droplet interface. Eventually, a droplet pinches off from the dispersed phase finger due to interfacial instability. In comparison with other technologies, using these microfluidic geometries to generate the droplets has a number of attractive features such as rapidity [37, 38], stability [39], uniformity [3], controllability of amount of reagent in each droplet [40] and low cost of chip fabrication [41].

Fig. 2.2 gives the typical images depicting the droplet breakup events in three main microfluidic geometries, in which three different droplet formation regimes are distinguished: squeezing, dripping, and jetting. Generally, droplet breakup from a capillary tip immersed in a continuous co-flowing liquid generally includes two distinct breakup regimes (see Fig. 2.2(a)): dripping, in which droplets pinch off near the capillary tip, and jetting, in which droplets pinch off from an extended thread downstream of the capillary tip. Three droplet formation regimes (i.e. squeezing, dripping, and jetting) can be observed and distinguished in microfluidic T-junctions (see Fig. 2.2(b)). In the squeezing and the dripping regime, droplet formation starts at the junction of the microchannel. Subsequently, the droplet grows and is deformed by the continuous phase liquid, until it is only attached to the bulk by a thin neck. Finally, the incipient droplet detaches at the downstream corner of the junction or slightly downstream from the junction. The difference between the squeezing and dripping is that in the squeezing regime the incipient droplet ultimately blocks the main channel completely, whereas in the dripping regime the continuous phase liquid can still flow past the incipient droplet. In the jetting regime, droplet formation starts downstream from the junction with a long dispersed-phase jet parallel to the flow direction of the continuous phase. The incipient droplet grows at the tip of this jet and detaches when the neck connecting the droplet to the bulk snaps-off, obviously also downstream from the junction. Droplet breakup via elongational flows in flow-focusing geometries can also be separated into squeezing, dripping and jetting regimes (see Fig. 2.2(c)). The squeezing regime is characterized by the droplet sizes that are larger than the orifice size, and the droplet completely blocks the orifice, leading to pinching

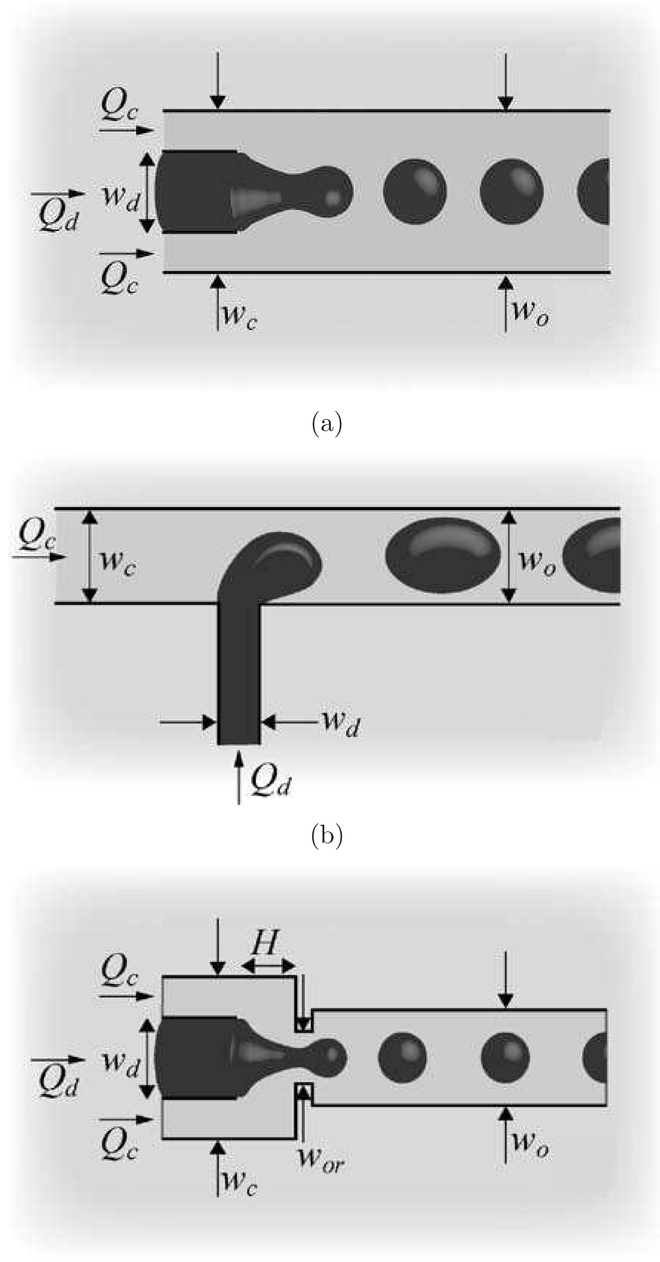

(a)

(b)

(c)

Figure 2.1: Schematic illustrations of three main microfluidic geometries used for generating droplets: (a) co-flowing streams; (b) cross-flowing streams in a T-shaped junction; (c) elongational flow in a flow-focusing geometry. In each geometry the widths of the inlet and outlet streams are indicated. It is assumed that the device is planar with a uniform depth h.

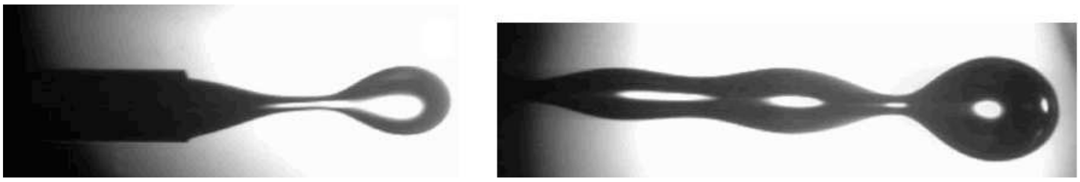

(a) Co-flowing streams (left: dripping; right: jetting)

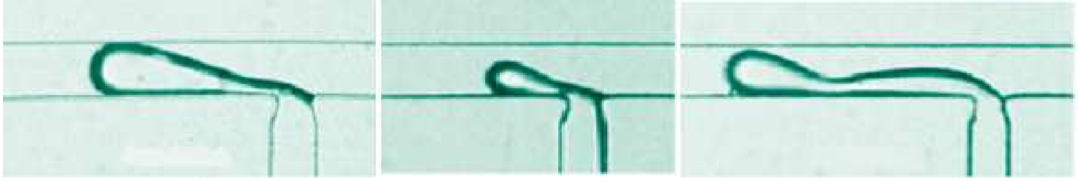

(b) T-junction (left: squeezing; middle: dripping; right: jetting)

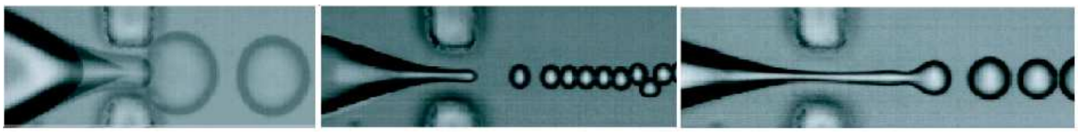

(c) Flow-focusing (left: squeezing; middle: dripping; right: jetting)

Figure 2.2: Images of droplet breakup in each of the three main microfluidic geometries used for droplet formation. The figures are taken from Cramer et al. [42] for (a), Zagnoni et al. [43] for (b), and Anna & Mayer [30] for (c), respectively.

of the interface inside the orifice. Once the droplet has formed, the finger of dispersed phase fluid retracts to a position at the upstream of the orifice. When the capillary number increases, droplet formation is in the dripping regime, where the portion of the interface does not retract after a droplet pinches off, but rather remains at a fixed location inside the orifice. In this case, droplets pinch off within one characteristic diameter of the flow focusing orifice. In the jetting regime, the dispersed phase finger extends at least three orifice diameters beyond the exit of the orifice and resembles a long jet. The jet interface exhibits undulations that grow until the discrete droplets pinch off. The resulting droplets are larger than those generated in the dripping regime, and less uniform.

Different types of droplets, such as plugs, discs and drops, can be generated in a microfluidic device, which strongly depend on the supplied flow conditions. Plugs are in contact with all four channel walls, discs are in contact with two parallel channel walls, and drops are not in contact with channel walls, and thus the drops are spherical. Generally, the formation of plugs and discs is termed as confined droplet breakup, while the formation of drops is termed as unconfined droplet breakup.

2.2 Characterization of droplet breakup in microchannel

2.2.1 Droplet breakup theory

There are three main forces acting on the emerging interface which affect the droplet breakup in a microfluidic geometry, i.e. viscous shear stresses, capillary pressure and squeezing pressure. The viscous shear stresses due to the continuous-phase fluid act to deform the interface. The magnitude of the viscous shear stresses can be estimated by the product $\eta_c G$, where η_c is the viscosity of the continuous-phase fluid and G is a characteristic rate of shear strain that is proportional to the volumetric flow rate Q_c of the continuous phase and a geometric factor. The magnitude of G depends on the specific geometry. The capillary pressure resists deformation by establishing a normal pressure jump $(p_d - p_c) \sim \sigma\kappa$ across the curved interface of the emerging droplet with the local interface curvature κ and the interfacial tension σ. Finally, as the emerging interface fills the junction, the available area through which the continuous-phase fluid can pass is restricted, leading to an increase in the pressure at the upstream of the junction. The excess pressure squeezes the neck of the emerging droplet, promoting breakup. The magnitude of the squeezing pressure increases dramatically as the distance between the emerging interface and the opposing wall of the microchannel decreases. In addition, a large surface area to volume ratio can promote the role of fluid-surface interaction, so that the wettability of the microchannel walls can strongly influence the droplet formation especially in the squeezing regime. In order to achieve consistent droplet breakup, it is important that the continuous phase fluid preferentially wets the walls.

2.2.2 Important dimensionless numbers

The droplet formation process could be fully described by several parameters characterising the flow and material properties of the fluids. These parameters are the average velocities of the continuous and dispersed phases, u_c and u_d respectively, the viscosities of the two fluids η_c and η_d, the interfacial tension σ, the density ρ, and the contact angle characterizing the wetting properties of a solution on a solid surface. Several key dimensionless numbers can be used to analyse the relative importance of each of key forces for the droplet breakup.

The capillary number Ca describes the relative magnitude of the viscous shear stress compared with the capillary pressure. A simple definition for Ca is given in terms of the average velocity u_c of the continuous-phase fluid,

$$Ca = \frac{\eta_c u_c}{\sigma}. \tag{2.1}$$

This definition is chosen to be consistent with classic experiments studying the deformation and breakup of isolated droplets in linear flows. In microfluidic droplet formation, capillary numbers typically range from 10^{-3} to 10.

The Reynolds number Re indicates the importance of inertial force in comparison with viscous shear stress, and is defined in terms of the characteristic length L of the microfluidic geometry,

$$Re = \frac{\rho u_c L}{\eta_c}. \tag{2.2}$$

Generally, the inlet channel width w_c of the continuous phase is chosen as the characteristic length. Small geometric length scales typically lead to $Re < 1$ for microfluidics.

The Weber number We is usually used to parametrize droplet breakup processes when inertial force and capillary pressure are more important than viscous shear stresses. The product of the capillary number and the Reynolds number yields the Weber number,

$$We = ReCa. \tag{2.3}$$

Typically, inertial force is the least important among the three key forces in microfluidics [29,44]; however, the inertia does play a role in bubble formation [14, 16].

During a droplet formation experiment, the dispersed and continuous phase fluids are injected at different volumetric flow rates, and the flow rate ratio Q characterizes the contrast between these two velocities:

$$Q = \frac{Q_d}{Q_c}. \tag{2.4}$$

The viscosity ratio λ is an important parameter in droplet breakup, where

$$\lambda = \frac{\eta_d}{\eta_c}. \tag{2.5}$$

Finally, the Bond number Bo characterizes the relative importance of buoyancy and interfacial tension, and is given by

$$Bo = \frac{\Delta \rho g L^2}{\sigma}, \tag{2.6}$$

where $\Delta\rho$ is the density difference between the dispersed phase and the continuous phase. For water droplets in oil which is considered in this thesis, the density difference is typically small, and so the magnitude of Bo can be as small as 10^{-3}. Hence, buoyancy is typically negligible in microdroplet formation.

2.3 State of the art of the droplet dynamics in microchannels

In recent years, great efforts have been devoted to exploring droplet and bubble formation in microfluidic devices. Thorsen et al. [17] was first to report the droplet formation in a T-junction microchannel. They found that the droplet size decreases with the increase of continuous phase flow rate and viscosity. They proposed a simple argument based on the original work of Taylor that the droplet will break up when the viscous shear stresses overcome the capillary force, i.e. $Ca \simeq 1$, yielding an expression for the droplet diameter d,

$$d \simeq \frac{2\sigma}{\eta_c G}. \tag{2.7}$$

This simple argument predicts the droplet sizes within a factor of two of the measured sizes. However, it is necessary to obtain the values of shear rate empirically. Even worse, the relationship between the shear rate G and the imposed pressures at both inlets is not clear.

Cubaud and Ho [45] investigated the liquid-gas flows in square microchannels with the bubbles generated in a cross-shaped mixing section. They observed that wettability plays an important role and can significantly affect the flow patterns in the system. Later, Cubaud et al. [13] found the bubble breakup in a cross-junction could be understood to be due to the competition between the pressure drops in the liquid and the gas phases. The bubble length in their experiment could be predicted by the ratio of the gas-liquid flow rates. Garstecki et al. [14] elaborated upon the mechanism for the bubble breakup process in the flow-focusing device with a small orifice, and they found that the bubble formation is due to the pressure gradient and the breakup can be controlled by the flow rate of the liquid phase. Garstecki et al. [20] later found that at low capillary numbers the breakup of plugs in microfluidic T-junctions is also caused by the squeezing pressure due to the high flow resistance to the continuous phase induced by the emerging bubble/droplet. In the squeezing regime, it is observed that the plug length depends predominantly on the flow rate ratio Q and not on the capillary number Ca. Garstecki et al. argued that detachment begins once the emerging droplet fills the channel and the droplet keeps growing due to continuous injection of the dispersed phase fluid, so the relationship between the droplet length l and Q is

$$\frac{l}{w_c} = 1 + \alpha Q, \tag{2.8}$$

where α is a fitting constant of order unity.

The squeezing mechanism at low capillary number was numerically validated by De Menech and co-workers [22] in a T-shaped microchannel. Also, they observed that the droplet formation regime is linked to the Ca, and an increase in Ca causes transition from the squeezing regime into the dripping regime and subsequently into the jetting regime. Examining the influence of the capillary number, flow rate ratio and viscosity ratio in a square channel, a distinct transition between the squeezing and dripping regimes was found at a critical capillary number $Ca_{cr} \approx 0.015$, above which the slope of the curve plotting the droplet volume as a function of capillary number becomes significantly steeper. In the dripping regime $Ca > Ca_{cr}$, the viscous shear stresses start to play an important role in the process of breakup. Larger viscosity ratios lead to smaller droplets, and droplet size decreases significantly as the capillary number increases. The authors examined the pressure fluctuations upstream of the emerging interface and found that even in the dripping regime the squeezing pressure cannot be neglected since the confinement of the emerging interface always plays a role in the process. However, Christopher et al. [23] recently observed that the droplet size depends on the capillary number and the flow rate ratio in both squeezing and dripping regimes. The viscosity ratio influences the droplet size only when the viscosities are similar. When the viscosity ratio λ is less than 1/50, the resulting droplet size is independent of the viscosity ratio and no transition to a purely squeezing regime appears. In this case, both the droplet size and the droplet production frequency obey power-law dependence on Ca. A scaling model was proposed by which the size of the droplets formed at a microfluidic T-junction can be estimated indirectly based on the capillary number. According to this model, the droplet breakup should occur when the sum of the viscous stresses and the squeezing pressure exceed the capillary force resisting deformation of the droplet. From this force balance, one can write the final dimensionless length $\bar{l} = l/w_c$ of the droplet as

$$\bar{l} = \bar{b} + \frac{\Lambda}{\bar{b}} Q, \tag{2.9}$$

where $\Lambda = w_d/w_c$ is ratio of channel widths, and $\bar{b}$ is the dimensionless length of the emerging droplet, which satisfies the following equation

$$(1 - \bar{b})^3 = \bar{b} Ca. \tag{2.10}$$

Eq. (2.9) is equivalent to Eq. (2.8) except that in the model of Garstecki et al., $\bar{b} = 1$ and the fitting constant α replaces the width ratio Λ.

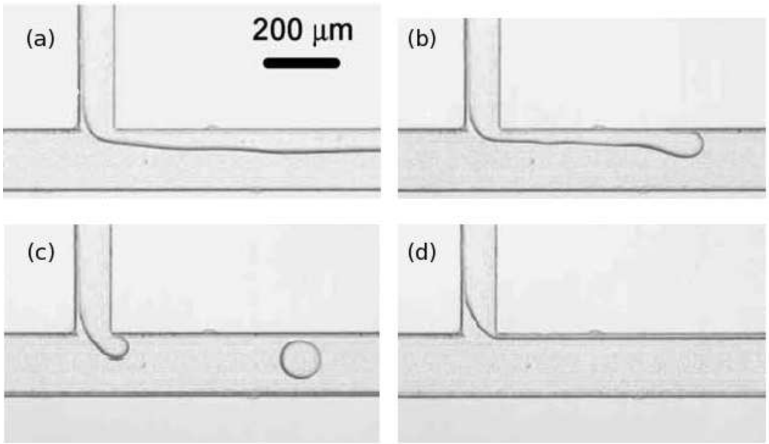

Figure 2.3: Patterns of droplet formation observed in a T-junction when the flow rate of the continuous phase (Q_c) is varied at a fixed flow rate of the dispersed phase ($Q_d = 0.1$ ml/h): (a) $Q_c = 0.5$ ml/h; (b) $Q_c = 1.0$ ml/h; (c) $Q_c = 2.0$ ml/h; (d) $Q_c = 22.0$ ml/h. The figures are taken from Nisisako et al. [46].

Nisisako et al. [46] reported that the variation of flow pattern caused by Q_c at a constant Q_d: at low Q_c (i.e. low Ca), parallel flow (PF) (see Fig. 2.3(a)) is observed in a T-junction. This changes to jetting (see Fig. 2.3(b)) at higher Q_c. Upon further increase in Q_c, the flow regime changes to dripping (see Fig. 2.3(c)) at the T-junction and eventually reverts to jetting (see Fig. 2.3(d)). For confined droplet breakup, Guillot and Colin [19] showed that for a given Q_c, if Q_d increases, the flow pattern changes from droplets at T-junction(DTJ) to droplets in channel(DC). With further increase in Q_d, the flow regime changes to parallel flow(PF). They developed a semi-empirical model, supported by experiments, to describe the transition from DTJ to PF. A phase diagram depicting the observed transitions is shown in Fig. 2.4. The predicted transition depends primarily on the the flow rate ratio and is derived based on a "blocking-pinching" mechanism ruled by flow rate conservation.

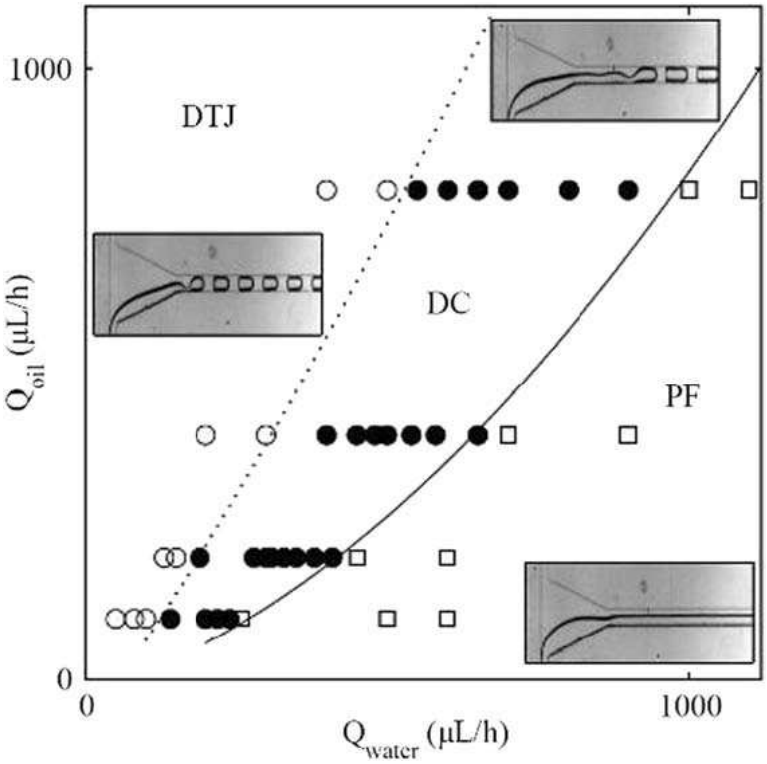

Figure 2.4: Droplet breakup modes for confined plug formation in a microfluidic T-junction. As the dispersed phase flow rate Q_d increases, direct breakup near the junction gives way to an extended thread that breaks downstream. For larger Q_d, the two streams co-flow parallel to each other. The figure is taken from Guillot and Colin [19].

Xu et al. [47] found the bubble formation in a T-junction microchannel is also affected by the viscosity of the continuous phase. They concluded that the capillary number governs the breakup dynamics. But the bubble size is independent of the interfacial tension. van der Graaf et al. [21,48] modeled the droplet formation in a T-junction by the numerical simulations and experimental observations. They observed in both confined and unconfined droplet breakup, the final droplet volume V is a result of two-stage growth. Initially, the droplet grows to a critical volume until the drag force exerted by the continuous phase balances the capillary force. Subsequently, the droplet continues to grow for a certain period until finally pinches-off due to the continuous injection of the dispersed phase fluid. According to van der Graaf et al. [21], both volume contributions are functions of Ca, and the following equation was proposed:

$$V = V_{c,ref} Ca^{m} + t_{n,ref} Q_d Ca^{n}, \tag{2.11}$$

where $V_{c,ref}$ and $t_{n,ref}$ are taken from simulation results at a capillary number of one. For T-junctions with $100 \times 100 \mu m$ channels, van der Graaf et al. found that $V_{c,ref} = 2.5 \times 10^{-5} \mu L$, $t_{n,ref} = 135 \mu s$, and $m = n = -0.75$.

Zhao et al. [49] proposed an empirical model to describe the size of droplets formed in all the regimes (squeezing, dripping and jetting) in a T-shaped microchannel. The model was based on their own experimental data, which suggests that the droplet size depends on the flow rates and the Weber numbers of both continuous phase and dispersed phase:

$$\frac{R}{D_{H,c}} = -0.1276 \ln \left[\frac{We_c \left(\frac{Q_c}{Q_c + Q_d} \right)}{\left(We_d \left(\frac{Q_d}{Q_c + Q_d} \right) \right)^{0.15}} \right] + 0.5595, \tag{2.12}$$

where R is the radius of an unrestricted spherical droplet which has the same volume as the actual droplet, $D_{H,c}$ is the hydraulic diameter of the continuous phase channel, We_c is the Weber number of the continuous phase, and We_d is the Weber number of the dispersed phase. Yu et al. [50] carried out experiments and lattice Boltzmann simulations to study the formation of gas bubbles in microfluidic cross-junctions with channel widths of 125 and $250 \mu m$ respectively. It was found that at high Ca ($Ca > 0.03$), the bubbles in bullet shapes were generally formed by shear instability, characterized by the stretching of the gas stream. At low Ca ($Ca < 0.01$), the bubbles in plug form were usually pinched off by the pressure difference in the two phases. Umbanhowar et al. [24] experimentally investigated the droplet formation at a capillary tip into a flowing surrounding liquid, i.e. co-flowing streams. They measured the droplet sizes and compared the experimental data with a scaling model, which is derived from a force balance accounting for the viscous shear stresses of the continuous phase liquid and the capillary pressure. The predicted droplet size is obtained by solving the nondimensional equation:

$$\bar{d}^3 - \left(1 + \frac{1}{3Ca}\right)\bar{d}^2 - \frac{Q}{\alpha}\bar{d} + \frac{Q}{\alpha} = 0, \tag{2.13}$$

where $\bar{d} = d/d_i$ is the droplet size scaled by the inner diameter of the capillary tube, the capillary number Ca is defined as $Ca = \eta_c u_c/\sigma = \eta_c Q_c/\sigma A_c$ with A_c denoting the cross-sectional area of the outer channel, and $\alpha = A_d/A_c$ is ratio of two cross-sectional areas. Eq. (2.13) clearly shows that the predicted droplet size is independent of the dispersed phase viscosity, consistent with the experimental observations of Cramer et al. [42]. The authors argued that the dripping will occur when the capillary pressure is more important than inertia, i.e. $We < 1$, or when $Q_d < \pi(d^3\sigma/2\rho_d)^{1/2}$. Furthermore, they pointed out that as long as Q_d is low enough, Eq. (2.13) can reduce to

$$\bar{d} \approx 1 + \frac{1}{3Ca}. \tag{2.14}$$

The predicted values agree well with the experimental results over the considered range of experimental conditions, validating the assumption that the viscous shear stresses and the capillary pressure are dominant in droplet breakup.

Hua et al. [25] used a front-tracking/finite volume method to investigate the droplet formation in co-flowing immiscible liquids. Two droplet formation regimes, namely dripping and jetting, are successfully produced through the numerical simulations under certain flow conditions. The correlation of the dimensionless droplet size $\bar{d}$ with the continuous phase flow parameters such as the Reynolds number, capillary number, Weber number and viscosity ratio can be obtained as $\bar{d} \propto Ca^{-1/2}Re^{-1/6}$ in the dripping regime and $\bar{d} \propto Ca^{1/3}We^{-1/2}\lambda^{1/2}$ in the jetting regime. Utada et al. [51] used a microcapillary device to study the transition from dripping to jetting in a two-phase co-flowing stream. The authors observed two distinct classes of transitions from dripping to jetting. One is driven by the viscous shear stresses from the continuous phase liquid, and the other is driven by the inertial forces from the dispersed phase liquid. The transition can be characterized by a state diagram that depends on both the capillary number of the continuous phase fluid and the Weber number of the dispersed phase fluid. Tan et al. [15] studied the formation mechanism of plug flow in an oil/water microfluidic cross-junction. They observed that the length of plugs decreases with the increase of continuous phase and total flow rates, as well as the viscosity of the continuous phase, while increases slightly with the increase of dispersed phase flow rate. Considering the equilibrium between the viscous shear stresses of the continuous phase fluid and the capillary force, and the influence of oil/water flow rate on the shape of the interface, a scaling equation was proposed to predict the length of plugs

$$\frac{l}{w_c} = kQ^{\alpha}Ca^{\beta}, \tag{2.15}$$

where k, α and β are fitting parameters. Tan et al. [15] found that, with the fitting parameters $k = 1.59$, $\alpha = 1/5$ and $\beta = -1/5$, Eq. (2.15) appears to provide a good fit across the whole range of experimental data. Recently, Tan and co-workers [52] investigated the formation of gas-plug-in-water in the microfluidic T-junctions, and found that the scaling equation Eq. (2.15) can still be used to predict the length of gas plugs.

Xu et al. [53] systematically analysed the scaling law of droplet formation in T-junction microchannels, and divided the two-phase flow patterns by the capillary number into three regimes: the squeezing regime ($Ca < 0.002$), dripping regime ($0.01 < Ca < 0.3$) and transient regime ($0.002 < Ca < 0.01$). In the squeezing regime, the final length of plugs is considered to be a contribution of two steps: growth length and squeeze length. Different from the model suggested by Garstecki et al. [20], the growth length of the plug l_{growth} is not strictly equal to w_c, but is written as $l_{growth} = \varepsilon w_c$ with ε being a parameter dependent on the geometry of the channel. Hence, the length of the plug can be given by

$$\frac{l}{w_c} = \varepsilon + \alpha Q, \tag{2.16}$$

where ε and α are the fitting parameters. The authors used Eq. (2.16) to fit the experimental data in Refs. [2, 20, 31, 54, 55] and argued that the values of ε and α are mainly determined by the channel geometry. In the dripping regime, a modified model was developed to predict the droplet diameter considering the influence of growing droplet size on the continuous phase flow rate, especially when the droplet size is comparable to the microchannel dimensions. In the transient regime, the model initially proposed by Tan et al. [15] for the plug formation in a cross-junction was extended to describe the plug length.

Dollet et al. [56] studied the role of the channel geometry in the bubble pinch-off in flow-focusing devices. They observed that the bubble breakup consists in a slow linear 2D collapse of the gas thread, ending in a fast 3D pinch-off.

They presented an analysis based on the perturbation of the gas-liquid interface, suggesting that the 2D collapse is always stable, while the 3D collapse is always unstable, causing bubble polydispersity. During 3D pinch-off, a scaling $w_m \sim \tau^{1/3}$ between the neck width w_m and the time τ before breakup indicates that the breakup is driven by the inertia of both gas and liquid, not by capillary instability. Fu et al. [16] investigated the bubble formation mechanism in a cross-junction microchannel using a high-speed digital camera and a micro-particle image velocimetry (μ-PIV) system. Various flow patterns, namely slug bubble, isolate bubble and satellite bubble, were obtained in the cross-junction by changing gas and liquid flow rates. Also, they found that the bubble (slug) breakup process is mainly controlled by the collapse stage, during which, the collapse rate of the thread neck and the collapse time were affected by the ratio of the gas/liquid flow rates and the viscosity of the liquid phase. Later, Fu et al. [57] scaled the formation of plug bubbles in two different cross-junctions with square channels of respectively 600×600 and $400 \times 400 \mu m$, and found that the length of plugs could be correlated to the ratio of the gas/liquid flow rates and the liquid Reynolds number, i.e.

$$\frac{l}{w_c} = kQ^{\alpha}Re^{\beta}. \tag{2.17}$$

Furthermore, the authors found that all the experimental data for the 3D pinch-off stage could be described by a mean power-law exponent of 0.31 ± 0.03, very close to 1/3, i.e. $w_m \propto \tau^{1/3}$, as observed by Dollet et al. [56]. Considering the neck width of gaseous thread w_m relying on the gas and liquid flow rates, liquid viscosity and the size of the cross-junction, an extended scaling law was proposed to describe the final pinch-off stage of the bubble formation:

$$w_m = 18.62Q^{-0.15}\tau^{1/3}. \tag{2.18}$$

Zhou et al. [58] used finite element method with adaptive meshing in a diffuse-interface framework to simulate the droplet formation in a microfluidic flow-focusing device. They argued that the mechanism for droplet breakup in the dripping regime is a mixture of capillary instability, including the classic Rayleigh capillary instability and an end-pinching mechanism, combined with viscous drag on the emerging droplet from the continuous phase fluid, which stretches and thins the neck region behind the droplet. The authors also argued that the dripping will give way to jetting when disturbances on the droplet interface are convected downstream before they can be amplified. This leads to a critical Weber number for the transition from dripping to jetting given by $We_{cr} \sim \rho R_{jet} V_{jet}^2 / \sigma \lambda_w^2$, where R_{jet} and V_{jet} are the radius and velocity of the jet respectively, and λ_w is the wavelength of the capillary wave. They analysed this expression and concluded that the critical Weber number for this transition scales as $We_{cr} \sim Q^{-1/2}$ if the dispersed phase flow rate Q_d is held fixed, or as $We_{cr} \sim Q^{3/2}$ if the continuous phase flow rate Q_c is held fixed. Utada et al. [51] argued that the transition from dripping to jetting in flow-focusing configurations will occur when the timescale for visco-capillary pinch-off is comparable to the timescale for growth of the jet, leading to a critical capillary number for the transition given by $Ca_{cr} = t_{pinch}/t_{growth} = \eta_c Q_d / \sigma R_{jet} \sim 1$. When $Ca < Ca_{cr}$, the interface instability will grow as soon as the emerging jet is long enough to sustain an instability, consistent with dripping, whereas for $Ca > Ca_{cr}$, viscous shear stresses on the interface are large enough to suppress the instability and allow for a longer thread.

Abated et al. [59] studied the impact of inlet channel geometry on droplet formation in droplet makers with T-junction style inlets and those with flow-focus style inlets. They found, at low and moderate capillary number, the droplet formation is dominated by the capillary force and mediated by the confinement of the microchannel, and the droplet size as a function of flow rate ratio follows a simple functional form based on the blocking-squeezing mechanism. For coflowing devices, Xiong et al. [60] thought that the bubble size is proportional to the ratio of the gas/liquid flow rates. The interfacial tension and the liquid viscosity just lead to different bubble shapes. Jensen et al. [61] presented a numerical investigation of the dynamics of the bubble formation in an axisymmetric flow-focusing device, and proposed a scaling law for the bubble size that is a function of the gas pressure, liquid flow rate, outlet channel size, interfacial tension and liquid viscosity. Compared to the experimental observations of Garstecki et al. [14], they found that the collapse rate of the gaseous thread is proportional to the ratio of the interfacial tension to the viscosity. They attributed this difference to the anisotropic confinement versus the axisymmetric confinement in their model.

Surfactants are usually used in the emulsion preparation process to adjust the interfacial tension and stabilize the emulsion [31]. When one uses the microfluidic devices for droplet formation, the surfactant is dissolved in one phase, usually in the continuous phase, and then injected into the microchannel using a syringe pump. In this way, the dynamic adsorption of surfactant on the interface occurs during the droplet formation, and the interfacial tension at the pinch-off moment will be strongly influenced by the adsorption process. In many experiments on the droplet formation, excessive surfactants are usually used to weaken the effect of adsorption and make the interfacial tension nearly constant during the droplet breakup process [15,55], since it is considered that the surfactant adsorption process is much faster than the pinch-off process at high surfactant concentration. However, the dynamic adsorption process is very important for the surfactants with big molecular weight and poor adsorption performance or those with low surfactant concentration. van der Graaf et al. [62] examined the effect of surfactant adsorption on the droplet formation during membrane emulsification. Their experiments showed that the dynamic interfacial tension influences the process of droplet formation; higher surfactant concentrations lead to smaller droplets and shorter droplet formation times. Wang et al. [63] experimentally studied the variation of dynamic interfacial tension caused by slow adsorption of surfactant, as well as its influence on the droplet formation process in a T-shaped microchannel. It was observed that the droplet size changed with the variation of surfactant concentration when the surfactant concentration was lower than a critical value, but hardly changed at higher concentrations, which was caused by the unsaturated adsorption and saturated adsorption of surfactant, respectively. The authors used the scaling model proposed by Tan et al. [15] to relate the interfacial tension (σ) with the droplet diameter d, i.e.

$$\frac{d}{d_c} = kQ^{\alpha} Ca^{\beta} = kQ^{\alpha} \left(\frac{\eta_c u_c}{\sigma} \right)^{\beta}, \tag{2.19}$$

where d_c is the characteristic diameter of the microchannel. They also found that the dynamic interfacial tension was mainly affected by the number density of the micelles, the formation time, and the convection of the two phases. A semi-empirical equation was established to characterize those effects. Steegmans et al. [64] carried out the droplet formation in microfluidic Y-junctions and used the droplet size to quantify the dynamic interfacial tension. In their experiments, the droplets were formed in less than milliseconds. They observed that the surfactant concentration has a significant effect on the droplet sizes for the surfactant concentration below the critical micelle concentration (CMC), and further showed that the surfactant transport is dominated by convection during the droplet formation.

2.4 Modelling and simulation of droplet dynamics

Modelling and simulation of droplet dynamics are essential to understand multiphase flows. Conventionally, multiphase flows are simulated by solving the Navier-Stokes equations and a transport equation for the interface. In the last 25 years, several techniques have been developed to describe complex evolution of a multiphase system, which can be classified into two major types: the interface-tracking and the interface-capturing. The former directly 'tracks' the location of the phase interface. The interface grid points moves with the interface in a Lagrange manner. Here, we introduce two major types of interface-tracking methods: moving-mesh method [65] and the front-tracking method of Tryggvason et al. [66]. For the moving-mesh method, the interfacial region is regarded as an infinitely thin or sharp dividing interface. The grid for the computational domain is selected in such a way that the interface between two phases is located along a grid line. The Navier-Stokes equations are solved in separate domains and the appropriate boundary conditions are applied at the interface. Through iteration, the velocity of the interface is determined, and then the interface is moved to a new location for the next time step. In this way, the computations continue and the interface is exactly tracked. The major disadvantage of this method is that a great number of grid points are required on the interfaces to accurately describe large deformations. So dynamical remeshing is required which increases the computational cost. Also, a strategy based upon fundamental physics which allows for liquid breakup does not currently exist for the moving-mesh method. This would require rupturing the interface, and then remeshing two interfaces where only one existed. In the front-tracking method of Tryggvason et al. [66], two sets of grids are used. A fixed grid is used to determine the fluid flow while the interface is tracked using a lower dimensional grid, i.e. a 1D grid for 2D flow and a 2D grid for 3D flow. Only one set of Navier-Stokes equations are solved in the fixed grids. The fluid properties are selected separately for each phase. The interfacial tension force needs to be transformed from the surface force into a volumetric force at the control points. And then, it will distribute to the fixed grids. Since no remeshing is required in the fluid domain and the interface-tracking is a lower dimensional problem, the computational cost will be significantly reduced in this method. As the interface is tracked, it is still difficult to simulate the droplet coalescence and breakup. The currently available methods for coalescence or breakup are not firmly based on physics, but instead on artificial treatments or ad hoc criteria such as the distance between interfaces.

Contrary to the interface-tracking approach, the interface-capturing method uses a continuous function to distinguish different phases (to be called "indicator function" thereafter). This type of approach is able to deal with topological changes in a natural way. The indicator function is generally chosen as the volume fraction of one of the two phases/components, as in the volume-of-fluid (VOF) method [27], the signed distance to the interface, as in the level-set (LS) method [67], or the density/mass fraction of one phase or component (also called order parameter later), as in the phase-field models (PFM) [68]. In this class of approach, there is only one set of unified partial differential equations(PDEs) that govern the fluid flows using Eulerian grids and the interfaces are implicitly captured by the indicator function (known as "interface capturing"). In the following, we will briefly review the VOF, LS and PFM methods with attentions on the application of these methods for fluid-surface interactions (i.e. contact-line dynamics), and the interfacial flows with surfactants.

2.4.1 Volume-of-fluid method

The VOF method uses the volume fraction of one of the fluid phases or components (denoted as C) to characterize the interfaces. In the bulk phase (i.e. a pure fluid), C is equal to zero or unity; in multi-fluid cells, it has a value of $0 < C < 1$. The most commonly used VOF method consists of two major steps, i.e. the interface reconstruction step, which finds an explicit description of the interface in each multi-fluid cell based on the volume fractions at this time step, and the advection step, which calculates the distribution of C at the next time step by solving an advection equation using the reconstructed interface and the underlying velocity field. The interfacial tension force model, which takes account of interfacial tension effects at the interface, is also very important in modelling microdroplets. Two widely-used interface reconstruction methods are Simple Line Interface Calculation (SLIC) [69] and the Piecewise Linear Interface Calculation (PLIC) [70]. In the SLIC method, the volume of fluid in each cell is treated as if its local interface is either a vertical or horizontal line. In the PLIC method, the local phase interface is determined by fitting a straight line in the cell that satisfies the volume of fluid criteria, and the orientation of the straight line is found by the distribution of one of the fluids in the neighboring cells. This method is shown to be very robust and efficient, but only of first-order accuracy. The volume fraction function is purely advected by the velocity field, i.e., it obeys the equation: $\partial_t C + \vec{u} \cdot \nabla C = 0$. As this equation suffers discontinuity across the interface, it is important to use sophisticated numerical schemes to solve it. Generally, the effect of interfacial tension force is incorporated into the momentum equation following the continuum surface force (CSF) model of Brackbill et al. [71]. The normal vector and the curvature of the interface are calculated from derivatives of this smoothed volume fraction function. The interfacial tension force is applied using these two computed quantities, and its magnitude is proportional to the interfacial tension σ. The balance of forces across the interface is purely reflected in the pressure field, and not in C. So in addition to an interface indicator, the other role of the volume fraction function is for the enforcement of the interfacial tension effect, which is not obviously related to any physical energy.

Renardy et al. [72] gave detailed discussions on how to apply the VOF method for the multiphase/multicomponent flows involving moving contact line (CL). They compared two different implementations to incorporate wetting in VOF method: one extrapolated the volume fraction beyond the computational domain, providing that its gradient is perpendicular to the interface and the normal to the interface at the wall is determined by the known equilibrium contact angle; the other one treated the problem as a three-phase situation, mimicking the classical argument of Young. In addition, a suitable slip model with some slip length was used so that the singularity problem with the CL dynamics was relieved. They argued that the latter approach introduced an artificial localized flow, so the extrapolation method was preferred.

Renardy et al. [73] developed a VOF method for 3D droplet deformation in the presence of insoluble surfactants. To my best knowledge, this was the first application of a continuum-based method to study surfactant dynamics. Their implementation of surfactant was somewhat *ad hoc* and only surfactants with linear equations of state were considered. This method was applied to study droplet deformation in shear flows in 3D. It was found that when the droplet becomes cusp-like, the simulation becomes sensitive to the discretization parameters and the surfactant can diffuse off the droplet interface. Although the simulations appear to show tip streaming, the surfactant concentration becomes very high at the drop tips and the interfacial tension actually becomes negative. A mesh refinement study indicated that the results depend on the temporal and spatial step sizes. James and Lowengrub [74] developed a surfactant-conserving VOF method to study the effects of insoluble surfactants on interfacial flows. Instead of solving the surfactant concentration equation based on Stone's derivation [75] directly, the authors related the surfactant concentration to the ratio of the surfactant mass and interface area so that they are tracked independently. They argued that an arbitrary equation of state relating the surfactant concentration to the interfacial tension can be used. The method has been applied to study the axis-symmetric droplet deformation in extensional flow, and its subsequent retraction and breakup upon cessation of the external flow.

2.4.2 Level set method

The LS method is firstly introduced by Osher and Seithian [76]. The basic idea is to use a smooth function (level set function) defined in the whole solution domain to represent the interface. It is defined as a signed distance to the interface and is purely a geometrical variable. The advantage is that the level set function varies smoothly across the interface, which eliminates the discontinuity problem that occurs in the VOF method. The interface tension force in the level set method is also modelled using the continuum surface force (CSF) method [71], except that the interface delta function is replaced by a Heaviside function. Similar to the volume fraction function in the VOF method, the level set function used in the LS method is purely transported by the flow velocity. In contrast to the volume fraction, it is just an indicator and has no physical meaning. Thus, the level set function need not satisfy the conservation law. It only needs to consider the differentiation of the convection term. However, the level set method requires a re-initialization procedure to restore the signed distance property when large topological changes occur around the interface [77]. This may violate the mass conservation for each phase or component. The way to incorporate wetting and CL dynamics in LS is similar to the first approach described above in the VOF method, i.e. the interface normal at the solid boundary is determined from the contact angle. By incorporating a model of the dynamic contact angle depending on the CL velocity, Spelt [78] extended the LS method for multiphase flow simulations involving moving CLs with the hysteresis effect being taken into account. Later, Spelt [79] applied it to study shear flows over 2D droplets.

Xu et al. [80] developed a level-set method for interfacial Stokes flows with surfactant. Their method couples surfactant transport, solved in an Eulerian domain with Stokes flowfield, solved by the immersed interface method with jump conditions across the interface. However, the method does not conserve the mass automatically and the numerical scaling is used to enforce the conservation of surfactant on the interface numerically. It was applied to study the effects of surfactant on single droplet, droplet-droplet interactions and interactions among multiple droplets in the Stokes flow under a steady applied shear.

2.4.3 Phase-field method

PFM originates from the theory for near-critical fluids, in which the fluid system is fundamentally viewed as a whole and the indicator function (i.e. order parameter) is associated with the free energy of the system based on the Cahn-Hilliard theory [81]. The order parameter is a conserved variable that varies continuously over thin interfacial layers and is mostly uniform in the bulk phases. PFM resolves the interface structure with the interfacial region having its own physics inside; but as the interface width becomes smaller and smaller (compared with the macroscopic length), it can be mathematically proven that PFM approaches the original sharp interface equations [68,82]. The equation of fluid motion which is modified to account for the presence of a thin layer can be applied over the entire domain. For example, the Navier-Stokes equations can be modified to include a pressure tensor accounting for the interfacial tension. The pressure tensor can be derived by the use of reversible thermodynamic arguments. The interfacial tension can be given in terms of the excess free energy which is distributed through a 3D layer rather than being defined on a 2D surface. The order parameter is evolved according to the Cahn-Hilliard equation, where the interface sharpness is automatically maintained by the anti-diffuse term without losing the continuity. The interface structure is preserved as the interface evolves, so that the method does not require additional efforts to keep the interface intact as in other methods [83, 84]. In addition, the smooth representation of the interface as a region with the finite thickness prevents the numerical difficulties caused by the interface singularities. Wetting and CL dynamics can be easily incorporated in PFM through a surface energy term [85]. Some important basic issues in numerical simulations using PFM have been studied by Jacqmin [86], and the

CL dynamics in PFM has been excellently analyzed for a simple 2D problem by Jacqmin [87]. Recently, it has been applied to study capillarity driven droplet spreading by Khatavkar et al. [88] and droplet impact on a surface by Khatavkar et al. [89].

Noticeably, van der Sman and van der Graaf [90] developed a PFM for surfactant adsorption onto the interface of two immiscible fluids. The model was based on a free energy functional, partly adapted from the sharp interface model of Diamant and Andelman [33]. It has been shown that the model can exhibit the well-known adsorption isotherm–Langmuir isotherm. The model was applied to simulate the classical Ward-Tordai problem [91] and the deformation of a surfactant-laden droplet in a shear flow, which indicated that the PFM model is very promising to model and simulate the droplet dynamics in an oil-water-surfactant system.

2.5 Remaining research challenges

In this chapter, previous studies on droplet formation in microfluidic devices have been reviewed. From this literature review, it can be seen that in spite of much work already done by many researchers, the available information is still fragmented due to the differences in channel dimensions, flow rates and materials (e.g. viscosities, interfacial tension, and wetting properties) used. This leads to inconclusive and even contradictory findings as reported in the literature. The same is true for the current models (i.e. scaling laws), which can only describe a limited range of the droplet formation spectrum. For example, Steegmans et al. [92] used statistical analysis to evaluate the models for describing the droplet size in microfluidic T-junctions and found that none of the models is general enough to describe the original data and data from other literature sources. Obviously, the mechanisms which control the droplet formation remain unclear, and the influence of various flow conditions still needs further investigation.

Meanwhile, the available numerical methods show that several approaches for modelling the droplet dynamics in microfluidic devices have their own limitations. The interface-tracking methods are not suitable for simulating the droplet breakup and coalescence, which needs additional efforts to determine when to rupture or merge interfaces and how to reconfigure the new interfaces. The VOF and LS methods are able to predict the droplet topological changes, but the treatment of the interface is based upon macroscopic physics where the interface is described by an indicator function without significant physical meanings and the interfacial tension is calculated by the curvature of interface. Fundamentally, the interfacial tension is a macroscopic parameter that results from microscopic interaction between molecules. Different from VOF and LS, PFM is another type of interface-capturing methods where the order parameter in PFM may be related to some physics such as the free energy and the equation of state. The main drawback of PFM is that the discretization of fourth order derivative is required in the calculation when one uses the traditional CFD solver. As to the modeling of wetting and CL dynamics, VOF and LS often rely on explicitly finding the interface position and impose the contact angle or some sophisticated predetermined model on the interface near the wall; while PFM addresses this issue in a seemingly more natural way by adding the surface energy contribution. Strictly speaking, the interface between different phases and the CL dynamics on the solid surface is based on the mesoscopic scale [34]. Thus, mesoscopic level studies are expected to be more appropriate for investigating the effect of wettability of the solid surface on water droplet dynamic behavior in the microchannels.

Although FT, VOF and LS have been successfully applied to simulate interfacial flows with surfactants, these methods are built upon the conservation laws at macroscopic level for interfacial dynamics, originating from the model proposed by Stone [75]. Meanwhile, they commonly suffer from several drawbacks: (i) dynamic interfacial tension relies on an asserted equilibrium equation of state, which is also assumed to be valid beyond the equilibrium state; (ii) for interfacial flows with soluble surfactants, mass transfer between the interface and the bulk fluids requires an external boundary condition, which cannot uniquely arise from the model itself; (iii) model extension for more complicated systems, such as ionic surfactant solutions, is not easy [33]; (iv) numerical stability becomes a problem for the flows with large topological changes, such as droplet breakup and coalescence. The PFM presented by van der Sman and van der Graaf [90] has demonstrated promising potential to simulate droplet dynamics in the presence of surfactants. However, the model is restricted to the Langmuir adsorption with equal solubility of the surfactants in both bulk phases. Although the model showed that the interfacial tension lowering $\Delta\sigma$ is proportional to $k_B T \ln(1-\psi_0)$ due to surfactant adsorption onto the interface, the dependence of the proportionality factor on the parameters used in the model is still unclear. Finally, the model capability is required to be further examined and demonstrated by simulating droplet dynamics with large topology changes.

2.6 Lattice Boltzmann method

In light of these uncertainties and limitations in the continuum methods discussed above, we will use the lattice Boltzmann method (LBM) to simulate the droplet dynamics in microfluidic devices. In recent years, LBM has been developed into an alternative and powerful tool for complex fluid systems [93]. Unlike the traditional CFD methods, which solve the conservation equations of macroscopic properties (i.e. mass, momentum and energy) numerically, LBM models the fluid consisting of fictive particles, and such particles perform consecutive propagation and collision processes over a discrete lattice grid. LBM originated from the lattice gas automata (LGA) method [94], which can be considered as a simplified fictitious molecular dynamics model in which space, time, and particle velocities are all discrete. The main motivation for the transition from LGA to LBM was the desire to remove the statistical noise by replacing the Boolean particle number in a lattice direction with its ensemble average, i.e. the so-called particle distribution function (PDF) [95]. Furthermore, the discrete collision rule is replaced by a continuous function known as the collision operator. In the LBM development, an important simplification to the collision operator is using the Bhatnagar-Gross-Krook (BGK) collision model. This lattice BGK (LBGK) model [96] makes simulations more efficient and allows flexibility of the transport coefficients. On the other hand, it has been shown that the LBM scheme can also be considered as a special discretized form of the continuous Boltzmann model equation. Based on Chapman-Enskog multi-scale analysis [97], one can recover the macroscopic continuity and Navier-Stokes equations from the LBM algorithm. In addition, the pressure field is also directly available from the density distributions and thus there is no extra Poisson equation to be solved. Due to its intrinsic kinetic nature and local dynamics, LBM has several advantages over other conventional CFD methods: simplification of nonlinear modeling, computational efficiency and accuracy, the capability of dealing with complex boundaries, and a mathematical framework allowing the molecular level modeling. These advantages make the LBM especially useful for simulation of multiphase flows in microfluidic devices [95]. Several LBM models for the simulation of multiphase flows have been developed. These include the chromodynamic model, the pseudo-potential model, the free-energy model, and the mean-field theory model. The chromodynamic model [98] is based on red and blue PDFs representing two different fluids. The effect of interfacial tension is obtained through a perturbation step modeled by a collision operator added to the original collision operator, and phase separation is maintained through a segregation step by forcing particles to regions of the same color. However, the segregation step requires time-consuming calculations of local maxima, and the perturbation step with the redistribution of colored PDFs causes an anisotropic interfacial tension that induces high spurious velocities near the interface [97]. The pseudo-potential model [99] introduces the nearest-neighboring interaction between fluid particles to describe the intermolecular potential, and the phase separation occurs with a properly chosen potential function. However, as pointed out by He and Doolen [100], the interfacial tension in this model is actually a numerical artifact and its value is controlled by a force parameter, which cannot be prescribed a priori. In addition, this model does not satisfy local momentum conservation so that the spurious velocities are high near the interface. The free-energy model proposed by Orlandini et al. [101] and Swift et al. [35] uses a free-energy functional to include interfacial tension effects in a thermodynamically consistent manner. Actually, it is the PFM realized in the framework of LBM, in other words, the free-energy model can recover to the PFM through a Chapman-Enskog expansion under the low Mach number limitation. Hence, the free-energy model is endowed with the advantages of the PFM as stated above. However, the free-energy model suffers from the lack of Galilean invariance [95], though the local momentum conservation is satisfied. In addition, minimising unphysical spurious velocities at interface remains a challenge for the free energy LB models. The mean-field theory model proposed by He et al. [100] is valid in the nearly incompressible limit and applies to nonideal gases. In this model, the simulation parameters are the pressure and an index function, which is used to capture the interface and plays the same role as the indicator function in the interface-capturing methods. Interfacial dynamics is modeled by introducing molecular interaction forces, which are approximated by the mean-field theory. Phase separation occurs naturally owing to the instability of the supernodal curve of the phase diagram. The serious limitation of the mean-field theory model is its numerical instability [102], associated with the 'stiffness' of the collision operator, when the 'complex fluid' effects are introduced by the forcing term. Furthermore, Rannou [103] used various LB multiphase models to investigate a fully developed two-phase Poiseuille flow in a 2D channel, and found that, the mean-field theory model gives accurate results for the high-viscosity phase but poor results for the low-viscosity phase. Obviously, each LB multiphase model has its own advantages and disadvantages. The best choice of model depends on the problem itself and/or one's taste. In a microfluidic device, the flows are typically characterized by small capillary numbers, so it is necessary for a suitable model to have good numerical stability for the microdroplet interfacial dynamics and small spurious velocities at the interface so that the small flow velocities are not contaminated.

2.7 Contribution of this work

In this thesis, we have developed an improved LB model, using the phase-field theory to describe the interfacial interactions, with the purpose of reducing the spurious velocities and to easily incorporate the complicated wetting boundary conditions, making the model a good candidate for the simulation of droplet dynamics in microfluidic devices. The model has been extensively validated then employed to investigate the influence of the physical and flow parameters including flow rate ratio, capillary number, viscosity ratio and contact angle on the droplet formation in surfactant-free microfluidic T-junction and cross-junction respectively. Some previous experimental and numerical findings have been verified, and some new physics has been identified. We have gained a deeper understanding of the droplet breakup mechanisms in confined geometries. Although the PFMs have shown promise for computation of binary mixture with surfactants, significant effort is still required to improve the model for realistic oil/water/surfactant systems. Therefore, we will also present a generalized PFM in the LB framework to simulate the adsorption of surfactants and its effect on droplet dynamics.

Chapter 3

Phase-field lattice Boltzmann model for a binary fluid

In this chapter, we will describe the phase-field LB model that we have used to obtain the numerical results presented in the subsequent three chapters. A unifying feature of all the phase-field models is the existence of a free-energy functional, which not only determines the equilibrium properties, but also strongly influences the dynamics of a multiphase system. In these models, the evolution and breakup of the interface occur naturally which can be described by the thermodynamic theory such as the Cahn-Hilliard equation [104]. One notable feature of the Cahn-Hilliard theory is that the stress singularity arising in the classical model of moving contact lines as pointed out by Huh & Scriven [105] is removed due to the mass transfer across the interface. Whereas other methods require some special treatment on the contact line region to make it move. Due to its rich physical basis, the phase-field model has been widely used to simulate droplet deformation, coalescence, breakup and contact line dynamics [86,88,89,106–110]. The hydrodynamic equations of motion in the phase-field model can be solved in many different ways. In this thesis, we will use a particular mesoscopic modelling technique called the lattice Boltzmann method. It has proved to be a powerful tool to study many complex fluids problems.

This chapter consists of three parts. Firstly, we introduce a free energy functional for a binary fluid and explain how it handles the essential ingredients needed to describe phase separation and interfacial tension. The generalisation of the Navier-Stokes equations appropriate for the two-phase system are summarised, with the emphasis on the improvements in reducing the spurious velocities and incorporating the wetting boundary condition. Afterwards, we describe the lattice Boltzmann algorithm that is used to solve the hydrodynamic equations. Finally, we give the thermodynamic and hydrodynamic boundary conditions needed to model wetting and inflow & outflow open boundaries, in which a stress-free outflow boundary condition is proposed to conserve the total mass of flow system and improve the numerical stability for flows with low Reynolds number.

3.1 The phase-field theory

We consider a binary incompressible fluid consisting of oil and water molecules with the phase ordering into an oil-rich and a water-rich phase below a critical temperature. The Ginzburg-Landau free energy functional [35] is used to describe the thermodynamics of the fluid,

$$\mathscr{F}(\rho, \phi, \nabla\phi) = \int \left[\Psi(\phi) + \frac{1}{2}\kappa(\nabla\phi)^2 + \rho c_s^2 \ln\rho\right] dV, \tag{3.1}$$

where the total fluid density ρ is $\rho_w + \rho_o$ with ρ_w and ρ_o being the densities of water and oil components respectively; $\phi = (\rho_w - \rho_o)/\rho$ is the order parameter, which represents the relative concentration of local composition [111] (note that the fluid is understood to be a mixture of oil and water components, so the density ρ_w (or ρ_o) is a local value and defined by the average mass of oil (or water) per unit control volume); $\Psi(\phi)$ is the bulk free energy density for a homogeneous system, which can be chosen as a double-well form $\Psi(\phi) = \frac{1}{4}A(\phi^2 - 1)^2$, with A being a positive constant controlling the interaction energy between two components/phases; the term $\frac{1}{2}\kappa|\nabla\phi|^2$ denotes the free energy excess in the interfacial region, which is defined as the interface energy between different phases with κ relating to the interfacial tension; c_s is the lattice speed of sound. Note that the final term in the free energy functional does not affect the phase behavior, which is introduced to enforce incompressibility in the LBM.

The chemical potential μ is defined as the variational derivative of the free energy functional with respect to the order parameter, i.e.,

$$\mu = \delta\mathscr{F}/\delta\phi = \Psi'(\phi) - \kappa\nabla^2\phi = A\phi(\phi^2 - 1) - \kappa\nabla^2\phi. \tag{3.2}$$

The equilibrium interface profile can be obtained from Eq. (3.2) at $\mu = 0$, which leads to two stable uniform solutions $\phi = \pm 1$ representing the coexisting bulk phases.

For simplicity, let us consider a planar oil-water interface in a quiescent infinite system, the order parameter profile across the interface can be given by

$$\phi(z) = \tanh(z/\xi), \tag{3.3}$$

where z is the spatial location normal to the interface ($z = 0$), and ξ is a measure for the thickness of interface, which is defined as

$$\xi = \sqrt{2\kappa/A}. \tag{3.4}$$

Since ξ must typically be chosen of the order of a few lattice spacings in simulation, models of this type are often called diffuse interface models. We define the interface thickness to be the distance from -0.9 to 0.9 so that the equilibrium interface thickness is $2\xi \tanh^{-1}(0.9) = 2.944\xi$. This width contains 98.5% of the interface tension stress [86].

The interfacial tension σ can be interpreted as the excess free energy per unit interface area, and for a planar interface in equilibrium, it can be evaluated by [112]

$$\sigma = \int_{-\infty}^{+\infty} \kappa \left(\frac{\mathrm{d}\phi}{\mathrm{d}z}\right)^2 dz. \tag{3.5}$$

From Eqs.(3.3)–(3.5), we can get

$$\sigma = \frac{4\kappa}{3\xi}. \tag{3.6}$$

Equations (3.4) and (3.6) suggest that we can determine the parameters κ and A by specifying the interfacial tension and the interface thickness.

The hydrodynamics of a binary fluid can be described by the continuity equation (3.7), the Navier-Stokes equation (3.8) and the Cahn-Hilliard equation (3.9) [35, 111]:

$$\nabla \cdot \vec{u} = 0, \tag{3.7}$$

$$\rho(\partial_t \vec{u} + \vec{u} \cdot \nabla \vec{u}) = -\nabla \cdot \boldsymbol{P} + \nabla \cdot [\eta(\nabla \vec{u} + \nabla \vec{u}^{\mathrm{T}})], \tag{3.8}$$

$$\partial_t \phi + \vec{u} \cdot \nabla \phi = \nabla \cdot (M \nabla \mu), \tag{3.9}$$

where $\vec{u}$, $\boldsymbol{P}$, η, and M are the fluid velocity, pressure tensor, dynamic viscosity, and Cahn-Hilliard mobility respectively. The equilibrium properties of the fluid are involved in the equations of motion through the chemical potential while the pressure can be derived via the Gibbs-Duhem relation [111]:

$$\nabla \cdot \boldsymbol{P} = \nabla(\rho c_s^2) + \phi \nabla \mu. \tag{3.10}$$

Obviously, thermodynamic equilibrium corresponds to $\nabla \cdot \boldsymbol{P} = 0$. A suitable choice of pressure tensor, which fulfils Eq. (3.10) and reduces to the usual bulk pressure if no gradients of the order parameter are present, is

$$\boldsymbol{P} = \left[p_b - \frac{\kappa}{2}(\nabla\phi)^2 - \kappa\phi\nabla^2\phi\right]\boldsymbol{I} + \kappa(\nabla\phi)(\nabla\phi)^{\mathrm{T}}, \tag{3.11}$$

with the bulk pressure term p_b given by

$$p_b = \rho c_s^2 + A\left(-\frac{1}{2}\phi^2 + \frac{3}{4}\phi^4\right), \tag{3.12}$$

where the speed of sound c_s follows that $c_s^2 = \frac{\mathrm{d}p_b}{\mathrm{d}\rho}$.

In the free energy model developed by Swift et al. [35], the interfacial tension force is introduced by imposing additional constraints on the equilibrium PDF. In addition to the mass and momentum conservation constraints, the equilibrium PDF is constructed in such a way, that its second moment reproduces the desired pressure tensor, i.e. Eq. (3.11). However, the free energy model violates Galilean invariance, as the resulting momentum equation contains an error term, which makes the Navier-Stokes equation unable to be correctly recovered. In addition, the unphysical spurious velocities, caused by a slight imbalance between the stresses in the interfacial region, are pronounced near the interfaces and surfaces. Pooley et al. [36] identified that the strong spurious velocities in the steady state lead to an incorrect equilibrium contact angle for a binary fluid with different viscosities. In the diffuse interface methods, the key to reducing the spurious velocities lies in the formulation of treating the interfacial tension force. Jacqmin [86] suggested that the chemical potential form of the interfacial tension force, i.e. Eq. (3.10), guaranteed to generate motionless equilibrium states without spurious velocities. Jamet et al. [113] later showed that the chemical potential form can ensure the correct energy transfer between the kinetic energy and the interfacial tension energy. Although both methods proposed by Swift et al. [35] and Jacqmin [86] are completely equivalent mathematically, they produce different discretization errors for the calculation of the interfacial tension force.

Hence, the chemical potential form will be employed in our study, but a minor modification is required to incorporate the wetting property of walls.

When the fluid-solid interaction is considered, the chemical potential at the solid wall cannot be easily specified in order to calculate $\nabla\mu$ at the fluid lattice sites next to the wall. Luckily, Eq. (3.10) can be expressed as

$$\nabla\cdot\boldsymbol{P}=\nabla(\rho c_s^2)+\phi\nabla\mu=\nabla p-\mu\nabla\phi, \tag{3.13}$$

where $p=\rho c_s^2+\phi\mu$ is the modified pressure. Using Eq. (3.13), the Eqs. (3.7)-(3.9) can be rewritten as

$$\nabla\cdot\vec{u}=0, \tag{3.14}$$

$$\rho(\partial_t\vec{u}+\vec{u}\cdot\nabla\vec{u})=-\nabla p+\nabla\cdot[\eta(\nabla\vec{u}+\nabla\vec{u}^{\mathrm{T}})]+\mu\nabla\phi, \tag{3.15}$$

$$\partial_t\phi+\vec{u}\cdot\nabla\phi=\nabla\cdot(M\nabla\mu). \tag{3.16}$$

In the LB model, p and the interfacial force term $\vec{F}_S=\mu\nabla\phi$ can be simply incorporated by modifying the equilibrium distribution function and by treating as an external body force [114], respectively.

3.2 The lattice Boltzmann algorithm

Instead of directly solving Eqs. (3.14)-(3.16), we present a LB algorithm to indirectly determine the macroscopic properties. The basic idea behind LB algorithm is to associate the PDFs, discretized in time and space according to a set of lattice velocity vectors $\vec{e}_i$. For instance, for a two-dimensional 9-velocity model (D2Q9) [96], the lattice velocities are chosen to be $\vec{e}_0=(0,0)$, $\vec{e}_{1,3}=(\pm c,0)$, $\vec{e}_{2,4}=(0,\pm c)$, $\vec{e}_{5,7}=(\pm c,\pm c)$ and $\vec{e}_{6,8}=(\mp c,\pm c)$. The lattice speed c is defined by $c=\delta_x/\delta_t$, where δ_x is the lattice distance, and δ_t is the simulation time step. The speed of sound c_s can be related to c by $c_s=c/\sqrt{3}$.

To describe a binary fluid, we need to define two particle distribution functions $f_i(\vec{x},t)$ and $g_i(\vec{x},t)$ on each lattice point. The macroscopic variables are related to the PDFs by

$$\rho(\vec{x},t)=\sum_i f_i(\vec{x},t),\quad \rho\vec{v}(\vec{x},t)=\sum_i f_i(\vec{x},t)\vec{e}_i,\quad \phi(\vec{x},t)=\sum_i g_i(\vec{x},t), \tag{3.17}$$

where $\vec{v}$ is defined by $\rho\vec{v}=\rho\vec{u}-\vec{F}_S\delta_t/2$. The distinction between $\vec{u}$ and $\vec{v}$ occurs at the interface so as to introduce the interfacial tension and produce the pressure gradient.

The time evolution equations for the PDFs, using the standard BGK (Bhatnagar-Gross-Krook) approximation, can be broken down into two steps

$$\text{Collision step :}\quad f_i'(\vec{x},t) = f_i(\vec{x},t) - \frac{1}{\tau_f}[f_i(\vec{x},t) - f_i^{eq}(\vec{x},t)] + F_i(\vec{x},t), \tag{3.18}$$

$$g_i'(\vec{x},t) = g_i(\vec{x},t) - \frac{1}{\tau_g}[g_i(\vec{x},t) - g_i^{eq}(\vec{x},t)], \tag{3.19}$$

$$\text{Propagation step :}\quad f_i(\vec{x}+\vec{e}_i\delta_t, t+\delta_t) = f_i'(\vec{x},t), \tag{3.20}$$

$$g_i(\vec{x}+\vec{e}_i\delta_t, t+\delta_t) = g_i'(\vec{x},t), \tag{3.21}$$

where f_i^{eq} and g_i^{eq} are the equilibrium distribution functions of f_i and g_i, defined as a power series of the velocity, τ_f and τ_g are two independent relaxation parameters, and F_i represents the interfacial force distributions in the lattice space.

The governing physics of LB schemes is determined through the hydrodynamic moments of the equilibrium distribution functions and the forcing terms (i.e. the interfacial force components). The moments of f_i^{eq}, g_i^{eq} and F_i are:

$$\sum_i f_i^{eq} = \rho, \quad \sum_i f_i^{eq} e_{i\alpha} = \rho u_\alpha, \quad \sum_i f_i^{eq} e_{i\alpha} e_{i\beta} = \rho u_\alpha u_\beta + p\delta_{\alpha\beta},$$
$$\sum_i f_i^{eq} e_{i\alpha} e_{i\beta} e_{i\gamma} = \rho c_s^2(\delta_{\alpha\beta}u_\gamma + \delta_{\alpha\gamma}u_\beta + \delta_{\beta\gamma}u_\alpha), \tag{3.22}$$

$$\sum_i g_i^{eq} = \phi, \quad \sum_i g_i^{eq} e_{i\alpha} = \phi u_\alpha, \quad \sum_i g_i^{eq} e_{i\alpha} e_{i\beta} = \phi u_\alpha u_\beta + \Gamma\mu\delta_{\alpha\beta}, \tag{3.23}$$

$$\sum_i F_i = 0, \quad \sum_i F_i e_{i\alpha} = \delta_t(1 - \frac{1}{2\tau_f})F_{S\alpha},$$
$$\sum_i F_i e_{i\alpha} e_{i\beta} = \delta_t(1 - \frac{1}{2\tau_f})(u_\alpha F_{S\beta} + u_\beta F_{S\alpha}), \tag{3.24}$$

where $e_{i\alpha}$ is the projection of $\vec{e}_i$ on the α-axis ($\alpha = x$ or y), and $\delta_{\alpha\beta}$ are Kronecker delta.

A suitable choice for f_i^{eq}, g_i^{eq} and F_i that satisfies the constraints (3.22)-(3.24) is a power series expansion in terms of the velocity

$$f_i^{eq} = w_i\left[A_i + \rho\left(\frac{\vec{e}_i\cdot\vec{u}}{c_s^2} + \frac{\vec{u}\vec{u}:(\vec{e}_i\vec{e}_i - c_s^2\boldsymbol{I})}{2c_s^4}\right)\right], \tag{3.25}$$

$$g_i^{eq} = w_i \left[B_i + \phi \left(\frac{\vec{e}_i \cdot \vec{u}}{c_s^2} + \frac{\vec{u}\vec{u} : (\vec{e}_i\vec{e}_i - c_s^2 \boldsymbol{I})}{2c_s^4} \right) \right], \tag{3.26}$$

$$F_i = (1 - \frac{1}{2\tau_f}) w_i \left[\frac{\vec{e}_i - \vec{u}}{c_s^2} + \frac{\vec{e}_i \cdot \vec{u}}{c_s^4} \vec{e}_i \right] \cdot \vec{F}_S \delta_t, \tag{3.27}$$

where the coefficients A_i and B_i are given by

$$A_i = \begin{cases} p/c_s^2 & (i > 0) \\ \left[\rho - (1 - w_0) p/c_s^2\right]/w_0 & (i = 0), \end{cases} \tag{3.28}$$

$$B_i = \begin{cases} \Gamma\mu/c_s^2 & (i > 0) \\ \left[\phi - (1 - w_0)\Gamma\mu/c_s^2\right]/w_0 & (i = 0), \end{cases} \tag{3.29}$$

and w_i is the weight factor with $w_0 = 4/9$, $w_{1-4} = 1/9$ and $w_{5-8} = 1/36$.

It can be shown, using the Chapman-Enskog multiscale analysis (detailed derivations are given in Appendix A), that Eqs. (3.18)-(3.21) can reproduce Eqs. (3.14)-(3.16) in the continuum limit with the equilibrium distribution functions and forcing term given by Eqs. (3.25)-(3.27). Therefore, our phase-field LB model is Galilean invariant. The relaxation parameters τ_f and τ_g in the LB algorithm are related to the physical variables in the hydrodynamic equations η and M by

$$\eta = \rho c_s^2 \delta_t \left(\tau_f - \frac{1}{2} \right), \qquad M = \delta_t \Gamma \left(\tau_g - \frac{1}{2} \right), \tag{3.30}$$

where Γ is a tunable parameter that appears in the equilibrium distribution function g_i^{eq}. Since η and M are positive quantities, the values of the relaxation parameters τ_f and τ_g have to be larger than 1/2.

In this thesis, the densities of two components/phases are assumed to be equal because the density difference in the commonly-used water droplet in oil is small. We set $\tau_g = 1/(3 - \sqrt{3})$ to minimize numerical errors of the convection-diffusion scheme [115]. To account for unequal viscosities of the two phases, we define the viscosity η as a linear function of the order parameter:

$$\eta(\phi) = \frac{1 - \phi}{2} \eta_o + \frac{1 + \phi}{2} \eta_w, \tag{3.31}$$

where η_o and η_w are the viscosities of the oil and water phases. In this way, η automatically changes across the interface with a profile similar to the tanh function.

3.3 Selection of lattice units

The LBM uses variables that are in lattice units. It is crucial to select the proper units of the lattice variables. Two constraints determine the selection of units. First, the LB simulation should be equivalent, in a well defined sense, to the physical system. Second, the parameters should be fine-tuned in order to have stable computation and reach the required accuracy, i.e. the grid should be sufficiently resolved, the discrete time step sufficiently small. In a typical binary LB simulation, there are several important parameters controlling the physics of flows: the length scale of the system L, the magnitude of flow velocity U, the density of fluid ρ, the viscosity η and the interfacial tension σ. To match these lattice parameters to physical values we can choose only three quantities: a length scale L_0, a time scale T_0, and a mass scale M_0. These scales can be defined by both the physical and lattice parameters:

$$L_0 = \frac{\delta_x^{phy}}{\delta_x}, \quad T_0 = \frac{\delta_t^{phy}}{\delta_t}, \quad \frac{M_0}{L_0^3} = \frac{\rho^{phy}}{\rho}, \tag{3.32}$$

where the superscript '*phy*' denotes the parameter in physical unit. Generally, the lattice grid spacing δ_x, the simulation time step δ_t and the lattice density ρ are all taken to be unity. So we have

$$L_0 = \delta_x^{phy}, \quad T_0 = \delta_t^{phy}, \quad M_0 = \rho^{phy}(\delta_x^{phy})^3. \tag{3.33}$$

Once the three scales are determined, a simulation parameter with dimensions $[L]^{n1}[T]^{n2}[M]^{n3}$ is multiplied by $[L_0]^{n1}[T_0]^{n2}[M_0]^{n3}$ to give the physical value and vice versa. In practice, a useful approach is to determine L_0, T_0, and M_0 by satisfying the following constraints.

The major constraint of the LBM is that it is valid for incompressible flows, i.e. low Mach numbers and for flows with low Knudsen numbers, i.e. mean free path is small relative to the characteristic length. In order to avoid errors due to compressibility, the Mach number of the simulation should be chosen to be smaller than 0.15. Mach number is determined by:

$$Ma = \frac{U}{c_s} = \frac{U^{phy}}{\frac{1}{\sqrt{3}}\frac{L_0}{T_0}} < 0.15, \tag{3.34}$$

The relaxation time τ_f, which is associated with the fluid viscosity, has two constraints. The first is that it should not be much greater than 1 because as τ_f increases so does the Knudsen number. Also τ_f should not be close to or less than 0.5 because the instability may occur due to insufficient temporal resolution. Generally, it is a good choice to select $0.55 < \tau_f < 1.5$. From Eq. (3.30), one can get

$$0.55 < \tau_f = 3\frac{\eta}{\rho} + 0.5 = 3\frac{\eta^{phy}}{\rho^{phy}}\frac{T_0}{L_0^2} + 0.5 < 1.5. \tag{3.35}$$

Finally, in order to produce small spurious velocities and avoid the numerical instability, we recommend selecting

$$\sigma = \sigma^{phy}\frac{T_0^2}{M_0} \leq 0.03\rho\xi c_s^2, \tag{3.36}$$

According to the physical parameters, we can select suitable L_0, T_0 and M_0 by satisfying the above constraints, i.e. Eqs. (3.34)-(3.36). In fact, the selection of lattice units is a special nondimensionalization, in which the lengths and the velocities are non-dimensionalised by the grid size and $\sqrt{3}$ times of the speed of sound, respectively.

3.4 Boundary conditions

Boundary treatment is one of the key issues in the LB modelling interfacial flows. In a typical LB simulation of droplet formation in a microchannel there are several important boundary conditions: the open inflow and outflow boundary conditions, the no-slip boundary condition at the solid walls, and the wetting boundary condition for considering the fluid-surface interaction.

No-slip boundary condition is applied at solid walls using half-way bounce-back [95], which can prevent the boundary “mass leakage”, especially for a flow with small velocity. To conserve the total mass of the system and to ensure the numerical stability of solving flows with small Reynolds number, a stress-free boundary condition is proposed to treat the outflow boundary with the mass modification at each node introduced by considering the fully developed velocity profile.

Assuming that the fluid node $\vec{x}$ is a boundary node, its links are divided into two groups: boundary links (BL) and fluid links (FL) [116]. Without losing generality, the outflow boundary is set at the right-hand end of the system, $x = x_{max}$; the inflow boundary is set at the left-hand end, $x = x_{min}$; and the inlet velocity of fluid is directed to the right. After the collision step, the PDFs at the inlet and outlet boundaries are first modified as

$$\tilde{f}_i(\vec{x}, t+\delta_t) = \begin{cases} f'_{i^*}(\vec{x}, t) & \text{if } (i^*) \text{ is BL} \\ f'_i(\vec{x}+\vec{e}_{i^*}, t) & \text{otherwise,} \end{cases} \tag{3.37}$$

where $\vec{e}_{i^*} = -\vec{e}_i$.

The outflow boundary is stress-free, which means that

$$\frac{\partial u_x}{\partial x} = 0 \quad \text{at } x = x_{max}. \tag{3.38}$$

In the LBM, the stress-free outflow boundary, Eq. (3.38), can be implemented by

$$f_i(\vec{x}, t+\delta_t) = \begin{cases} \tilde{f}_i(\vec{x}_-, t+\delta_t) & \text{if } (i^*) \text{ is BL} \\ \tilde{f}_i(\vec{x}, t+\delta_t) + \delta f(\vec{x}, t+\delta_t) & \text{if } i = 0 \\ \tilde{f}_i(\vec{x}, t+\delta_t) & \text{otherwise,} \end{cases} \tag{3.39}$$

where $\vec{x}_- = (x_{max} - \delta_x, y)$, and δf will be defined below.

At the inflow boundary, a given constant velocity, $\vec{u}_{in}$, normal to the boundary, is imposed by

$$f_i(\vec{x}, t+\delta_t) = \begin{cases} \tilde{f}_i(\vec{x}, t+\delta_t) + 2w_i \rho u_{in}/c_s^2 & \text{if } (i^*) \text{ is BL} \\ \tilde{f}_i(\vec{x}, t+\delta_t) & \text{otherwise.} \end{cases} \tag{3.40}$$

Hence, the total net flux at all lattice sites at the inflow boundary follows

$$m_{tot} = \sum_{x=x_{min}} \sum_{(i^*)\in \text{BL}} 2\rho w_i u_{in}/c_s^2 = \sum_{x=x_{min}} \rho u_{in}. \tag{3.41}$$

Assuming that the fully developed velocity profile at the outflow boundary is $\vec{u} = (u_x(y), 0)$, the outgoing mass at site $\vec{x} = (x_{max}, y)$ can be calculated by

$$m(\vec{x}) = m_{tot} \frac{u_x(y)}{\sum u_x(y)}. \tag{3.42}$$

In order to conserve the total mass in the system, δf in Eq. (3.39) should be

$$\delta f(\vec{x}, t+\delta_t) = \sum_{(i^*)\in \text{BL}} [\tilde{f}_i(\vec{x}, t+\delta_t) - f_i(\vec{x}_-, t+\delta_t)] - m(\vec{x}). \tag{3.43}$$

The wetting properties are important for fluid/surface interactions. Iwahara et al. [117] proposed an elegant way to implement the wetting boundary condition in a vapor-liquid system. Recently, van der Graaf et al. [21] used the same wetting boundary treatment for a liquid-liquid system. They assume that the wall is a mixture of two fluids, thus having a certain value of the order parameter ϕ_w, so the derivatives of the order parameter at the surface boundary can be calculated using (9 points) regular finite difference stencils [118]. Consequently, the chemical potential and the interfacial force term in Eq. (3.27) become dependent on the properties of the neighboring solid lattice sites, resulting in a special case of the Cahn boundary condition [104].

The wetting properties are usually characterized by the contact angle of a solution on a surface. The Young's equation gives the relation between a contact angle and interfacial tensions. For a water droplet attached on a solid wall, surrounded by the oil phase, the equilibrium contact angle θ_w is given by

$$\cos(\theta_w) = \frac{\sigma_{w,oil} - \sigma_{w,water}}{\sigma}, \tag{3.44}$$

where $\sigma_{w,oil}$ or $\sigma_{w,water}$ is the interfacial tension between the fluid phase (oil or water) and the solid wall.

Since the solid wall is assumed to be a mixture of two fluids, the fluid-wall interfacial tensions can be calculated in a similar way to the fluid-fluid interfacial tension

$$\sigma_{w,water} = \int_{z_w}^{+\infty} \kappa \left(\frac{\mathrm{d}\phi}{\mathrm{d}z}\right)^2 dz, \tag{3.45}$$

$$\sigma_{w,oil} = \int_{-\infty}^{z_w} \kappa \left(\frac{\mathrm{d}\phi}{\mathrm{d}z}\right)^2 dz, \tag{3.46}$$

with $\tanh(z_w/\xi) = \phi_w$. Substituting Eq. (3.4) into Eqs. (3.45) and (3.46), we have

$$\sigma_{w,water} = \frac{\kappa}{3\xi}\left(2 - 3\phi_w + \phi_w^3\right), \tag{3.47}$$

$$\sigma_{w,oil} = \frac{\kappa}{3\xi}\left(2 + 3\phi_w - \phi_w^3\right). \tag{3.48}$$

Substituting the values of the interfacial tensions into Young's law, Eq. (3.44) becomes

$$\cos\theta_w = \frac{1}{2}\phi_w\left(3 - \phi_w^2\right). \tag{3.49}$$

From Eq. (3.49), the desired equilibrium contact angle can be obtained by assigning the order parameter ϕ_w to the solid lattice sites next to the wall. It should be noted that in principle Eq. (3.49) is only valid for the homogeneous surfaces and the equilibrium contact angle. However, Iwahara et al. [117] identified in their simulations that the present wetting boundary condition can mimic heterogeneous surfaces with arbitrary wettabilities, it can also capture the contact line pinning and the contact angle hysteresis etc. In contrast to the model proposed by Briant et al. [119], this approach can be more easily implemented, in particular for complex structured boundary and heterogeneous surface.

Chapter 4

Validation and analysis of model

This chapter has two objectives. First, we will validate the usefulness and accuracy of our model by comparing our simulation results with the analytical solutions. Second, we will further examine the phase-field lattice Boltzmann model for simulating the droplet dynamical behavior, such as the droplet deformation, break-up, coalescence, collision and contact line motions, which will indicate the capability of our toolkit for interfacial flows of complex fluids. Comprehensive exploration of new physics in complicated microfluidic devices will be carried out in the subsequent chapters.

4.1 Validation of the present model

To validate the proposed phase-field LB model, two examples of a water droplet placed in an unbounded oil-phase domain and on a solid wall are simulated. For the first benchmark case, a two-dimensional circular droplet is initially located at the centre of the lattice domain with 120×120 lattices in the xy-plane. The periodic boundary conditions are imposed at all boundaries. According to the Laplace's law, when the system reaches the equilibrium state, the pressure difference across the droplet interface Δp is related to the interfacial tension σ as

$$\Delta p = \frac{\sigma}{R}, \tag{4.1}$$

where R is the radius of the droplet. Fig. 4.1 shows the pressure difference Δp against $1/R$ using the following parameters: $\tau_f = 1.0$, $\sigma = 0.01$, $\xi = 1.5\delta_x$, and $\Gamma = 4.0$. It can be found that the model predictions ("□") are in excellent agreement with the Laplace's law (the solid line). Eq. (3.3) can also be used to

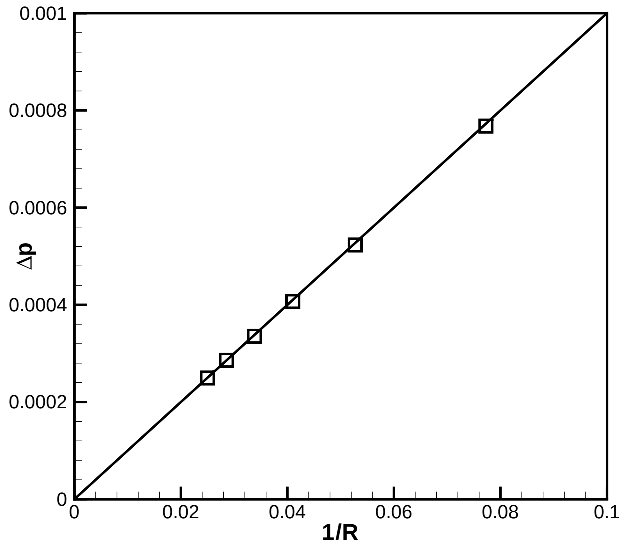

Figure 4.1: Comparison of the LBM results ("□") with the Laplace's law (the solid line) for pressure jump across a stationary droplet interface.

verify the accuracy of the numerical results, which can be written as

$$\phi(x,y) = \tanh \frac{R - \sqrt{(x-x_0)^2 + (y-y_0)^2}}{\xi}, \tag{4.2}$$

where x_0 and y_0 are the coordinates of the centre of the droplet. Fig. 4.2 displays the order parameter as a function of the distance from the droplet centre, which is in good agreement with the theoretical equilibrium profile given by Eq. (4.2). This shows that our method can correctly model and capture the phase interface. However, a numerical artifact observed in many numerical methods is the presence of spurious velocities at the phase interface. This is also true in our case. Fig. 4.3 shows the velocity vector plots in the final stage of droplet evolution for the improved color-function model presented by Lishchuk et al. [120], the free energy model of Swift et al. [35], and the present model, where the values of $\vec{u}$ are magnified by 1.5×10^5 times in (a), 5×10^4 in (b) and 1×10^7 times in (c) respectively. Although the improved color-function model has shown to significantly reduce the spurious velocities in comparison with the Gunstensen's model [98] and the Shan-Chen model [99], it can be observed that the magnitude of the maximal spurious velocity of the present model (1.6×10^{-6}) is much smaller than that of the improved color-function model (5.2×10^{-5}). Noticeably, although the

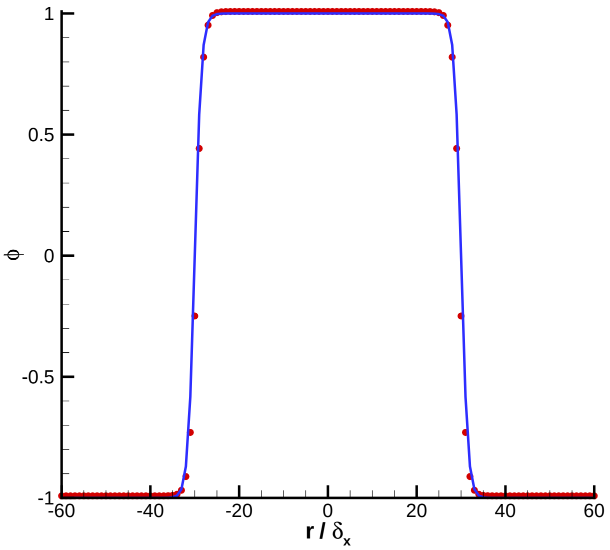

Figure 4.2: The profile of order parameter along the cross section of a droplet with $R = 30\delta_x$. The discrete symbols represent the simulation results of the present LB model and the solid line is the theoretical profile given by Eq. (4.2).

present model is essentially the same as the free energy model of Swift et al., building upon the Cahn-Hilliard free energy theory [81], the present model can effectively reduce the spurious velocities at the interface (note that the maximal spurious velocity is 3.75×10^{-4} in the model of Swift et al.) due to the smaller discretization errror introduced in the treatment of interfacial tension force [86].

As the first example, we use the aforementioned method to obtain the corresponding physical values of our LB parameters used above. We choose the length scale $L_0 = 6 \times 10^{-6}$ m and the time scale $T_0 = 6 \times 10^{-7}$ s. Also, we choose the density of fluid $\rho^{phy} = 10^3$ kg/m^3. Hence it can have the mass scale $M_0 = \rho^{phy} L_0^3 = 2.16 \times 10^{-13}$ kg. For a droplet with radius $R = 30$ lattices, the physical values of the simulation parameters can be given by: $R^{phy} = RL_0 = 1.8 \times 10^{-4}$ m, $\sigma^{phy} = \sigma \frac{M_0}{T_0^2} = 0.01 \frac{2.16\times10^{-13}}{(6\times10^{-7})^2} = 6 \times 10^{-3}$ N/m, $\eta = \frac{2\tau_f - 1}{6} \frac{M_0}{L_0 T_0} = \frac{1}{6} \frac{2.16\times10^{-13}}{(6\times10^{-6})(6\times10^{-7})} =$ 0.01 Pa s, and $\Delta p^{phy} = \Delta p \frac{M_0}{L_0 T_0^2} = 10^5 \Delta p = 33.53$ N/m^2.

To assess the fluid-solid interaction model given by Eq. (3.49) implemented in the proposed phase-field model, we perform the static contact angle simulation in a 200×80 domain. The initial condition is a semicircular stationary droplet sitting along the center line on the bottom wall. The top wall is assumed to be neutral wetting, i.e. $\phi_w = 0$. The periodic boundary condition is used in the

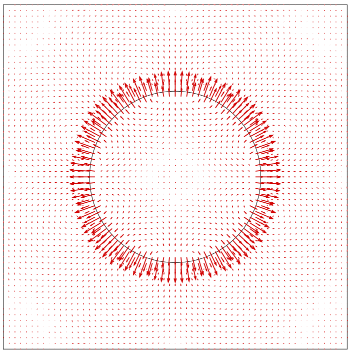

(a) Lishchuk's model

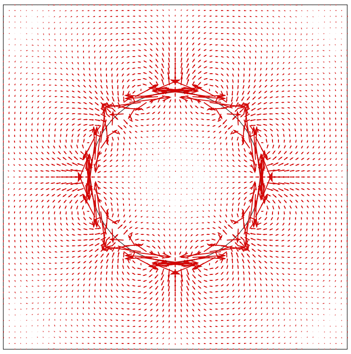

(b) Swift's model

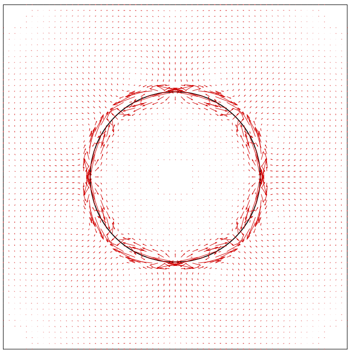

(c) Present model

Figure 4.3: Comparison of the spurious velocities of a droplet in stationary fluid with $\sigma = 0.01$ and $R = 30\delta_x$ for (a) the model of Lishchuk et al. [120], (b) the model of Swift et al. [35], and (c) the present model. Values of $\vec{u}$ are magnified by 1.5×10^5 times in (a), 5×10^4 times in (b), and 1.5×10^7 times in (c).

x-direction while the halfway bounce-back boundary condition is imposed at top and bottom in the y-direction. Other parameters are chosen as: $\sigma = 0.0025$, $\xi = 1.5\delta_x$, $\tau_f = 0.8$, and $\Gamma = 4.0$. We run the simulation until the shape of droplet does not change, i.e. reaching an equilibrium state. The contact angle is evaluated by fitting the arc of a circle to the cross section of the droplet and determining the contact angle of this arc with the solid wall using the least-square method. Fig. 4.4 gives the comparison of two different wetting boundary treatments for a droplet on a solid wall with static contact angles $\theta = 45^\circ, 90^\circ$ and 135°, where (a) uses the method described above, and (b) uses the method proposed by Briant et al. [119], which is based on the free energy model of Swift et al. [35]. It can be easily seen that both methods agree qualitatively. Fig. 4.5 shows the contact angle as a function of the order parameter value of the solid surface. The result shows good agreement with the theoretical line described by Eq. (3.49). A recent study of Pooley et al. [36] showed that, when the two phases have different viscosities for a binary fluid, the free energy model of Swift et al. (using the wetting boundary condition of Briant et al. [119]) can produce incorrect results for the equilibrium contact angle due to strong spurious velocities in the steady state. They demonstrated that one has to resort to a multiple-relaxation-time (MRT) algorithm (which has more complexity and higher computing cost in contrast to the single-relaxation-time (SRT) algorithm in the free energy model of Swift et al. [35]) in order to correctly capture the contact angle. To examine whether the present model can produce the correct equilibrium contact angle for both phases with different viscosities, we run simulations with $\tau_o = 0.59$ and $\tau_w = 1.4$ (this choice gives the viscosity ratio $\lambda = \frac{\tau_w - 0.5}{\tau_o - 0.5} = 10$), and keep the other parameters as used above. We find that all the simulation results are the same as those for the cases with $\tau_f = \tau_w = \tau_o = 0.8$. This may be because the spurious velocities are effectively suppressed in the present model. Therefore, the present phase-field LB model is capable of simulating two-phase flow with the presence of solid walls.

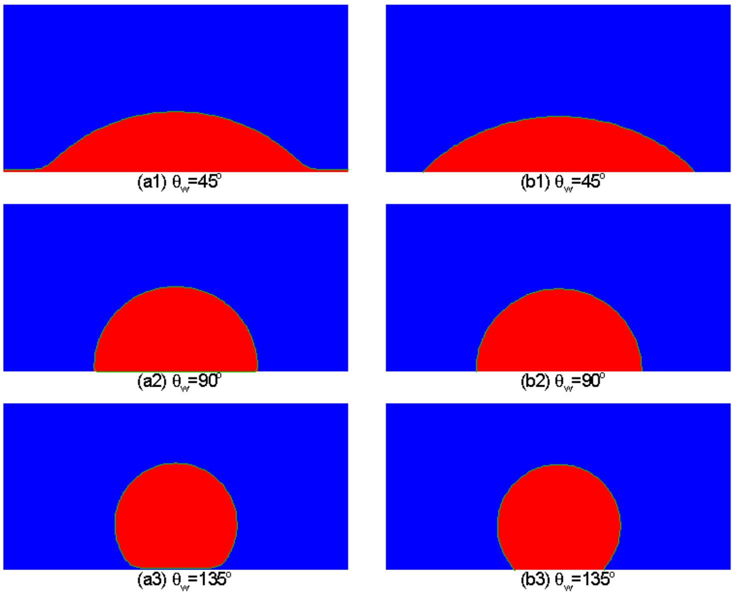

Figure 4.4: Comparsion of the simulations of static contact angles using (a) the present method and (b) Briant's method [119].

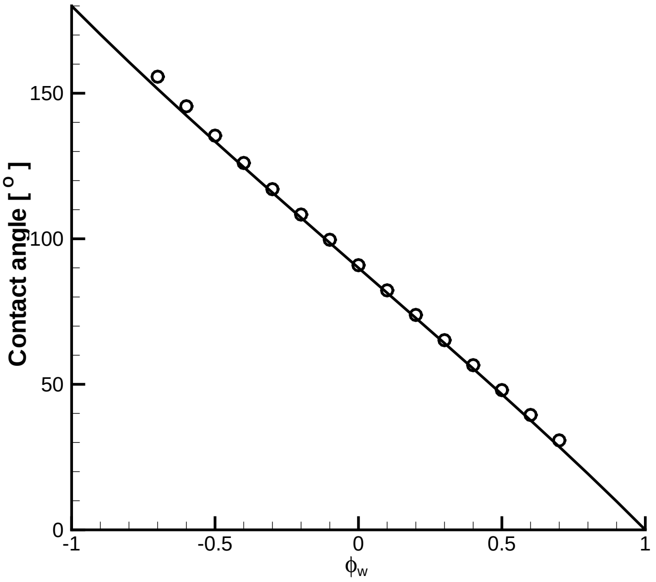

Figure 4.5: Contact angles as a function of the order parameter of the solid surface with the simulation data points ("○") and the solid line from analytical theory.

4.2 Droplet dynamics

4.2.1 Droplet deformation and breakup under simple shear flow

Taylor deformation is often used to assess whether a multiphase model is able to simulate dynamic problems. A droplet is placed between two parallel plates which are moving in opposite directions to obtain the shear flow in the Stokes regime (small Reynolds number), and droplet deformation is studied as a function of the shear rate (expressed as the Capillary number) at a constant Peclet number. The definitions of the Reynolds number, Capillary number and Peclet number [21,121] are given as

$$Re = \frac{\gamma R^2 \rho}{\eta}, \qquad Ca = \frac{\gamma R \eta}{\sigma}, \qquad Pe_\phi = \frac{\gamma R \xi}{MA} \tag{4.3}$$

where $\gamma = 2u_w/H$ is the shear rate with u_w being the velocity of moving wall, and H being the channel height, and R is the initial radius of the droplet. For this case, we assume that the densities and viscosities are the same for both fluids. The simulations are run at $Re = 0.1$ and $Pe_\phi = 2.0$ for a droplet with the radius of 32 lattice cells in a system of 256×128 lattice cells. At the steady state, the droplet is assumed to be an elliptic shape, which is usually characterized by the deformation parameter Df, defined as

$$Df = \frac{a-b}{a+b}, \tag{4.4}$$

where a and b are the major and minor axis of the ellipse. In 2D, it is expected that Df follows the Taylor relation for small Ca [122], which reads:

$$Df = f(\lambda) Ca, \tag{4.5}$$

where λ is the viscosity ratio between droplet and matrix fluid. We also carry out the simulations using the LB free energy model developed by Swift et al. [35] with the same parameter settings, as well as using the VOF method with the same physical parameters and grid size. In Fig. 4.6 we have plotted Df versus Ca for both LBM and VOF simulations. We observe that the simulation results of the present model are almost the same as those of Swift's model, and the results of the present model are slightly closer to the VOF results. In addition, the linear dependence of Df on Ca, i.e. Eq. (4.5), is confirmed at low capillary

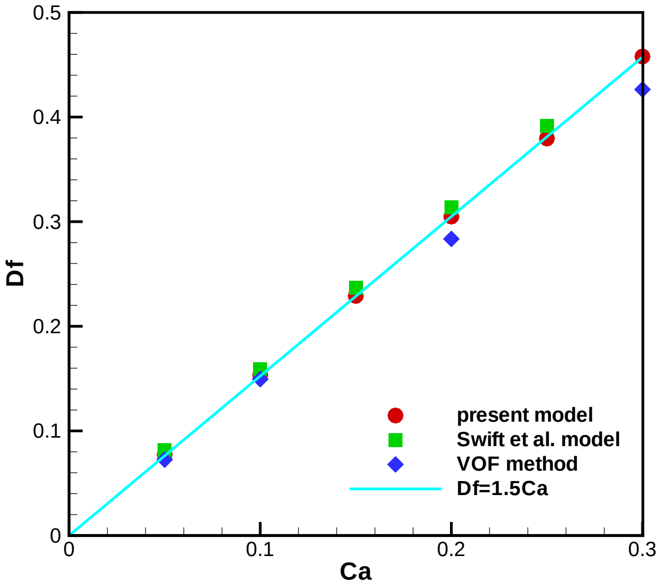

Figure 4.6: Taylor deformation parameter Df as a function of the capillary number.

numbers, where $Df = 1.5Ca$ is obtained based on the simulation results of the present model. Fig. 4.7 shows the steady state droplet shapes for various capillary numbers. Qualitatively, the profiles agree well with those profiles presented in Zhou and Pozrikidis [123]: all profiles cross two points. Finally, we find that the droplet breaks up at the critical capillary number Ca_{cr} between 0.9 and 1.0 for $Re = 1.0$, which is in agreement with the finding of Zhou and Pozrikidis [123]. Fig. 4.8 shows the comparison of the droplet evolution under simple shear flow for (a) $Ca = 0.9$ and (b) $Ca = 1.0$. The dimensionless time is defined as γt. We notice that at $Ca = 0.9$ the droplet will shrink once the maximal deformation is not enough to "pinch-off" the droplet. Also, the intermediate filament will shrink when the daughter droplets detach from the bulk at $Ca = 1.0$. These indicate that the droplet behaves elastically to some extent.

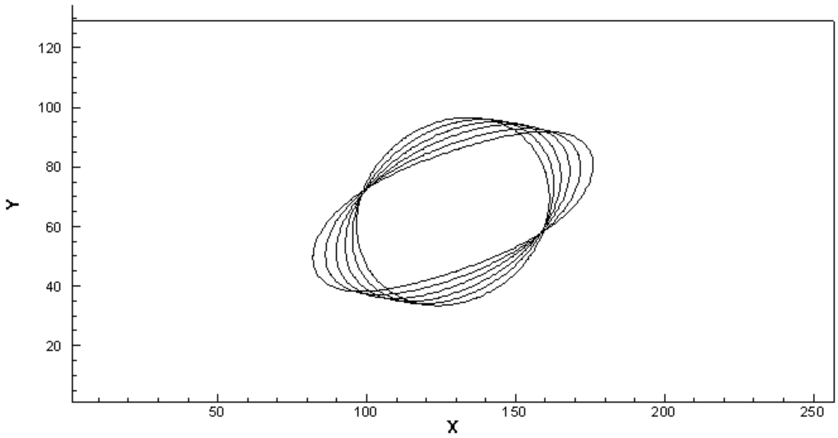

Figure 4.7: Stable droplet shape depicted as contour lines of $\phi = 0$, for various capillary numbers: $Ca = \{0.05, 0.1, 0.15, 0.2, 0.25, 0.3\}$.

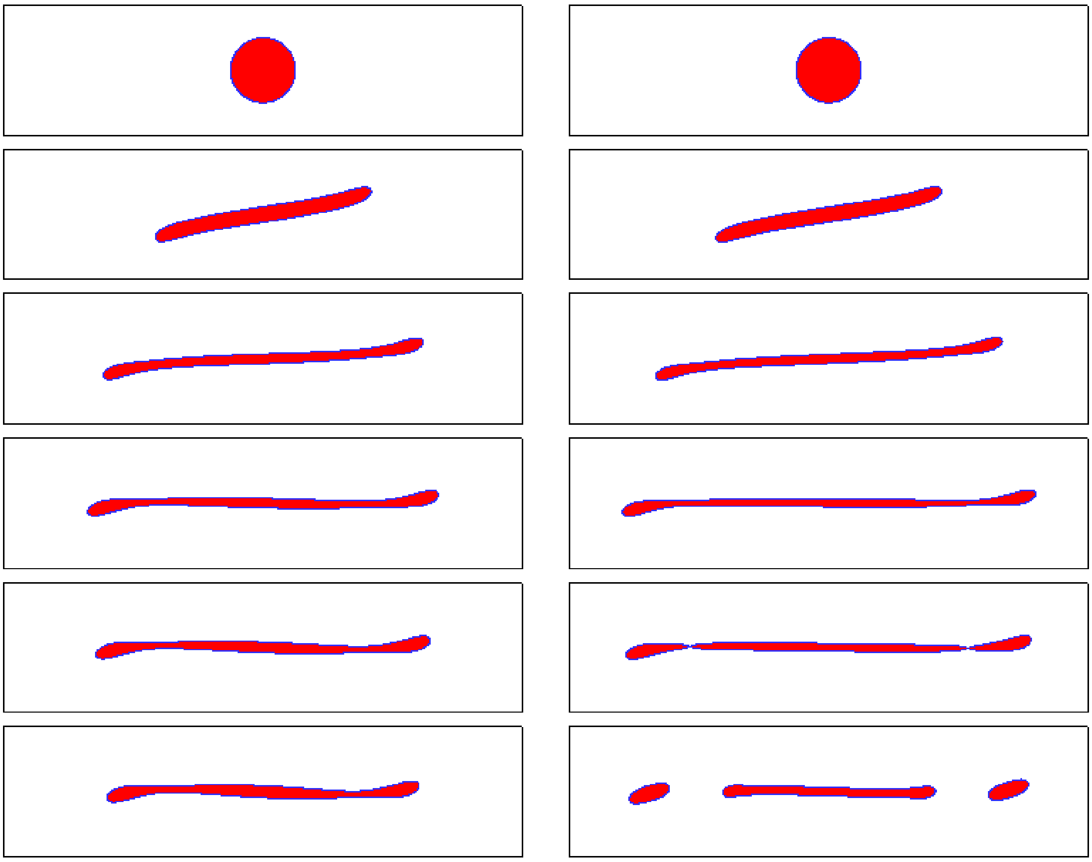

(a) $Ca = 0.9$ (b) $Ca = 1.0$

Figure 4.8: Snapshots of the droplet evolution under simple shear flow at $\lambda = 1$, $Re = 1.0$ for (a) $Ca = 0.9$ and (b) $Ca = 1.0$, taken at times $\gamma t = \{0, 6, 12, 24, 27, 30\}$.

4.2.2 Coalescence of two droplets with and without collision

Coalescence of droplets dispersed in a second immiscible fluid (i.e. matrix fluid) plays an important role in many industrial applications. These applications include emulsion stability, ink-jet printing, and coating applications. Since coalescence involves droplet interactions, it is intrinsically more complex than droplet breakup and more difficult to study either theoretically or experimentally. When the droplets are in contact, the inversion of the radius of curvature causes a singularity, forming a liquid bridge between the droplets. To demonstrate the ability of our model to handle singular topological changes, we first examine the inertial coalescence of two equal-sized droplets without collision, driven by the interfacial tension. We construct a 120×120 domain with two circular droplets located horizontally with a gap of d. The radius of droplets is $R = 20$ lattices ($R^{phy} = 120\ \mu m$). The periodic boundary condition is employed at all boundaries. The simulation parameters are chosen as: $\tau_f = 1.0$ and $\sigma = 0.002$ ($\eta^{phy} = 0.02$ Pa s and $\sigma^{phy} = 4.8$ mN/m). The gap of the two droplet d is fixed as 5 lattices ($d^{phy} = 30\ \mu m$), while the interface thickness parameter ξ and the mobility coefficient Γ are adjusted to investigate their influences on the coalescence.

Firstly, we set the interface thickness parameter as $\xi = 1.2\delta_x$ ($\xi^{phy} = 7.2\ \mu m$), and $\Gamma = 1.0$, so that the gap of the two droplets is larger than 4ξ. Simulation results are shown in Fig. 4.9. It can be easily seen that the two droplets do not coalesce at any time. When we maintain the interface thickness parameter at 1.2 lattices but set a larger value of $\Gamma = 100.0$, the simulation results are still the same as the above. Actually, even when the interface thickness parameter is increased to 1.25 lattices, the two droplets do not merge together.

The interface thickness is then set to $\xi = 1.3\delta_x$ ($\xi^{phy} = 7.8\ \mu m$) and $\Gamma = 10.0$. This is the case where the gap of two droplets is less than 4ξ. The other parameters are kept unchanged. The results are shown in Fig. 4.10. It can be easily seen that the two droplets merge together and eventually into a larger droplet. To show the influence of the mobility coefficient Γ on the coalescence, the interface thickness parameter is maintained as $\xi = 1.3\delta_x$ ($\xi^{phy} = 7.8\ \mu m$) and Γ value is reduced to 0.1. The other parameters are kept unchanged. The simulation results are shown in Fig. 4.11. The two droplets still coalesce. However, the coalescence process is slower then the case with $\Gamma = 10.0$.

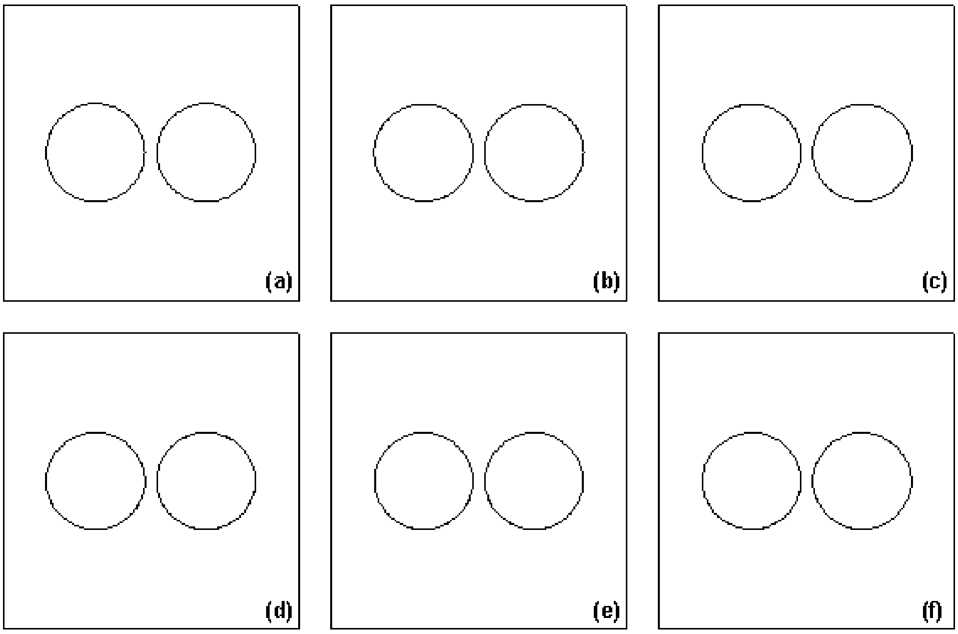

Figure 4.9: Two stationary droplets without coalescence for $\xi = 1.2\delta_x$, $d = 5.0\delta_x$ and $\Gamma = 1.0$ at time step: (a)t=0, (b)t=30000, (c)t=100000, (d)t=200000, (e)t=500000, (f)t=800000. The corresponding physical times are $t^{phy} = \{0, 9, 30, 60, 150, 240\}$ ms.

Based on the above simulation results, we can conclude that, for the two stationary droplets without collision, the gap between the droplets and the interface thickness are the major factors to decide whether the two droplets will coalesce together or not. When $d \geq 4\xi$, the two droplets will not coalesce. Otherwise, they both will coalesce together. The mobility coefficient Γ does not determine whether the two droplets will coalesce or not, but it can affect the velocity of coalescence, i.e., a larger Γ makes the two droplets merge together more quickly.

The shear induced coalescence described in Ref. [110] is investigated here. We only aim to examine the effect of mobility coefficient Γ (expressed as Pe_ϕ) on coalescence. The computational domain is taken as 180×120 lattices. Two droplets with radius $R = 20\delta_x$ are placed at symmetrical locations above and below the centre line of the shear flow in such a way that they can approach each other when the solid walls are set in motion. The initial differences in the x-coordinate and y-coordinate of the droplets are 20 and 80 lattices respectively. As in Yang et al. [124], the shear induced coalescence and separation can be divided into three stages: droplet transport, film drainage and coalescence or separation. Whether two droplets will coalesce or separate depends on the capillary number,

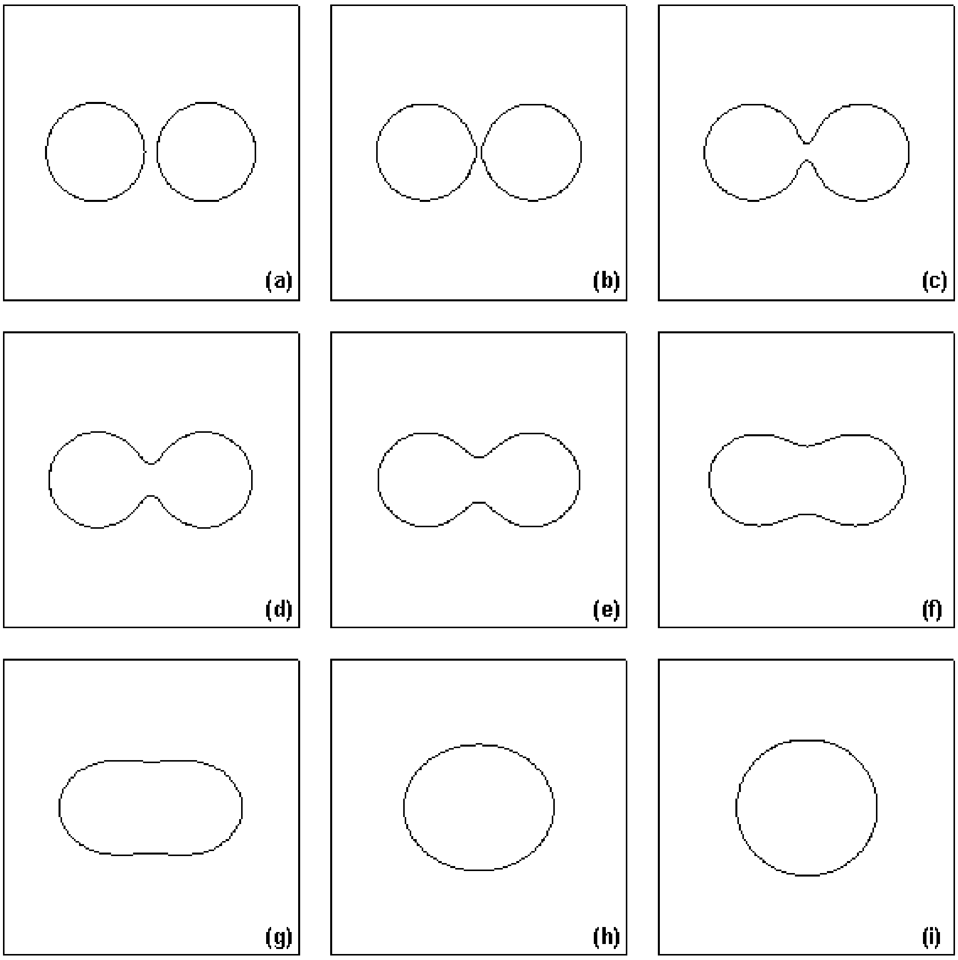

Figure 4.10: The coalescence of two droplets without collision for $\xi = 1.3\delta_x$, $d = 5.0\delta_x$ and $\Gamma = 10.0$ at time step: (a) t=0, (b) t=42000, (c) t=43000, (d) t=44000, (e)t=45000, (f)t=47000, (g)t=50000, (h)t=60000, (i)t=150000. The corresponding physical times are $t^{phy} = \{0, 12.6, 12.9, 13.2, 13.5, 14.1, 15, 18, 45\}$ ms.

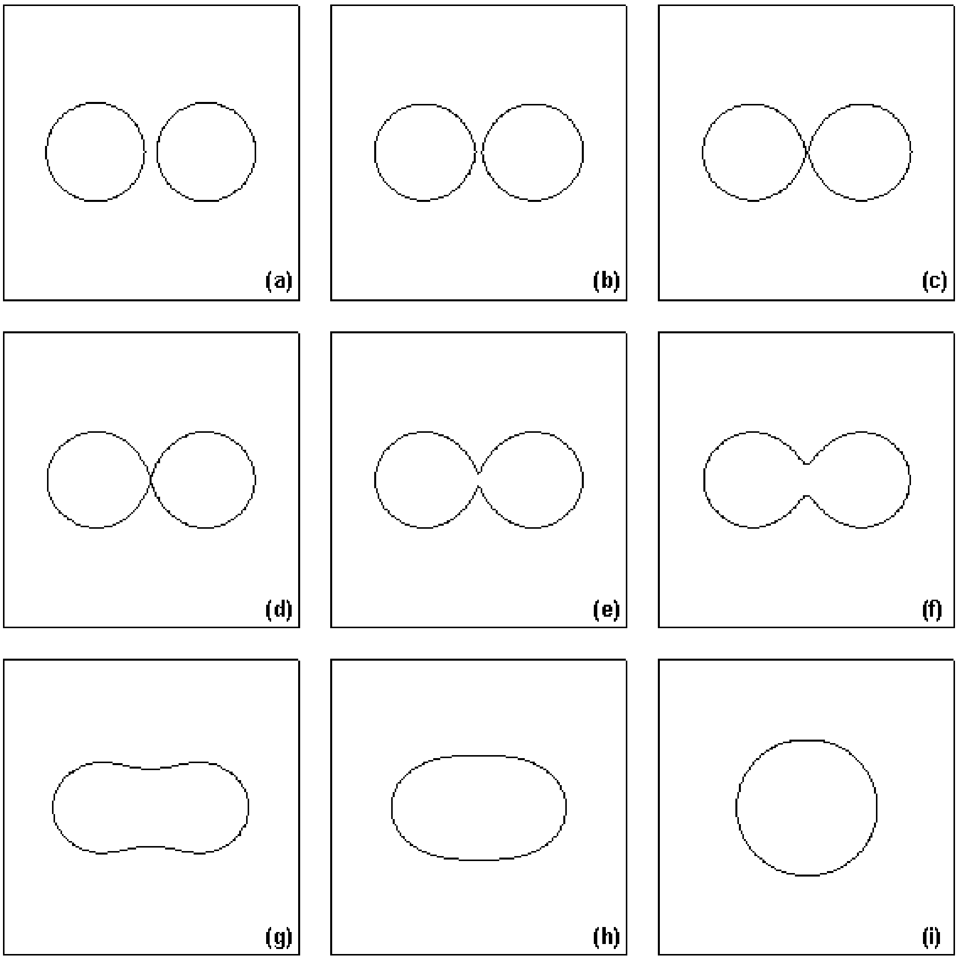

Figure 4.11: The coalescence of two droplets without collision for $\xi = 1.3\delta_x$, $d = 5.0\delta_x$ and $\Gamma = 0.15$ at time step: (a)t=0, (b)t=100000, (c)t=106000, (d)t=107000, (e)t=108000, (f)t=110000, (g)t=120000, (h)t=150000, (i)t=500000. The corresponding physical times are $t^{phy} = \{0, 30, 31.8, 32.1, 32.4, 33, 36, 45, 150\}$ ms.

the way of two droplets interact, and the interfacial properties. Fig. 4.12 and Fig. 4.13 show the simulation results for $Pe_\phi = 5$ and $Pe_\phi = 50$, respectively. All the other parameters are the same, which are chosen as: $Ca = 0.18$, $Re = 0.4$, $\xi = 2\delta_x$, and $\tau_f = 1.1$. Fig. 4.12 shows a shear-induced collision and coalescence at small Pe_ϕ (i.e. $Pe_\phi = 5$), and Fig. 4.13 shows a shear-induced non-contact collision at large Pe_ϕ (i.e. $Pe_\phi = 50$). Obviously, the small Pe_ϕ can help droplets to coalesce, which is consistent with the simulations given by Yu and Zhou [110] on droplets coalescence in viscoelastic matrix under shear using a traditional CFD solver with the phase-field model, as well as the experiments reported by Zdravkov [125] on two polymers with a big difference in molecular weight under planar extensional flow.

The effect of Pe_ϕ (Γ) on coalescence with collision induced by shear can be seen more clearly in the flowfield shown in Fig. 4.14. Zero and ±0.9 order parameter contour lines are shown as blue solid lines, small red lines with arrow denote the velocity vectors and green solid lines with big arrows denote the streamlines to show the trend of fluid motion. In the shear-induced collision-coalescence ($Pe_\phi = 5$), the overlap of the diffuse interface thickness can be observed and the matrix fluid between two droplets is drained out. Whereas in the shear-induced collision-separation ($Pe_\phi = 50$), little drainage of the matrix fluid is observed and two droplets rotate, which can be seen from the direction of streamline. This difference can be attributed to the Marangoni stresses because of the inhomogeneous interface thickness in the matrix film trapped between two droplets [110, 125]. In the phase-field model, the interface thickness is not uniform under shear force. The interface thickness increases near the elongated droplet tips and decreases near the short axes due to different stresses in different regions. As a result, the interfacial tension should not be the same everywhere for an elongated droplet in the flowfield. The non-uniform distribution of interfacial tension can cause Marangoni stresses. At small Pe_ϕ, the Marangoni stresses have the same direction with the drainage because of the larger order parameter value in the contact region, while the Marangoni stresses have the opposite direction with the drainage at large Pe_ϕ due to absence of interface overlap. It can be concluded that interface diffusion can affect whether the coalescence with collision occurs or not to some extent. However, we should note that the interface diffusion is (at least) not the decisive factor. In general, the most important factor should be the hydrodynamic forces.

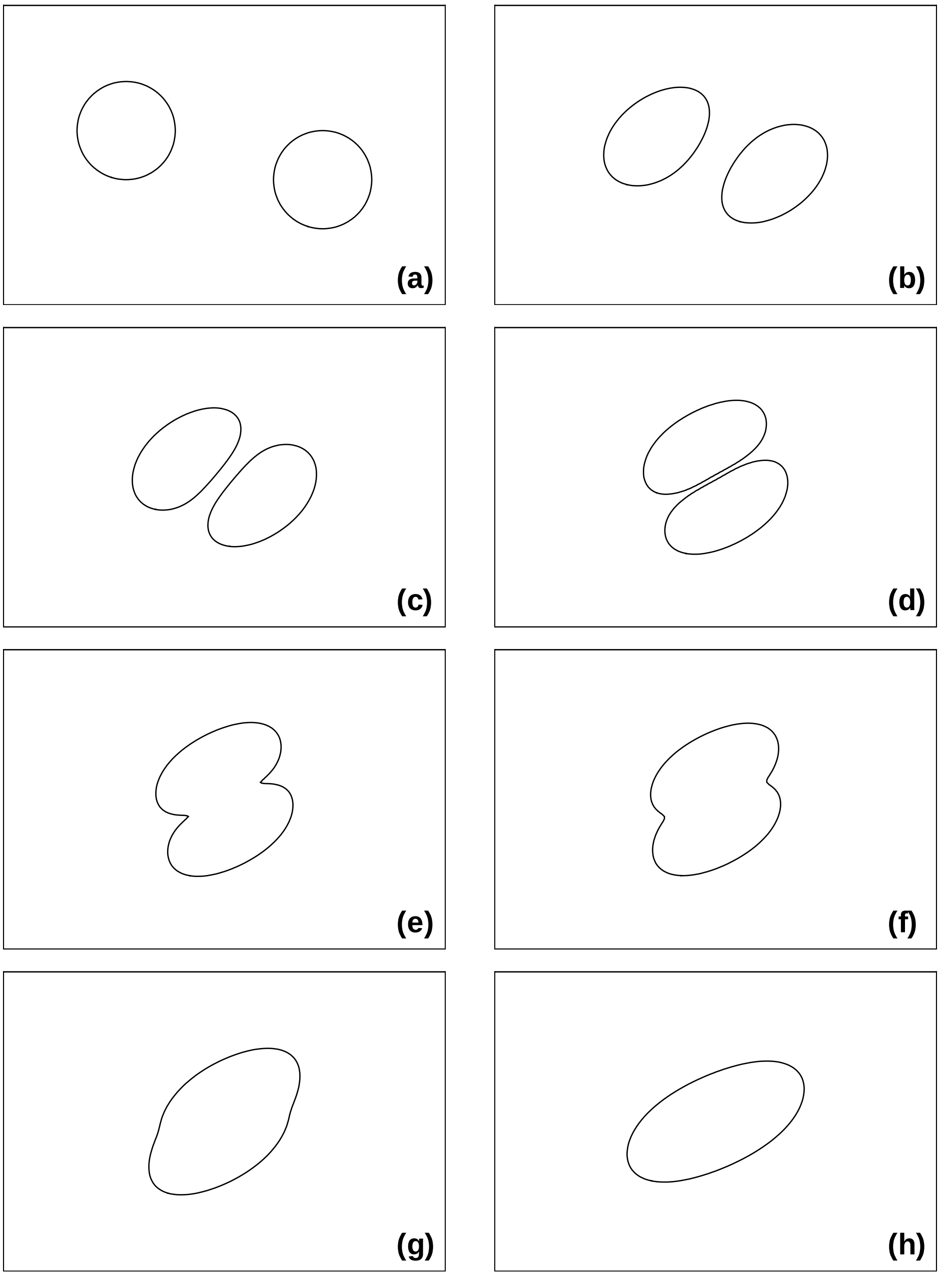

Figure 4.12: The collision-coalescence of two droplets in shear flow at time: (a)$\gamma t = 0$, (b)$\gamma t = 2$, (c)$\gamma t = 4$, (d)$\gamma t = 5.8$, (e)$\gamma t = 6$, (f)$\gamma t = 6.2$, (g)$\gamma t = 6.6$, (h)$\gamma t = 30$. The parameters are $Ca = 0.18$, $Re = 0.4$ and $Pe_\phi = 5$.

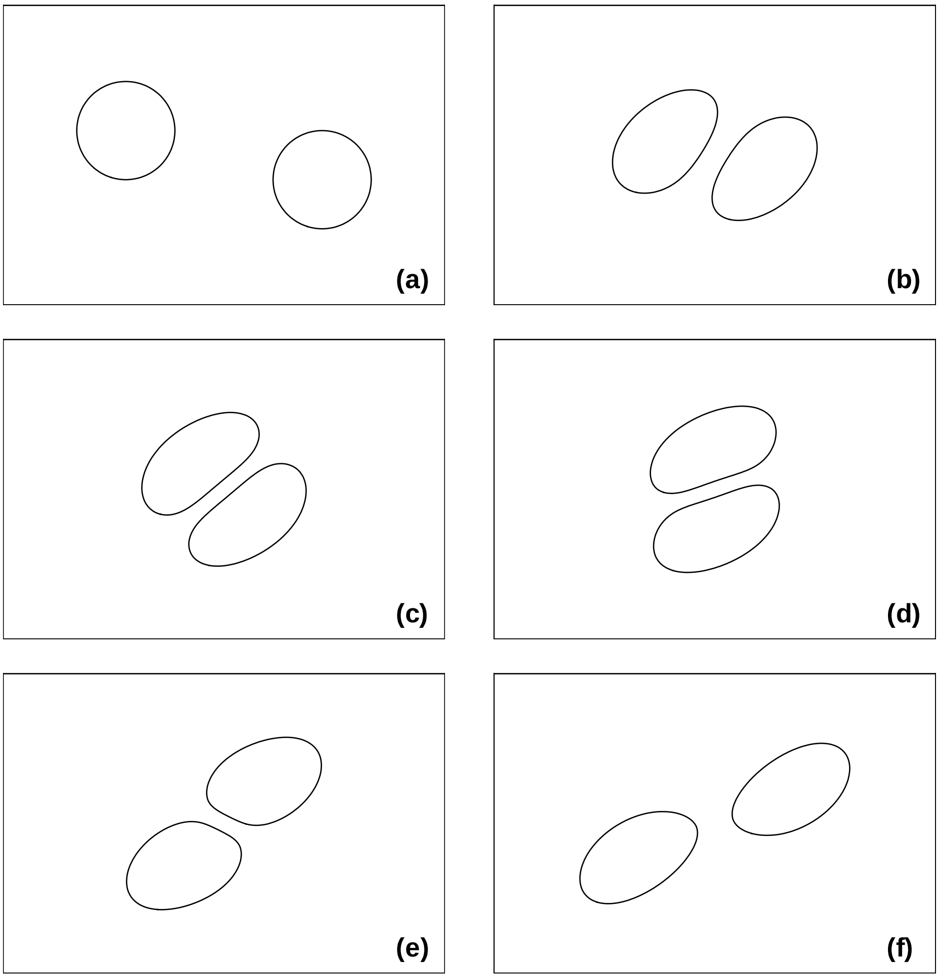

Figure 4.13: The non-contact collision of two droplets in shear flow at time: (a)$\gamma t = 0$, (b)$\gamma t = 3$, (c)$\gamma t = 6$, (d)$\gamma t = 7$, (e)$\gamma t = 8$, (f)$\gamma t = 9$. The parameters are $Ca = 0.18$, $Re = 0.4$ and $Pe_\phi = 50$.

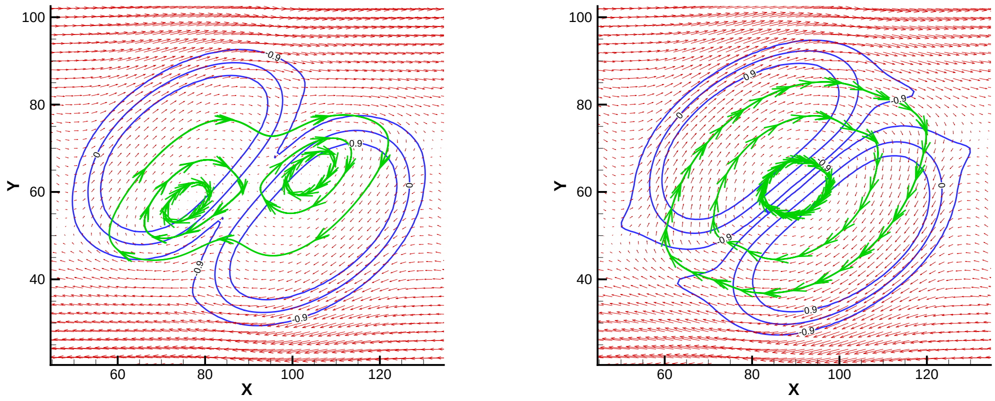

(a) $Pe_\phi = 5$ (b) $Pe_\phi = 50$

Figure 4.14: The velocity fields for two droplets with collision-coalescence and with non-contact collision. The blue solid lines show zero and ±0.9 order parameter contour lines, the small red lines with arrow denote the velocity vectors and the green solid lines with big arrows denote the streamlines to show the trend of fluid motion.

4.2.3 Contact-line motion

To show whether our method can model contact-line motion, a droplet attached on a substrate in a shear flow is investigated. We examine the advancing contact angle θ_A, the receding contact angle θ_R and droplet velocity u_d when the shear is induced by moving the upper wall at a constant velocity u_w. As shown in Fig. 4.15, the two walls are separated by a distance H. The lower wall is kept stationary, and the upper walls moves towards the right with a constant velocity u_w. Periodic boundary conditions are applied in the x-direction. The advancing and receding contact angles are both defined as the angles measured from the droplet side of the contact line. The capillary number, Reynolds number and Peclet number are defined as in Eq. (4.3), where the shear rate is chosen as $\gamma = u_w/H$. We run the simulations in a 256×64 lattice domain. The initial droplet radius is $R = 32$ lattices and the initial droplet centre is $(X_c, Y_c) = (64, 0)$. Both fluids have the same viscosity, which is given by $\eta = 0.1$. The interfacial tension is set to be $\sigma = 1 \times 10^{-3}$. Without losing generality, here we only consider the solid wall with neutral wetting ($\phi_w = 0$).

To investigate the effect of the wall velocity on droplet motion, we only vary the wall velocity u_w (expressed as Ca) and keep all the other parameters fixed. Note that the mobility is fixed as $M = 0.5$ in the current study, so the Peclet

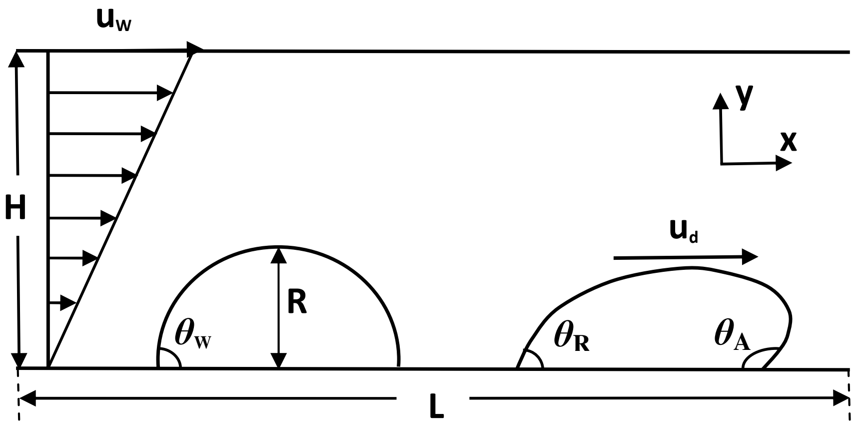

Figure 4.15: A schematic illustration of the simulation geometry to examine contact-line motion. The droplet on the left is in the original shape before the start of flow, while the one on the right is deformed by the shear flow.

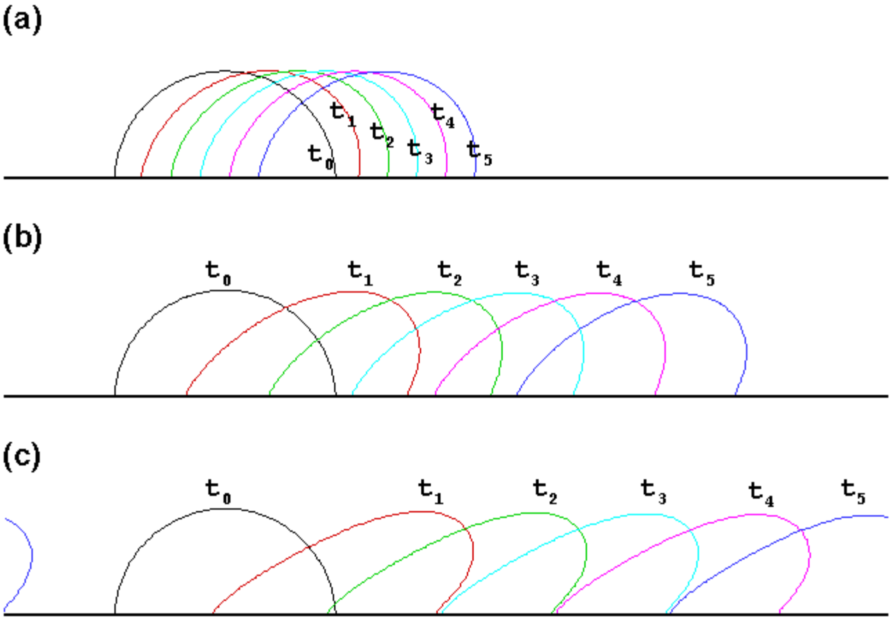

Figure 4.16: The snapshots of droplet sliding on a solid wall under shear for (a) $Ca = 0.05$ and $Re = 0.16$, (b) $Ca = 0.15$ and $Re = 0.48$, and (c) $Ca = 0.225$ and $Re = 0.72$. The time steps are taken as $t_0 = 0$, $t_1 = 100000$, $t_2 = 200000$, $t_3 = 300000$, $t_4 = 400000$, and $t_5 = 500000$, respectively.

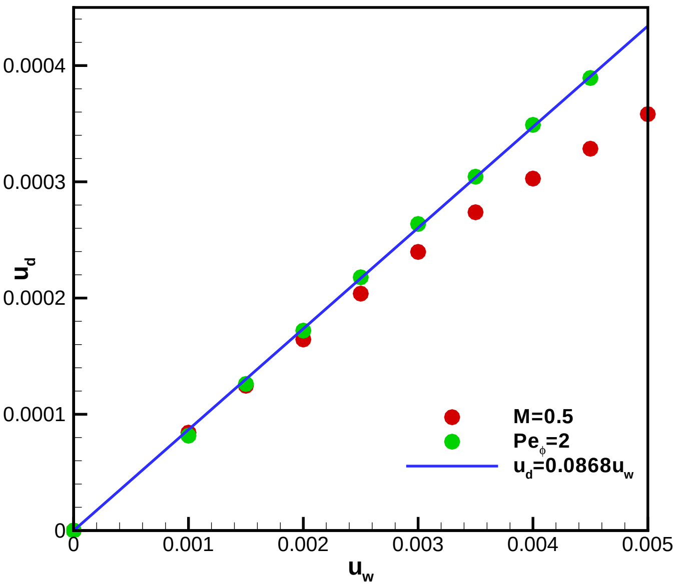

Figure 4.17: Droplet velocity vs. moving wall velocity. The red symbols are the simulation results of $M = 0.5$, and the green symbols are the simulation results of $Pe_\phi = 2$. The solid line is a linear fitting of the simulation results with $Pe_\phi = 2$.

number Pe_ϕ increases as Ca increases. When Ca is increased from 0 to 0.4 (the corresponding wall velocity increased from 0 to 0.008), we find that the motion of the droplet can experience two modes. One is the slip mode where the droplet slides along the wall and steady-state exists for the droplet shape and velocity. The other is the breakup mode where the droplet is divided into two droplets when the capillary number increases to some critical value ($Ca_{cr} > 0.25$).

Fig. 4.16 shows the snapshots of droplet motion in the slip mode (i.e. $Ca < Ca_{cr}$) for (a) $Ca = 0.05$ and $Re = 0.16$, (b) $Ca = 0.15$ and $Re = 0.48$, and (c) $Ca = 0.225$ and $Re = 0.72$. Under a small shear rate the droplet deforms slowly first, then starts to move, and finally ceases to deform when reaching a certain shape with a constant moving velocity u_d. As the capillary number increases, the droplet deformation and the moving velocity increase. We also notice that the height of droplets during the deformation seems to be the same as in the initial state. To highlight the influence of Pe_ϕ on the droplet motion, we carry out the simulations with a fixed Peclet number ($Pe_\phi = 2$) and keep all the other parameters as in the above simulations with fixed mobility M. Fig. 4.17 shows the relationship between the wall velocity u_w and droplet moving velocity u_d in

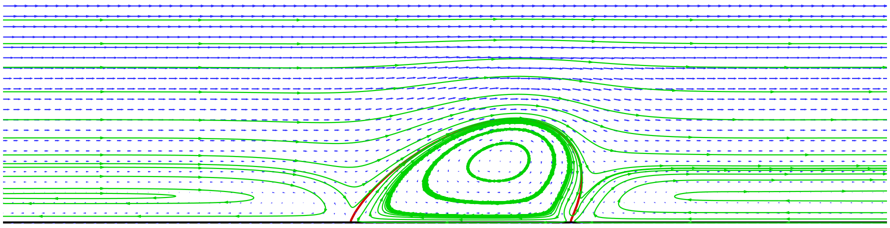

Figure 4.18: Steady flowfield (relative to the moving droplet) around a droplet for $Ca = 0.15$, $Re = 0.48$ and $M = 0.5$. The red contour represents the droplet interface, the green lines represent the streamlines, and small blue lines with arrow represent the velocity vectors.

the slip mode for $M = 0.5$ (red discrete symbols) and $Pe_\phi = 2$ (green discrete symbols). The droplet velocity u_d is calculated by

$$u_d = \sum_{i,j} u_{i,j} N(\phi_{i,j}) / \sum_{i,j} N(\phi_{i,j}), \tag{4.6}$$

where the function $N(\phi)$ is defined as

$$N(\phi) = \begin{cases} 1 & (\phi > 0) \\ 0 & (\phi \leq 0). \end{cases} \tag{4.7}$$

It can be clearly seen that the droplet velocity u_d exhibits a linear dependence on the wall velocity for the fixed Pe_ϕ, i.e. $u_d = 0.0868 u_w$. However, the droplet velocity gradually deviates from the linear relationship as the wall velocity increases for a fixed mobility. This is because the Peclet number increases (larger than 2) with an increase in u_w for a fixed M. So one can expect that a larger Pe_ϕ slows down the droplet motion on the wall. It should be noted that, since the lower wall is stationary and the droplet keeps a fixed shape upon reaching the steady state, u_d is actually the slip velocity of the contact line. To indicate the flowfield around the droplet, a snapshot of the steady state (with the velocity vectors in a frame moving with the droplet) is shown in Fig. 4.18. From Fig. 4.18, it can be seen that the shear flow far above from the droplet is only slightly disturbed; as the flows approach the droplet, the streamlines are increasingly deformed. Also, in the lower region containing the droplet, two circulations are observed: one is inside the droplet and the other is outside, which is relatively flat (note that in Fig. 4.18 the outside circulation is separated into two parts on the left and right sides of the droplets which can be connected together because the periodic boundary conditions are applied in the x-direction).

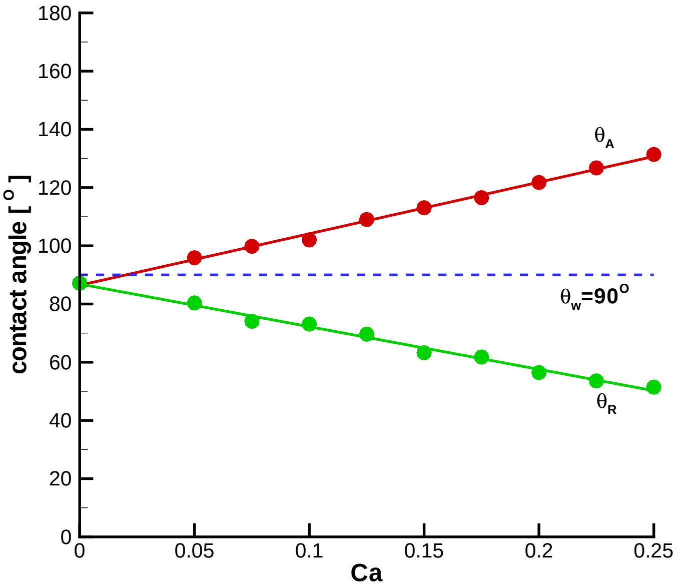

Figure 4.19: Dynamic contact angles as a function of capillary number. The red and blue symbols are the simulation results of the advancing contact angle θ_A and the receding contact angle θ_R, and the red and blue sold lines are the linear fitting of the simulation results θ_A and θ_R, respectively. In the simulations, the order parameter of wall is set to be $\phi_w = 0$, so that the equilibrium contact angle is $\theta_w = 90°$, which is represented by a dashed line.

Fig. 4.19 gives the relationship between the capillary number Ca and the dynamic contact angles θ_A and θ_R in the slip mode for $M = 0.5$. It is observed again that the droplet can stay steady even though both contact angles θ_A and θ_R deviate from the static contact angle θ_S (where $\theta_S = \theta_A|_{Ca\to 0} = \theta_R|_{Ca\to 0} = 87.15°$) when the droplet is moving on the wall. It should be noted that all the contact angles are calculated by the coordinates of the nearest two fluid nodes close to the wall. Also, the wall is actually located between the first fluid node and the solid node because a half-way bounce-back boundary condition is imposed at the wall. Therefore, it is not surprising that the calculated static contact angle θ_S is slightly smaller than its given value $\theta_w = 90°$. We can also notice $\theta_R \le \theta_S \le \theta_A$, which is consistent with the usual concept of contact angle hysteresis [126]. On the basis of our simulation results, it can be found that the advancing contact angle and the receding contact angle both approximately exhibit a linear dependence on

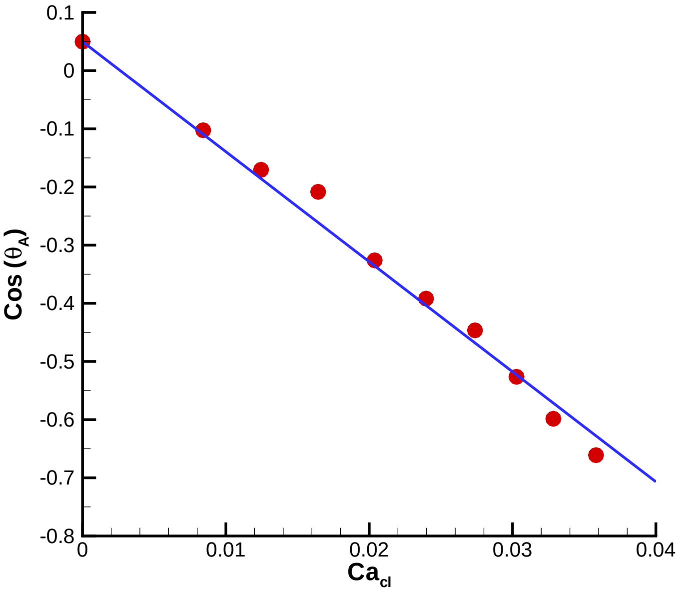

Figure 4.20: The advancing contact angle θ_A as a function of Ca_{cl} at $M = 0.5$. The discrete symbols are the simulation results and the solid line is the linear fit of $\cos(\theta_A)$ to Ca_{cl}.

the capillary number, i.e. $\theta_A = 87.15 + 173.07Ca$ and $\theta_R = 87.15 - 148.11Ca$.

Based on the contact-line velocity u_{cl} (which is equal to u_d as stated above), we define a new capillary number, $Ca_{cl} = u_{cl}\eta/\sigma$, which we call the contact-line capillary number in this study to differentiate with the capillary number Ca. To lowest order in Ca_{cl}, the advancing contact angle is related to the static contact angle θ_S and the capillary number Ca_{cl} by [127]

$$\cos(\theta_A) = \cos(\theta_S) - Ca_{cl} \ln(KL/l_s), \tag{4.8}$$

where K is a constant, L is the length scale of the system, and l_s is the effective slip length at the three phase contact line. Fig. 4.20 gives the measured contact angle θ_A as a function of Ca_{cl} at $M = 0.5$. As expected, our simulation results show a linear decrease of $\cos(\theta_A)$ with the contact-line capillary number Ca_{cl}. Finally, Fig. 4.21 gives the evolution of the droplet in the breakup mode with $Ca = 0.3$, $Re = 0.96$ and $M = 0.5$. In the process of droplet breakup the contact-line motion is instantaneously varying, so the time-related studies are required to understand the contact-line dynamics. This is not included in this thesis.

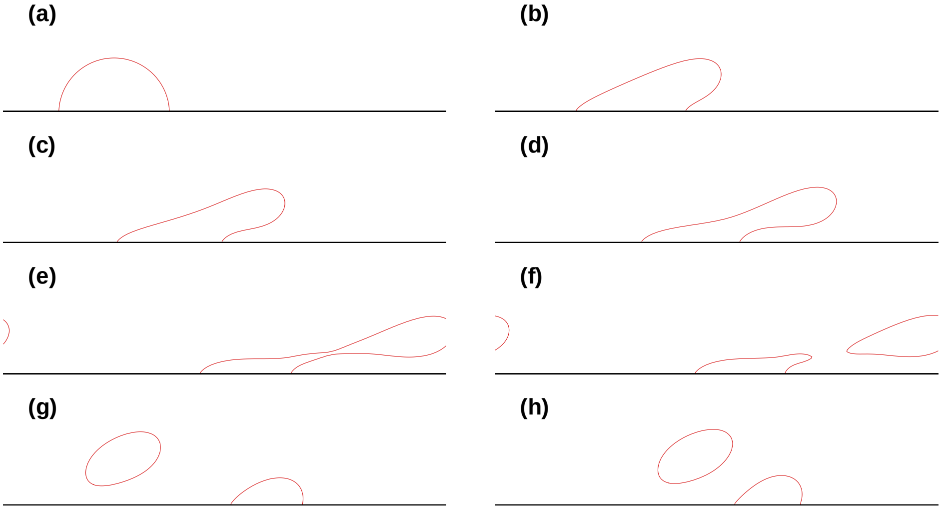

Figure 4.21: The snapshots of droplet breakup on a solid wall under shear at $Ca = 0.3$, $Re = 0.96$ and $M = 0.5$ for: (a) γt=0, (b) γt=4.69, (c) γt=9.38, (d) γt=14.06, (e) γt=21.56, (f) γt=22.03, (g) γt=26.25, and (h) γt=28.13.

4.3 Conclusions

The simulations of stationary droplet flow and static contact angle have demonstrated that the binary phase-field LB model can easily and accurately capture droplet behaviour. A series of simulations have been carried out on droplet deformation, breakup, coalescence, collision and contact line motions in microfluidic devices using this model. The influences of some flow and numerical parameters on droplet dynamic behaviour are studied. The following conclusions are drawn:

1. In contrast to some existing LB multiphase models, the present model can significantly reduce unphysical spurious velocities at the interface. In particular, it is very direct and simple to implement boundary conditions including wetting boundary condition. The present model can overcome the disadvantages of Swift's free energy model for treating the wetting boundary, in which strong spurious velocities in the steady state lead to incorrect results for the equilibrium contact angle when the both fluids have different viscosities.

2. The droplet deformation between two shearing plates shows that, the Taylor deformation parameter is a linear function of capillary number for small droplet deformation, and the droplet breakup occurs at a critical capillary number $0.9 < Ca_{cr} < 1.0$ for $Re = 1.0$.

3. Simulation results on the coalescence of two stationary droplets driven by interfacial tension indicate that: whether the two droplets will coalesce or not is completely determined by their gap and the interface width. Droplets with high diffusion ability can coalesce easier and faster when the coalescence occurs.

4. The coalescence process of two droplets in simple shear flow is found to be greatly dependent on the diffuse property of the interface. For convection-dominated case (large Pe_ϕ), the diffusion of the order parameter is greatly inhibited, and an overlap of the interfacial layer will not happen, which results in the final separation of two droplets.

5. The simulation results of contact line dynamics for a droplet attached to a substrate in a shear flow show two droplet motion modes including the slip mode and the breakup mode. In the slip mode, the droplet deforms and finally reaches the fixed shape and moving velocity. The moving velocity of droplet is a linear function of the wall velocity for a fixed Peclet number. It is identified that large interface mobility (i.e. small Peclet number) can accelerate the contact line motion. In addition, the contact angle hysteresis phenomenon is reproduced by the present model. The advancing and receding contact angles both exhibit a linear dependence on the wall velocity. It is found that the advancing contact angle can be correlated with the contact line velocity through a scaling equation.

Chapter 5

Droplet formation in a T-shaped microfluidic junction

For many microfluidic microdroplet applications, it is important to generate mono-dispersed droplets in a continuous flow. T-junctions are one of the most frequently used microfluidic geometries to produce immiscible fluid segments (plugs) and droplets. Although much experimental work has been done on understanding droplet formation in microfluidic T-junctions, the available information is fragmented due to differences in channel dimensions, flow rates, and materials used. As a numerical study can be complementary to an experimental investigation, our multiphase LB model, using the phase-field theory to describe interfacial interactions, is employed to investigate the droplet formation in a microfluidic T-junction. The influence of capillary number, flow rate ratio, viscosity ratio, and contact angle on droplet breakup, size, and detachment is to be systematically studied.

We study droplet formation in a T-junction microchannel, as illustrated in Fig. 5.1, consisting of a main channel with width w_c and a lateral channel with width w_d. Both w_c and w_d are 100 μm in the current simulations. The continuous phase oil is introduced at the inlet of the main channel, and the dispersed phase water is injected into the lateral channel. To quantitatively understand the underlying flow physics, we need 3D simulations to resolve intermolecular interactions at the interface and their effect on the hydrodynamics. However, to accurately resolve an interface with a typical thickness of 1nm and surrounding fluid flowfield, it is still not practical to use the phase-field calculation with today's computer technology. Therefore, we run our simulations in 2D to un-

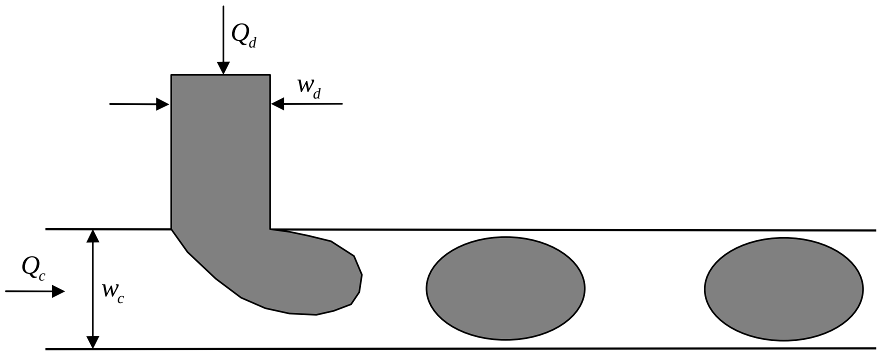

Figure 5.1: Schematic illustration of the droplet generation in a microfluidic T-junction, where w_c, w_d are the widths of the main and lateral channels, and Q_c and Q_d are the inlet volumetric flow rates of the continuous and dispersed phases.

derstand flow physics qualitatively. The computational domain consists of 300 × 60 lattices and each lattice spacing corresponds to 5μm. In all the cases, we find that mesh refinement will lead to results variations no more than 5%. In the following, we will use the subscripts 'c' and 'd' to refer to the continuous and dispersed phases, respectively.

In the numerical solution, the interfacial thickness parameter ξ is a free parameter. In order to keep a sharp phase interface, ξ should be chosen to be a small value. However, if ξ is too small, numerical inaccuracy and instability will occur at the interface. For a finite interface thickness, straining flows can thicken or thin the interface, which must be resisted by diffusion. Meanwhile, large diffusion will excessively damp the flow. Therefore, appropriate balance between the convection and diffusion effects at the interface is important which can be described by the Peclet number, Pe:

$$Pe = \frac{u_c w_c}{MA}, \tag{5.1}$$

where the average inlet velocity u_c and inlet width w_c of the continuous phase are chosen to be the characteristic velocity and length of the system. In our simulations, we compromise to have ξ of 2 lattice grids, so that the interface is resolved typically 5 ∼ 6 grids, and Pe is of $\mathcal{O}(10) \sim \mathcal{O}(100)$.

Flow behavior in a microfluidic T-junction can be classified by a group of dimensionless parameters, which are commonly defined by the experimentally measurable variables e.g. the interfacial tension, the inlet volumetric flow rates (Q_c and Q_d) and viscosities (η_c and η_d) of the two fluids. For a typical microfluidic system, the Reynolds number is so small that inertial effects can be neglected.

The Bond number is also negligibly small due to the small density difference of the two immiscible liquids. In contrast, the capillary number (Ca), which describes the relative importance of the viscosity and the interfacial tension, is a most important parameter for droplet generation and defined by the average inlet velocity u_c and the viscosity η_c of the continuous phase, and the interfacial tension σ as

$$Ca = \frac{\eta_c u_c}{\sigma} = \frac{\eta_c Q_c}{\sigma w_c}. \tag{5.2}$$

An additional important dimensionless parameter is the ratio of flow rates ($Q = Q_d/Q_c$). The viscosity ratio ($\lambda = \eta_d/\eta_c$) and fluid/surface interaction also play important roles in droplet formation process, which has been experimentally observed [54, 128]. In order to achieve consistent droplet breakup, it is necessary that the continuous phase liquid should preferentially wet the walls. The magnitude of wettability will be described by a static contact angle θ_w. Here, we will examine the roles of these parameters in droplet formation.

5.1 Influence of the capillary number

A series of simulations are performed with the interfacial tension $\sigma = 0.0036$, the viscosity of the continuous phase $\eta_c = 0.016$ and the viscosity ratio $\lambda = 1/4$. The densities of both fluids are assumed to be unity. The contact angle $\theta_w = 180°$ so that the continuous phase fluid completely wets the walls, while the dispersed phase fluid is non-wetting. In order to compare our simulation results with the experimental data [18, 46, 129], we choose Q_d=0.004, 0.006 and 0.008 in the simulations. For convenience, all quantities are expressed in the lattice units except the droplet diameter, which is in the physical unit. As described in Section 3.3, we need to choose three reference quantities to match these LB simulation parameters to their physical values. Specifically, $L_0 = 5 \times 10^{-6}$ m, $T_0 = 10^{-7}$ s and $M_0 = 1.25 \times 10^{-13}$ kg in this study. Following the forementioned criterion, for example, we can obtain the physical value of interfacial tension σ^{phy} by: $\sigma^{phy} = \sigma \frac{M_0}{T_0^2} = 0.0036 \frac{1.25\times10^{-13}}{(10^{-7})^2} = 0.045$ N m^{-1}, and the physical value of continuous phase viscosity η_c^{phy} by: $\eta_c^{phy} = \eta_c \frac{M_0}{L_0 T_0} = 0.016 \frac{1.25\times10^{-13}}{5\times10^{-6}\cdot10^{-7}} = 4 \times 10^{-3}$ Pa s.

Fig. 5.2 shows the snapshots of droplet formation in the T-junction. The droplet deforms before detachment, and the necking of the dispersed phase is initiated once the continuous phase fluid intrudes into the upstream side of the

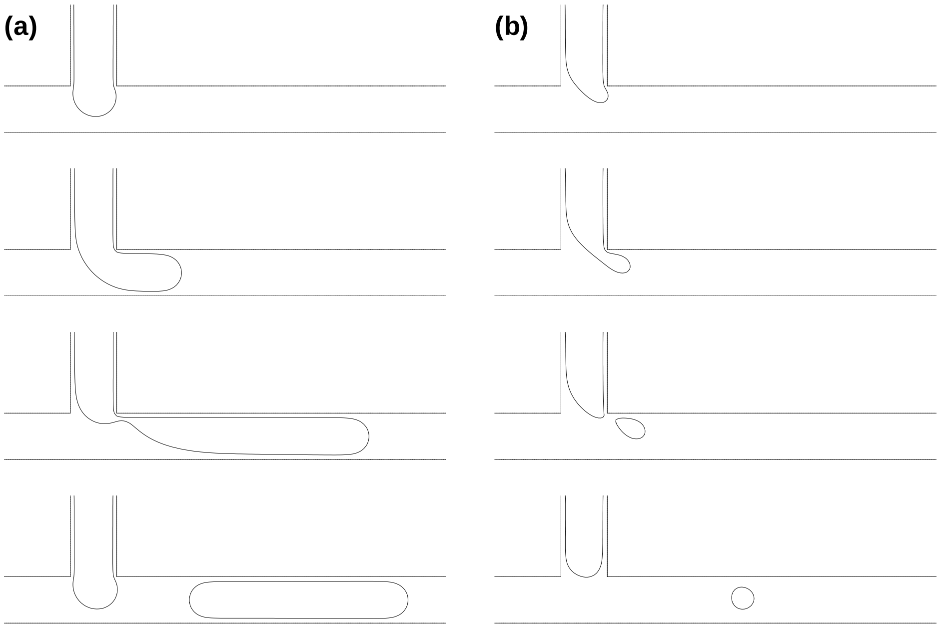

Figure 5.2: The snapshots of droplet formation: (a) Ca=0.00056, $Q_d = 0.004$; and (b) Ca=0.059, $Q_d = 0.008$.

lateral channel. The intrusion of the continuous phase accentuates the influence of the contact line dynamics, which is thought to be indispensable for the droplet detachment. Fig. 5.2 shows that the necking occurs soon after the dispersed phase streams into the main channel when Ca is large ($Ca = 0.059$), while the plugs are formed when Ca is small ($Ca = 0.00056$). The current simulation results agree well with the experimental observations [18, 46]. Fig. 5.3 shows that the droplet diameter becomes smaller when Ca increases for a fixed dispersed phase flow rate, and is very weakly dependent on the dispersed phase flow rate. Here, we define the diameter of a non-spherical droplet as the diameter of a spherical droplet with the same volume.

In both experiment [48] and simulation [21], van der Graaf et al. found that the final droplet volume is a result of a two-stage droplet growth. Initially, the droplet grows to a critical volume V_c until the forces exerted on the interface achieve balance. Subsequently, the droplet continues to grow for a time t_n for necking due to the continuous injection of the dispersed phase fluid. And the final droplet volume V can be described by [48]

$$V = V_c + t_n Q_d. \tag{5.3}$$

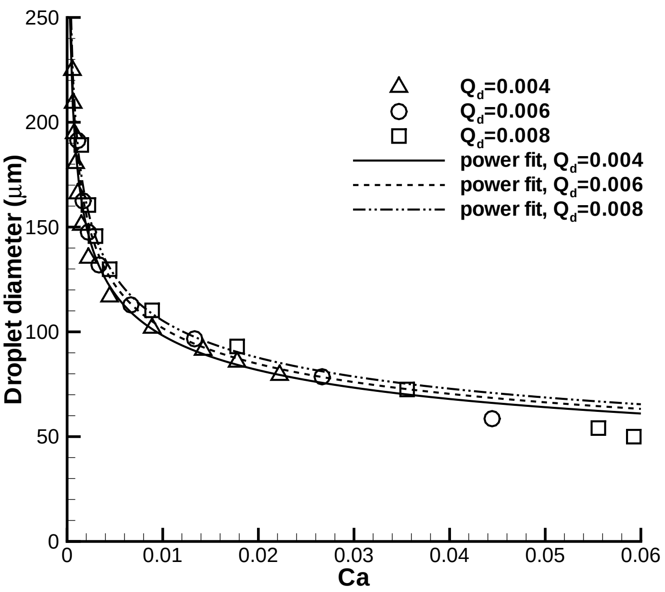

Figure 5.3: The effect of the capillary number on the droplet diameter at the dispersed phase flow rates Q_d of 4×10^{-3}, 6×10^{-3} and 8×10^{-3} respectively. The lines represent the power fittings of the simulation results

V_c depends only on Ca and the duration of necking t_n decreases as Ca increases. An empirical relationship was proposed to predict the droplet volume by van der Graaf et al. [21]:

$$V = V_{c,ref} Ca^m + t_{n,ref} Ca^n Q_d, \tag{5.4}$$

where $V_{c,ref}$ and $t_{n,ref}$ are the reference values at $Ca = 1$ (the droplet detachment process is very fast, i.e. $t_n \to 0$); the exponents m and n depend on the device geometry. In our simulation, we find that $m = n = -0.78$, while $m = n = -0.75$ were also reported by van der Graaf et al. [21].

5.2 Influence of the flow rate ratio

Here, we study the influence of the flow rate ratio on droplet formation in the T-junction over a broad range of capillary numbers. Three different flow rate ratios $Q = 1/8,\ 1/4$, and $1/2$ are used in the simulations. For each flow rate ratio, the capillary number varies from 0.004 to 0.056, typically found in microfluidic droplet generation. The wetting conditions and the densities of both phases are kept the same as in the previous section. The interfacial tension σ is now set to be 0.005. The viscosity of the continuous phase fluid η_c is 0.08, and the viscosity ratio λ is 1/8.

As shown in Fig. 5.4, when the capillary number is low i.e. $Ca = 0.006$, the incoming dispersed phase fluid tends to occupy the full width of the main channel, and the breakup occurs at the downstream corner of the T-junction. When the capillary number increases i.e. $Ca = 0.032$, 0.056, the dispersed phase fluid occupies only part of the main channel, and smaller droplets are formed. According to Ca, we find two distinguished droplet generation regimes i.e. the squeezing and dripping regimes. In the squeezing regime when Ca is small, the buildup of pressure in the upstream due to the obstruction of the main channel by the emerging droplet plays a dominant role in “pinching off” the droplet, while the viscous shear force becomes increasingly important in the dripping regime when Ca increases.

Fig. 5.4 clearly shows the effect of Q and Ca on the droplet detachment point. For small Q, i.e. $Q = 1/8$, the droplets are pinched off at the T-junction corner for all the capillary numbers. However, for $Q = 1/4$ and 1/2, increasing Ca will force the detachment point to move from the corner to the downstream. When Ca is 0.006, varying Q from 1/8 to 1/2 does not change the detachment point of the droplet. When Ca is 0.032 and 0.056, increasing Q will move the detachment point from the T-junction corner to the downstream. In addition, we find the droplet detachment point gradually moves downstream until a stable jet is formed when we increase Ca and Q, which was also observed in both simulation [22] and experiment [23].

Fig. 5.5 gives the predicted droplet diameter as a function of the capillary number for three different flow rate ratios. The droplet grows as the flow rate ratio increases but its diameter decreases as the capillary number increases. For all Q, we can clearly identify two distinguished squeezing and dripping regimes with the same critical capillary number, $Ca_c = 0.018$. In the squeezing regime, the flow rate ratio shows significant effect on the droplet size. While in the dripping regime, the effect of the flow rate ratio diminishes as Ca increases, which was also recently reported by Menech et al. [22] using the Navier-Stokes solver with a phase-field model. The influence of the flow rate ratio was numerically investigated in [22] for both squeezing and dripping regimes, where the critical capillary number of 0.015 was found for the squeezing and dripping transition. However, the recent experimental study by Christopher et al. [23] did not observe the critical capillary number during the squeezing-to-dripping transition.

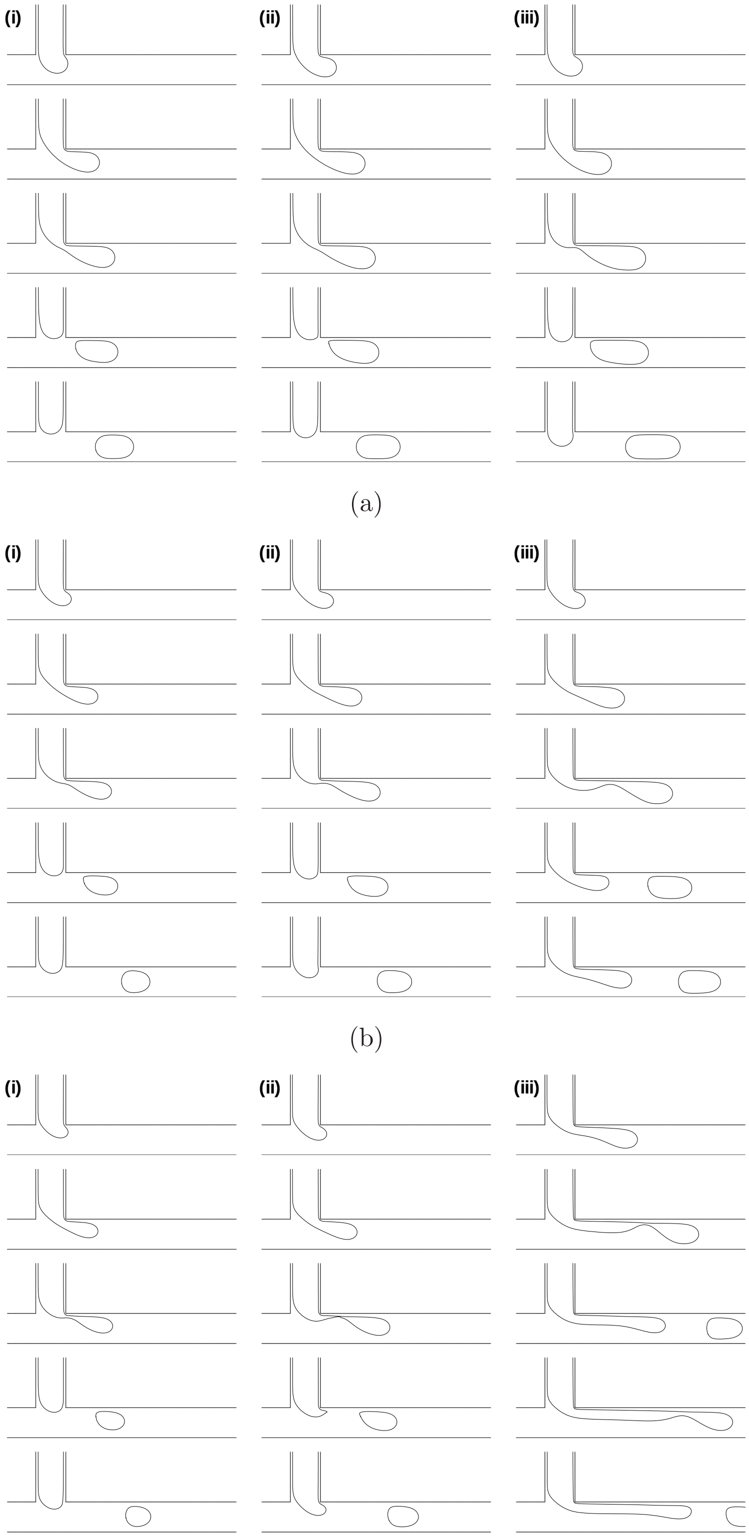

(a)

(b)

(c)

Figure 5.4: The effect of the capillary number and the flow rate ratio in droplet formation process with a fixed viscosity ratio, i.e. $\lambda = 1/8$: (a) $Ca = 0.006$; (b) $Ca = 0.032$; (c) $Ca = 0.056$; and the flow rate ratio Q is: (i) 1/8; (ii) 1/4; and (iii) 1/2.

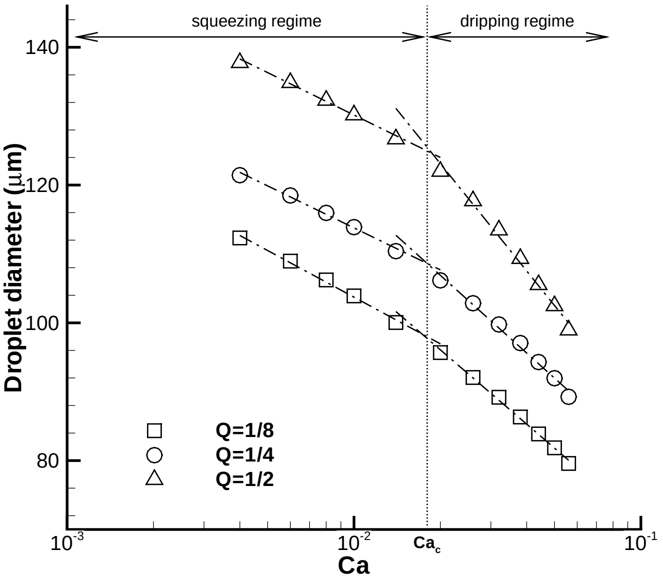

Figure 5.5: The effect of capillary number and flow rate ratio on droplet diameter at a fixed viscosity ratio, $\lambda = 1/8$.

In our simulation, we notice that the two regimes become difficult to distinguish as Q decreases because the droplet detachment point is always close to the downstream corner of the T-junction at small Q. This may explain why Christopher et al. [23] did not observe the critical Ca during the squeezing-to-dripping transition because they performed experiments at small viscosity ratio $\lambda = 0.01$, where the droplet breakup always occurs at the downstream corner of the T-junction.

Many experimental studies were carried out in the squeezing regime so that the droplets filled the main channel and formed “plug-like” or “slug-like” shapes [2, 20, 40], where the viscous shear force may be ignored and the dominant force responsible for droplet breakup is the squeezing pressure caused by the channel obstruction. Garstecki et al. [20] argued that the detachment begins once the emerging droplet fills the main channel and the droplet continues to grow during this time due to continuous injection of the dispersed phase fluid. Assuming that the neck squeezes at a rate proportional to the average velocity of the continuous phase fluid, and the plug fills at a rate proportional to Q_d, a scaling law for the final plug length l was established:

$$l/w_c = 1 + \alpha Q, \tag{5.5}$$

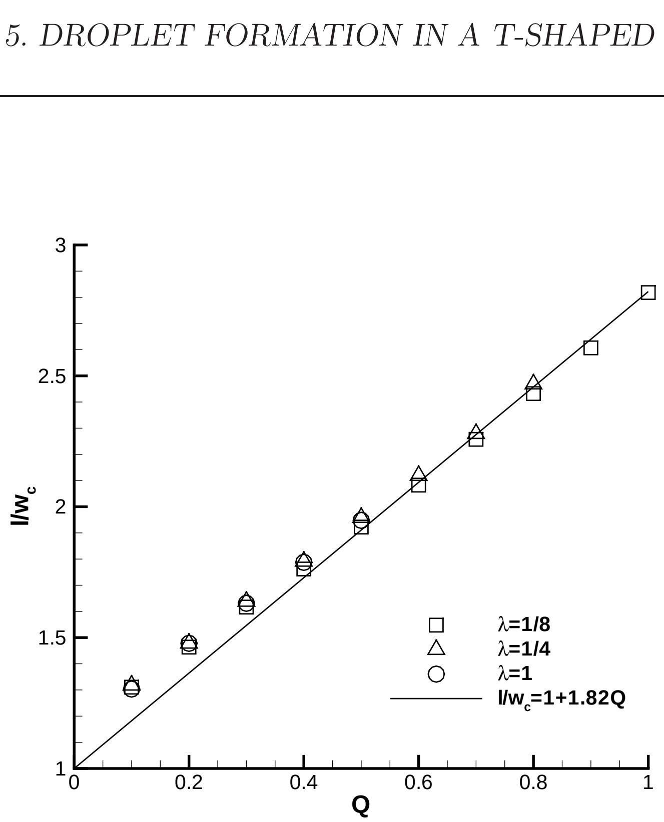

Figure 5.6: For small capillary number ($Ca = 0.005$) in the squeezing regime, our simulation results show that the effect of the flow rate ratio on the droplet size obeys the scaling law proposed by Garstecki et al. [20]

where α is a constant of order one, whose value depends on the widths of both channels. Eq. (5.5) clearly shows the plug length depends only on Q. However, our simulation results shown in Fig. 5.5 suggest that the droplet size also strongly depends on Ca in the squeezing regime, which is consistent with the experimental observations [23]. Therefore, the role of capillary number needs to be reflected in the scaling law.

Although the scaling law, Eq. (5.5) does not capture the capillary number dependency that we observe in simulations, it can predict the droplet size under various flow rate ratios when Ca is fixed in the squeezing regime. Fig. 5.6 shows a scaling formula of $l/w_c = 1 + 1.82Q$ when $Ca = 0.005$. In addition, Eq. (5.5) indicates that the droplet length is independent of the viscosity ratio λ.

5.3 Influence of the viscosity ratio

Here, we investigate the role of the viscosity ratio in the droplet breakup process. In the simulations, the flow rate ratio, Q is fixed at 1/4. Fig. 5.7 shows a series of snapshots of droplet formation with $\lambda = 1/8$ and 1. At the low capillary number

($Ca = 0.006$), as shown in Fig. 5.7(a), the droplet fills the main channel and the detachment occurs at the downstream corner of the T-junction for both viscosity ratios. At the high capillary number (Ca = 0.032, 0.056), the large viscosity ratio will force the position of droplet detachment point to move further to the downstream, which is similar to the effects of Ca and Q as discussed in Section 5.2.

Fig. 5.8 shows that the critical capillary number $Ca_c = 0.018$, which distinguishes the squeezing and dripping regimes, is independent of the viscosity ratio. In the squeezing regime ($Ca \leq \mathrm{Ca}_c$), the predicted droplet diameter is nearly independent of the viscosity ratio, where the droplet formation is completely controlled by the capillary force and the squeezing pressure. In the dripping regime ($Ca > Ca_c$), the influence of viscosity ratio becomes more pronounced as Ca increases, where the large viscosity ratio leads to smaller droplet. However, it also shows that the influence of the viscosity ratio on the generated droplet diameter is not as significant as in the unbounded flow [24], where the breakup of droplets is controlled by a competition between the viscous shear force and the capillary force in the dripping regime. This indicates that the squeezing pressure caused by the confinement of geometry of a T-junction has to be taken into account even in the dripping regime.

5.4 Influence of the contact angle

Due to high surface to volume ratio, fluid/surface interaction will significantly affect the droplet dynamics in microchannels. In order to examine the influence of wetting properties on droplet formation, we simulate the droplet generation at different contact angles i.e. $\theta_w = 110°, 130°, 150°$ and 180°. Fig. 5.9 shows that the contact angle influences droplet shape, generation frequency, the distance between two neighboring droplets, and detachment point. The droplet interfaces tend to be normal to the channel walls at small contact angles, which is consistent with the theory of interface dynamics. In addition, our model can simulate dynamic contact angle. We find that the advancing and receding contact angles are different and both deviate from the prescribed static contact angle θ_w for the dynamic droplet in motion. This phenomenon has been observed in many experiments, and is well known as the contact angle hysteresis [130].

Fig. 5.10 shows that the droplet diameter decreases as the contact angle increases, but the squeezing-to-dripping transition still occurs at the the same criti-

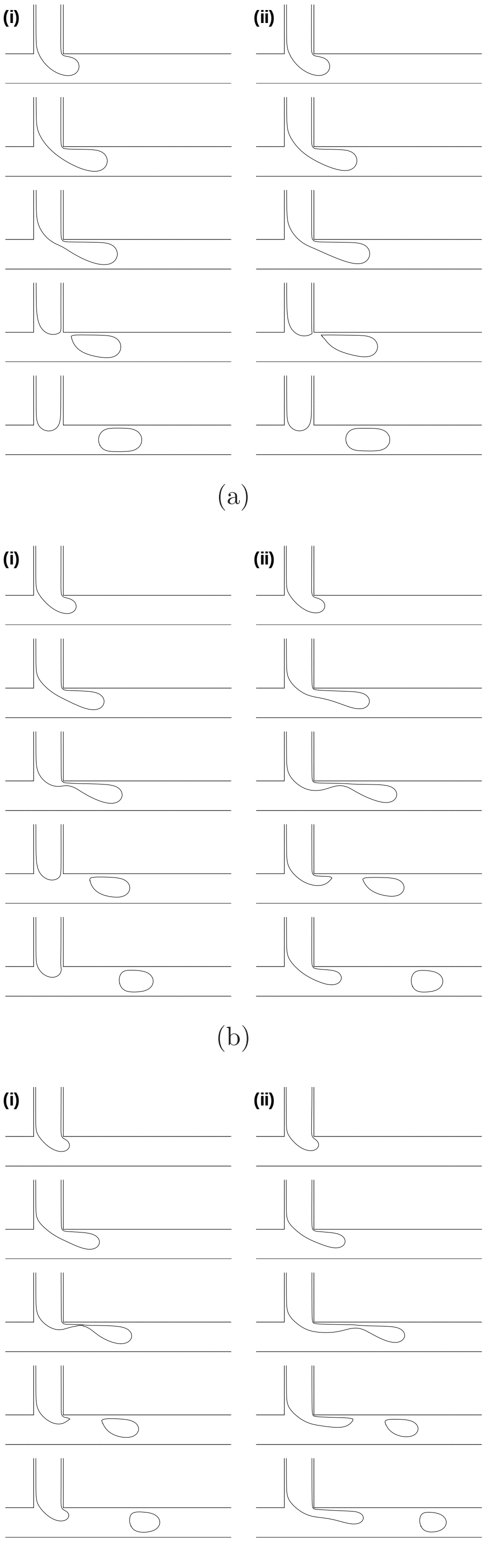

(a)

(b)

(c)

Figure 5.7: The effect of the viscosity ratio in the droplet formation process at a fixed flow rate ratio $Q = 1/4$, where (a) $Ca = 0.006$; (b) $Ca = 0.032$; and (c) $Ca = 0.056$; and the viscosity ratio λ is 1/8 and 1 for the column (i) and (ii).

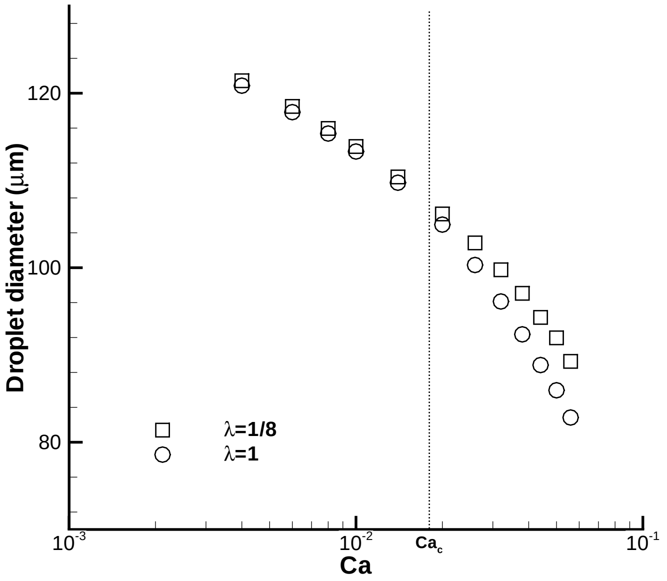

Figure 5.8: The effect of the capillary number and the viscosity ratio on droplet diameter at a fixed flow rate ratio, i.e. $Q = 1/4$.

cal capillary number i.e. $Ca = 0.018$ for different wetting conditions. In addition, the droplet size is independent of the viscosity ratio in the squeezing regime, which was also reported in the literature [20,22], is only valid for more hydrophobic wetting conditions. When θ_w is small (at 110° and 130°), we find that the droplet size depends on the viscosity ratio. For a given contact angle θ_w, larger λ generally produces slightly larger droplets in the squeezing regime but smaller droplets in the dripping regime. Interestingly, we find that the wetting property has more significant effect on droplet size at small Ca, and its effect diminishes gradually when Ca increases. The reason may be that the generated droplet at a small Ca is usually big, which has a large contact area with the channel surface, so that the wall surface plays a more significant role in the droplet generation.

5.5 Conclusions

In this chapter, our improved phase-field lattice Boltzmann model has been applied to study the droplet formation in a microfluidic T-junction. The capillary number, the flow rate ratio, the viscosity ratio and the contact angle have found to be important in droplet formation, and these parameters are coupled together

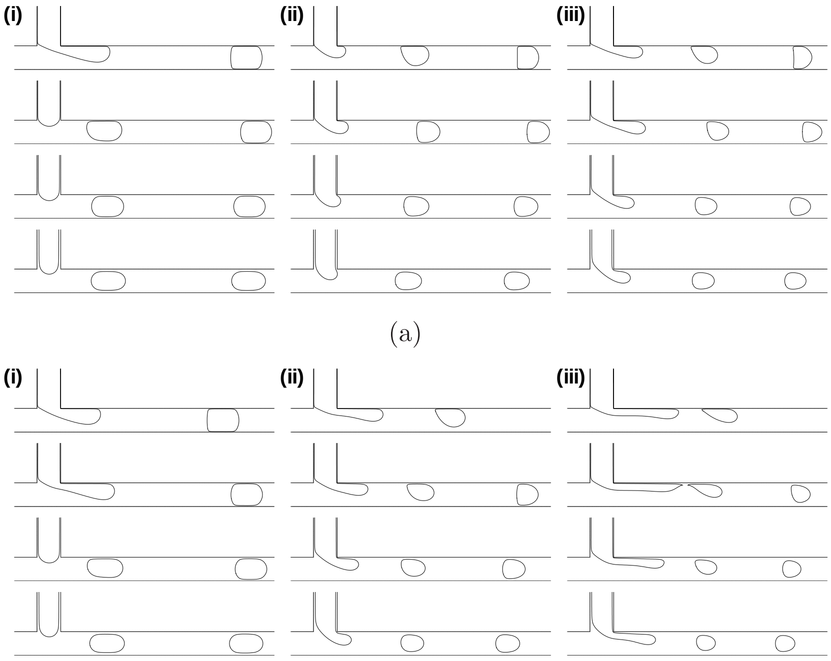

(a)

(b)

Figure 5.9: The flow patterns for different contact angles: θ_w is the same in each row ($110°, 130°, 150°$ and $180°$ from the top row to the bottom row); column (i) $Ca = 0.006$, column (ii) $Ca = 0.032$, column (iii) $Ca = 0.056$; (a) $\lambda = 1/8$ and (b) $\lambda = 1$.

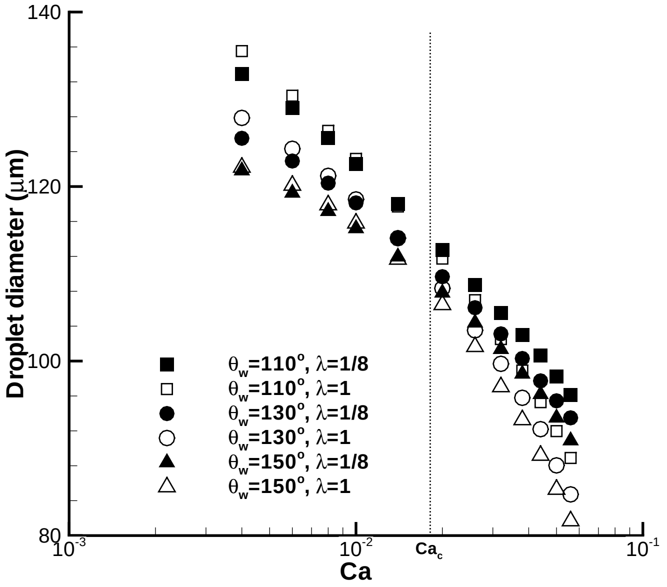

Figure 5.10: The effect of the contact angle, the capillary number and the viscosity ratio on droplet diameter.

to control the complex droplet generation process. We have focused on droplet formation in the squeezing and dripping regimes. The squeezing-to-dripping transition occurs at a critical capillary number $Ca_c = 0.018$, which is independent of the flow rate ratio, the viscosity ratio and the contact angle. Unlike unbounded flow, the squeezing pressure not only dominates the droplet generation in the squeezing regime but also plays an important role in the dripping regime. In the next chapter, we will explore the mechanisms of droplet generation in a microfluidic cross-junction.

Chapter 6

Droplet formation in a microfluidic cross-junction

Although flow physics of droplet generation at T-junctions has been extensively investigated both experimentally and numerically, significant effort is required to understand droplet generation in a confined cross-junction. The droplet dynamics in a microfluidic cross-junction is also very complicated. Many coupled factors will affect the droplet formation process, e.g. interfacial tension, wetting properties and confinement of flow channels, fluid flow rates and viscosities, and their influences may be different from those in T-junction due to the difference in channel geometry. Several experimental studies has been done to investigate the droplet formation in the microfluidic cross-junction. Cubaud et al. [13] investigated the liquid/gas flows in a cross-junction and found that the bubble breakup could be understood as the competition between the pressure drops in the liquid and gas phases. The bubble size could be predicted by the gas/liquid flow rate ratio. Garstecki et al. [14] investigated the mechanism for bubble breakup process in the cross-junction with a small orifice, and observed that the collapsing rate of the neck is quasi-stationary and proportional to the liquid flow rate. Tan et al. [15] studied the formation mechanism of plug flow in a oil/water microfluidic cross-junction. They found that the plug size depends on the flow rate ratio of both fluids and the capillary number. Recently, Fu et al. [16] found that the bubble (slug) breakup process in a cross-junction is mainly controlled by the collapse stage, during which, the collapse rate of the thread neck and the collapse time were affected by the gas/liquid flow rate ratio and the viscosity of the liquid phase.

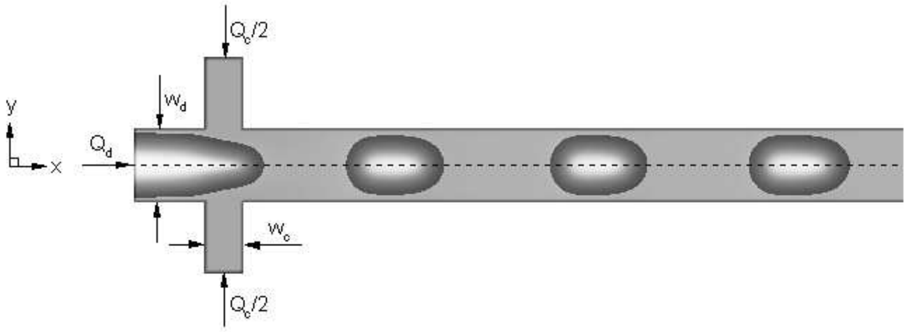

Figure 6.1: The schematic diagram of droplet formation in a cross-junction microchannel, where w_c, w_d are the widths of the main and lateral channels, and Q_c and Q_d are the inlet volumetric flow rates of the continuous and dispersed phases.

In order to gain a comprehensive understanding for better design of microfluidic devices, it is necessary to systematically study the droplet generation in cross-junctions. While many experimental investigations have helped to understand the underlying physics, direct numerical simulations can provide more details on various factors and their interactions, and hopefully deeper insights at a lower cost especially with the fast development of computing power. In this chapter, numerical investigation on the droplet formation in a microfluidic cross-junction is carried out to understand the mechanisms of confined droplet breakup. The influences of the capillary number, the flow rate ratio, the viscosity ratio and the viscosity of the continuous phase on droplet size, shape and detachment are systematically studied. Our simulation results show that the droplet formation in an oil/water two-phase system is noticeably different from the bubble formation in some existing experiments, more consistent with the experimental findings of Tan et al. [15]. Considering the balance between the viscous force and the capillary force, and the influence of oil/water flow rate on the shape of interface, the droplet diameter can be described as a function of the ratio of water/oil flow rates and the capillary number.

6.1 Description of computational system

The schematic diagram of a cross-junction microchannel used in this study is shown in Fig. 6.1. The microchannel consists of the main channel with width w_c = 200 μm and the two lateral channels with the same width i.e. w_d =

100 μm. The dispersed phase water is introduced at the inlet of the main channel, and the continuous phase oil is injected into the lateral channels. We aim to understand the droplet formation mechanism in a microfluidic cross-junction. So we use the mesoscale phase-field model to coarsely resolve the interface and run our simulations in 2D. The computational domain consists of 360 × 30 lattices, where only one half domain is used in the y-direction due to the symmetry of the problem. In all the cases, we find that mesh refinement will lead to result variations no more than 5%.

For simplicity, we assume that the both fluids have the same densities, which are given by ρ. It is expected that this choice has negligible influence on the results, since in typical oil-water microfluidic system buoyancy-driven velocities are much smaller than the actual flow velocities. We also assume the contact angle $\theta_w = 180°$ so that the continuous phase fluid completely wets the walls, and the dispersed phase fluid is non-wetting. For the selected geometrical parameters w_c and w_d, the dynamical response of fluids in a microfluidic cross-junction can be fully described by the experimentally measurable parameters including the interfacial tension σ, the inlet volumetric flow rates (Q_c and Q_d), the fluid viscosities (η_c and η_d) and density ρ, where the subscripts 'c' and 'd' denote the continuous and dispersed phases respectively. Based on these six parameters, the size of droplets formed in this microchannel can be defined by four dimensionless numbers following the Buckingham's Pi theorem, i.e.

$$d = f(Ca, Re, Q, \lambda), \tag{6.1}$$

where d is the droplet diameter, which is defined by the diameter of a spherical droplet with the same volume as a non-spherical droplet; Ca is the capillary number describing relative importance of the viscosity and the interfacial tension, and it is defined by the average inlet velocity u_c and the viscosity η_c of the continuous phase, and the interfacial tension σ as $Ca = \frac{u_c\eta_c}{\sigma} = \frac{Q_c\eta_c}{2\sigma w_c}$; Re is the Reynolds number describing the ratio of inertia to viscous stresses, i.e. $Re = \frac{\rho u_c w_c}{\eta_c} = \frac{\rho Q_c}{2\eta_c}$; $Q = \frac{Q_d}{Q_c}$ is the ratio of flow rates, and $\lambda = \frac{\eta_d}{\eta_c}$ is the viscosity ratio. For the flow regimes under consideration, the Reynolds number is small ($Re < 1$), and it has a negligible effect on the formation of the droplet in microchannel, so that the number of governing parameters reduces to Ca, Q and λ.

Different kinds of droplets, namely slug droplet, isolate droplet and satellite droplet, can be generated in the cross-junction microfluidic device, which strongly depend on the flow conditions [16]. In the present study, we focus on formation of slugs and isolate droplets, and examine the roles of the above dimensionless numbers in droplet formation.

6.2 Results and discussions

6.2.1 The effect of capillary number

Fig. 6.2 shows the influence of capillary number on the droplet diameter where the interfacial tension $\sigma = 0.016$, the viscosity of the continuous phase $\eta_c = 0.08$ and the viscosity ratio $\lambda = 1/4$. The densities of both fluids are assumed to be unity. In order to compare our simulation results with the experimental observations [15], we choose $Q_d = 0.002$, 0.004 and 0.008 in the simulations. For convenience, all quantities are expressed in the lattice units except the droplet diameter, which is in the physical unit. To match these LB simulation parameters to their physical values, we choose three reference quantities: a length scale L_0, a time scale T_0, and a mass scale M_0. In this study, $L_0 = 10^{-5}$ m, $T_0 = 10^{-6}$ s and $M_0 = 10^{-12}$ kg. A simulation parameter with dimensions $[L]^{n1}[T]^{n2}[M]^{n3}$ is multiplied by $[L_0]^{n1}[T_0]^{n2}[M_0]^{n3}$ to obtain the physical value. Following this criterion, for example, we can obtain the physical value of interfacial tension σ^{phy} by: $\sigma^{phy} = \sigma\frac{M_0}{T_0^2} = 0.016\frac{10^{-12}}{(10^{-6})^2} = 0.016$ N m^{-1}, and the physical value of continuous phase viscosity η_c^{phy} by: $\eta_c^{phy} = \eta_c\frac{M_0}{L_0T_0} = 0.08\frac{10^{-12}}{10^{-5}\cdot10^{-6}} = 8\times10^{-3}$ Pa s.

For each Q_d, we control Ca by only varying Q_c. At a fixed dispersed phase flow rate, the droplet diameter becomes smaller when Ca increases. At small Ca , the flow rate of the dispersed phase shows a significant effect on the droplet diameter, and larger Q_d is expected to generate a larger droplet; whereas the influence of Q_d gradually weakens as Ca increases. These observations are consistent with the experimental findings of Tan et al. [15]. Fig. 6.3 shows the snapshots of droplet formation at a fixed $Q_d = 8\times10^{-3}$ for various capillary numbers. At large capillary number, the dispersed phase fluid breaks up easily leading to small droplets. When the capillary number increases, the distance between two neighboring droplets increases.

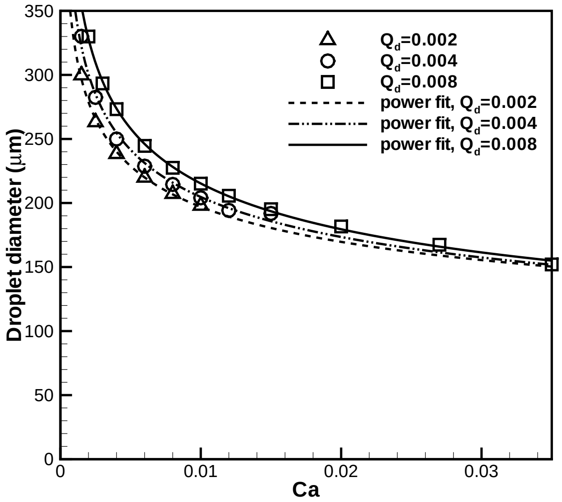

Figure 6.2: The influence of capillary number on the droplet diameter at the dispersed phase flow rate Q_d of 2×10^{-3}, 4×10^{-3} and 8×10^{-3} respectively. The lines represent the power fittings of the simulation results.

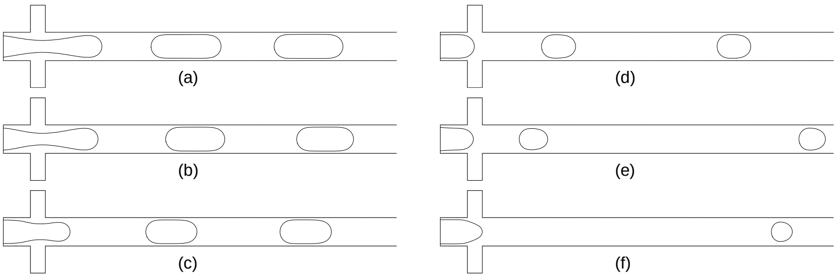

Figure 6.3: The droplet generation at the dispersed phase flow rate $Q_d = 8 \times 10^{-3}$ for various capillary numbers: (a) 0.002; (b) 0.003; (c) 0.004; (d) 0.01; (e) 0.02; and (f) 0.035.

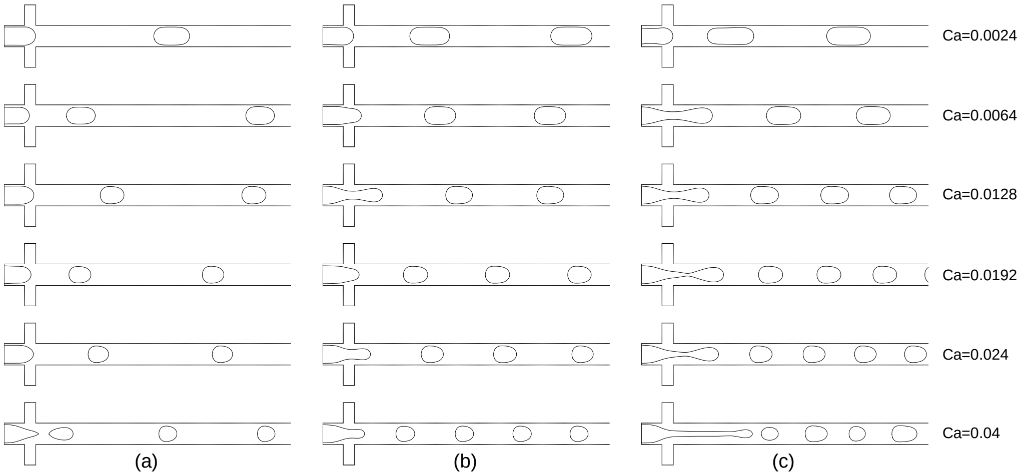

Figure 6.4: The flow patterns for various capillary numbers and the flow rate ratios at a fixed viscosity ratio $\lambda = 1/4$: (a) $Q = 1/6$; (b) $Q = 1/3$; and (c) $Q = 1/2$. Each row uses the same capillary number, which is labelled on the right side.

6.2.2 The effect of flow rate ratio

The effect of flow rate ratio on droplet formation is investigated over a wide range of capillary numbers. We still keep the fluid pair fixed, where the interfacial tension is now set to be 0.01 (the corresponding physical value is 0.01 N m^{-1}), and the densities and viscosities of both fluids are kept the same as in the previous section. Three different flow rate ratios, i.e. $Q = 1/6$, 1/3, and 1/2, are used in the simulations. For each flow rate ratio, the capillary number varies from 0.0024 to 0.04, typically found in microfluidic droplet generation. To keep the flow rate ratio fixed, both Q_c and Q_d must vary as Ca varies.

As shown in Fig. 6.4, the monodisperse droplets are regularly generated for all capillary numbers at low flow rate ratios, i.e. $Q = 1/6,\ 1/3$. For the high flow rate ratio $Q = 1/2$, the highly uniform droplets can be generated at small capillary number i.e. $Ca \leq 0.024$. For high capillary number $Ca = 0.04$, the generated droplets are not uniform, where a long dispersed jet is observed with the detachment point moving progressively downstream. In the future, we will investigate this jetting mode in detail. For all of the cases with uniform droplets generated, the distance between two neighboring droplets and their size decrease when Ca increases at the same flow rate ratio Q. Increasing the flow rate ratio can decrease the distance between two neighboring droplets at the same Ca .

Fig. 6.5 shows the predicted droplet diameter as a function of capillary num-

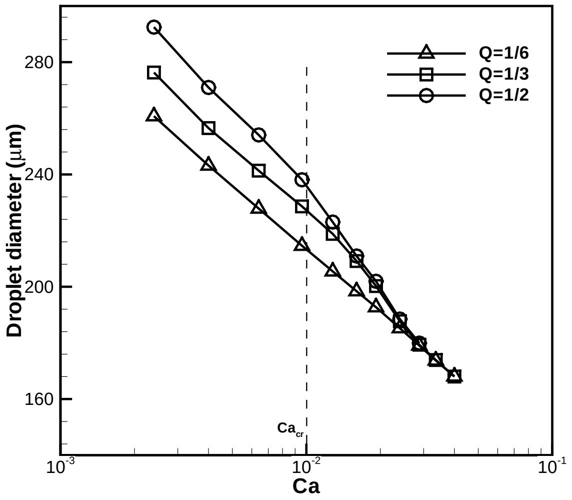

Figure 6.5: The effect of capillary number and flow rate ratio on droplet diameter at a fixed viscosity ratio, $\lambda = 1/4$. Note that, for $Q = 1/2$ and $Ca > 0.024$, the measured droplet diameters are not plotted in this figure due to irregular droplets are generated.

ber for three different flow rate ratios. The droplets grow as the flow rate ratio increases but they become smaller as the capillary number increases. This trend is consistent with the experimental observations for the droplet production in a variety of geometries [3]. Two distinguished regimes are identified and divided by a critical capillary number (Ca_{cr}), which is 0.01 in our simulations. For low Ca, i.e. $Ca \leq Ca_{cr}$, the flow rate can significantly affect the droplet size, and the droplet diameter d exhibits a power-law dependence on the capillary number, i.e. $d \propto Ca^{-0.147}$, where the power-law exponent $\alpha = -0.147$ is independent of the flow rate Q. This finding was also experimentally observed by Tan et al. [15] for the plug generation in a cross-junction microchannel. Obviously, the formation of plugs in a cross-junction is different from the experimental observation of Garstecki et al. [20] in microfluidic T-junctions where the plug size depends predominantly on the flow rate ratio Q rather than the capillary number Ca. Garstecki et al. [20] concluded that the droplet breakup is completely dominated by the squeezing pressure, which arises when the emerging droplet obstructs the continuous phase stream in the main channel. However, the numerical investigation in Chapter 5 and a recent numerical study [131] on the plugs formed in T-junctions observed that the droplet size is also dependent on Ca at low cap-

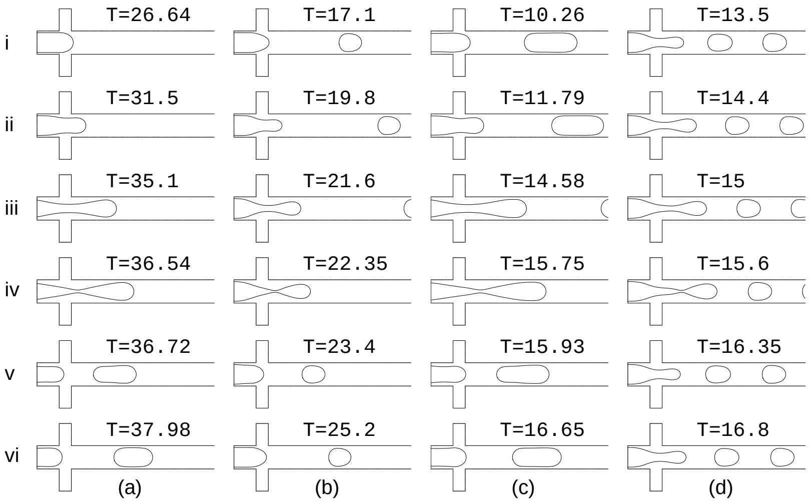

Figure 6.6: A series of instantaneous states of droplet formation for (a) $Q = 1/6,\ Ca = 0.0024$; (b) $Q = 1/6,\ Ca = 0.024$; (c) $Q = 1/2,\ Ca = 0.0024$ and (d) $Q = 1/2,\ Ca = 0.024$. The viscosity ratio $\lambda = 1/4$, and the dimensionless time is defined as $T = \frac{u_c}{w_c}t$.

illary numbers. In addition, the 3D cross-junction simulation of Wu et al. [132] showed that, at a fixed flow rate ratio, the droplet size has no sign of approaching a constant value as the capillary number decreases, although they did not report the power-law dependence of droplet size on the capillary number. In the next section, we will also show that the viscous force plays an important role in the process of droplet generation in this regime, which we call the squeezing-like regime in this chapter. When $Ca > Ca_{cr}$, the dependence of the droplet diameter on the capillary number does not exhibit a fixed power-law behavior, and the effect of flow ratio diminishes quickly as Ca increases. More specifically, the droplet diameter is completely independent of the flow rate ratio when $Ca \geq 0.024$. This feature, in the dripping regime, is similar to the T-junctions [22, 133]. In the dripping regime, the viscous force is significant, together with the capillary force, determine the process of droplet breakup, which is significantly different from the droplet generation in unbound flow conditions due to the confinement of channel walls [22].

Fig. 6.6 shows a series of instantaneous states of droplet formation with four pairs of Q and Ca: (a) $Q = 1/6,\ Ca = 0.0024$; (b) $Q = 1/6,\ Ca = 0.024$; (c) $Q = 1/2,\ Ca = 0.0024$ and (d) $Q = 1/2,\ Ca = 0.024$. It can be seen that the droplet formation process has three stages, i.e. expansion (i)-(iii), necking (iv) and figuration (v)-(vi). At small capillary number i.e. $Ca = 0.0024$, the incoming dispersed phase fluid tends to occupy the full width of the outlet channel and the dispersed phase interface has a large deviation from the solid wall at the main channel entrance, so the squeezing pressure is pronounced when the emerging droplet obstructs the channel. While in the dripping regime i.e. $Ca = 0.024$, the dispersed phase fluid occupies only part of the outlet channel, and smaller droplets are formed. At small Q, i.e. $Q = 1/6$, the droplets are pinched off close to the junction corner for all the capillary numbers. Increasing Q will move the detachment point further to the downstream. At small Q (see Fig. 6.5), the two regimes i.e. the squeezing-like and dripping regimes are not distinguishable, which was also observed experimentally in droplet generation in a T-junction by Christopher et al. [23]. Fig. 6.6 also gives the dimensionless times corresponding to various instantaneous states of droplet formation process. The dimensionless time is taken as $T = \frac{u_c}{w_c}t = \frac{Q_c}{2w_c^2}t$. It can be clearly seen that the increase in Q (or Ca) can lead to the decrease in elapsed dimensionless time for generating each droplet.

6.2.3 The effect of viscosity ratio

The viscosity ratio is known to affect breakup of isolated droplets [134] and liquid jets [135]. Moreover, the numerical and experimental investigations on T-junction microchannel reveal that the effect of viscosity ratio is most pronounced in the dripping regime and diminishes in the squeezing regime [20,22,54,133]. However, in a cross-junction with oil-water two-phase flow, Tan et al. [15] found that the plug size is independent of viscosity ratio and decreases when the continuous phase viscosity increases. Christopher et al. [23] experimentally observed in the T-junction microfluidic devices that the viscosity ratio influences the droplet size only when the viscosities of two fluids are similar. When the viscosity ratio $\lambda < 1/50$, the resulting droplet size is independent of the viscosity ratio. In addition, Fu et al. [16] found that the viscosity of liquid phase is one of the dominant parameters during the bubble breakup process. To understand the complex effect of viscosity ratio and viscosity on droplet breakup, we numerically simulated the droplet breakup process in a cross-junction. In the simulations, the interfacial tension is set to be 0.01 (the corresponding physical value is 0.01 N m^{-1}). The flow rate of the continuous phase Q_c varies from 0.006 to 0.06, and the flow rate ratio Q is fixed at 1/6 so that the droplet breakup always occurs close to the junction as the experiment of Tan et al. [15].

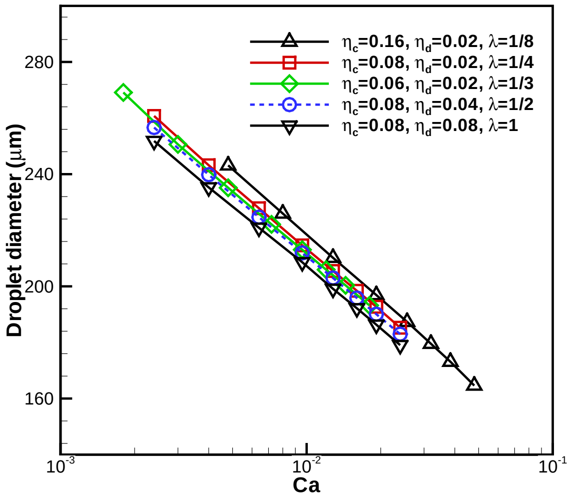

Figure 6.7: The effect of capillary number and viscosity ratio on droplet diameter at a fixed flow rate ratio, i.e. $Q = 1/6$.

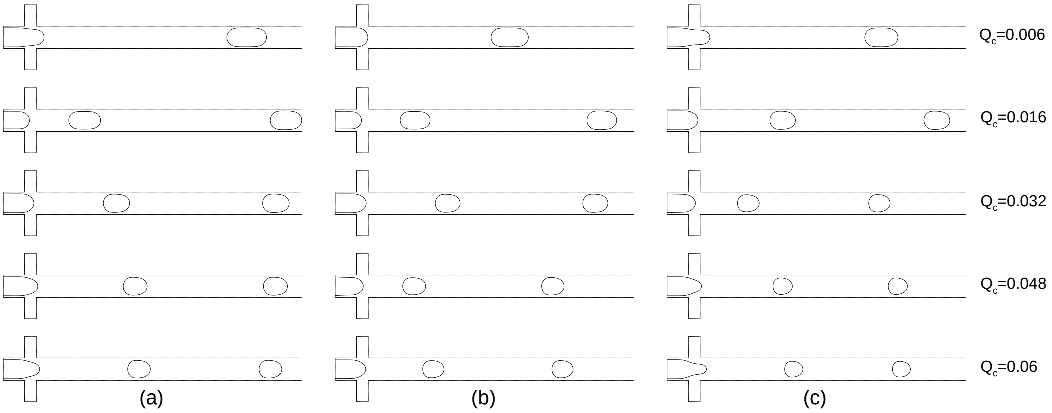

Figure 6.8: The flow patterns for various η_c and Q_c at a fixed flow rate ratio $Q = 1/6$: (a) $\eta_c = 0.06$; (b) $\eta_c = 0.08$; and (c) $\eta_c = 0.16$. Each row uses the same Q_c, which is labelled on the right side.

Fig. 6.7 shows that the droplet size is found to be weakly dependent on the viscosity ratio, which is very similar to the experimental observation by Christopher et al. [23] in a T-junction where the viscosity ratio is smaller than 1/50. Fig. 6.8 shows the flow patterns for different viscosities of the continuous phase. The droplet size and the distance between two neighboring droplets decrease as the viscosity of the continuous phase increases at a fixed Q_c (or Q_d). The result is consistent with the experimental finding in the cross-junction by Tan et al. [15]. However, it is different from the experimental observations on droplet formation in the T-junction microchannel [20, 54] and bubble formation in a cross-junction microchannel [13, 14], where the plug length is independent of the viscosity of the continuous phase. Tan et al. [15] argued that the difference may attribute to the symmetrical flow route of cross-junction and small capillary number in bubble formation. In addition, the sharp corner of T-junctions and the large density and viscosity ratios in the bubble formation may also be responsible.

There are two mechanisms which influence plug/droplet size. One is the dynamic breakup of interface, which can mainly be affected by the flow rate ratio Q. The other is the balance between the viscous force and the capillary force, which can be described by the capillary number. Tan et al. [15] proposed a scaling law to predict the plug length, which will be similarly used to estimate droplet sizes apart from the flow conditions in the dripping regime with large Q where the droplet breakup occurs at further downstream of the junction. Therefore, the droplet diameter d can be correlated as

$$d = kQ^{\alpha}Ca^{\beta}, \tag{6.2}$$

where α and β represent the influences of two mechanisms. Our numerical simulations suggest that this scaling law works well with the coefficients of $k = 129.32$, $\alpha = 0.103$ and $\beta = -0.147$ (see Fig. 6.9). Although the scaling law may not be quantitatively accurate as 3D effects are not considered, our 2D simulation results can reveal the underlying mechanisms of droplet breakup which are consistent with the experimental findings [15].

6.3 Conclusions

Water droplet formation in a microfluidic cross-junction has been simulated using the phase-field lattice Boltzmann model. The influence of capillary number, flow

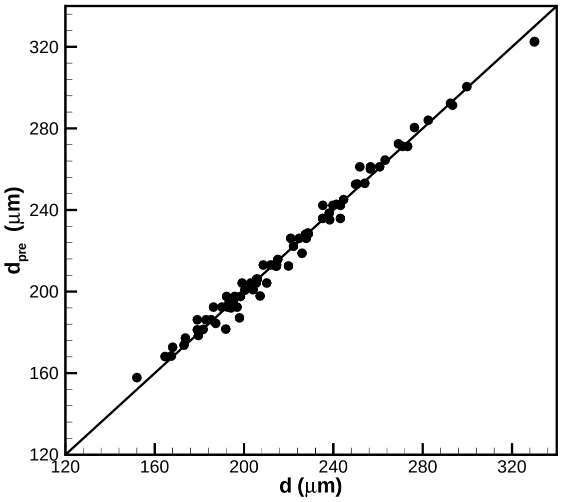

Figure 6.9: Comparison of droplet diameter between the fitting results d_{pre} from Eq. (6.2) and the simulation results d.

rate ratio, viscosity ratio, and viscosity of continuous phase on droplet formation has been systematically studied over a wide range of capillary numbers. Two different regimes, i.e. the squeezing-like and dripping regimes, are clearly identified with the transition occurring at a critical capillary number $Ca_{cr} = 0.01$. However, these two regimes are difficult to distinguish when the flow rate ratio decreases. In the squeezing-like regime, i.e. $Ca \leq Ca_{cr}$, the droplet breakup is influenced not only by the squeezing pressure but also by the viscous force. While in the dripping regime, i.e. $Ca > Ca_{cr}$, the viscous force plays an increasingly important role in the breakup process and the droplet size becomes quickly independent of the flow rate ratio for large capillary number. As the droplet size is weakly dependent on the viscosity ratio, a scaling law is constructed to estimate the generated droplet size, which depends on the capillary number and the flow rate ratio.

Chapter 7

Phase-field modeling droplet dynamics with soluble surfactants

7.1 Introduction

Surfactants are interfacially active agents that play an important role in many industrial processes, ranging from crude oil recovery, manufacture of cosmetics and pharmaceutical products, to food processing [136]. More recently, surfactants have been widely used in microfluidic applications [29]. Commonly-used surfactants are the molecules with polar head groups appended to hydrophobic tails, which selectively adhere to fluid interfaces forming a buffer zone to reduce the system energy. In microfluidic systems, surfactants are often used to generate small droplets and make them kinetically stable as emulsions even though water-in-oil and oil-in-water emulsions are thermodynamically unstable [137]. The capillary effect usually plays a dominant role in a microfluidic system, and the presence of surfactants at an interface will greatly modify interfacial tension. Therefore, surfactants are expected to significantly alter droplet dynamical behavior in the microfluidic devices [48,92,138]. A number of recent theoretical or numerical studies have reported to identify the mechanisms of droplet deformation, breakup and coalescence in the presence of surfactants [30, 32, 80, 139–143].

Modelling interfacial dynamics with soluble surfactants in a multiphase system is a daunting task. The surfactant molecules will self-assemble into a monolayer at the oil/water interface, thereby lowering interfacial tension. When the bulk concentrations are below the critical micelle concentration (CMC) and the surfactant lateral interactions are not important, the Langmuir adsorption can describe the realistic equilibrium adsorption behavior of non-ionic surfactants [144]. When the surfactant lateral interactions cannot be neglected, the Frumkin adsorption is more appropriate. Both advection and diffusion are important for surfactant transport at the interface and in the bulk phases. Non-uniform surfactant concentration (mainly at the interface) creates non-uniform interfacial tension forces and Marangoni stresses in the fluid, which in turn affect the flowfield. Meanwhile, the flowfield will influence the surfactant distribution. The interaction between surfactants and flowfield is highly non-linear, which poses a computational challenge. Most previous numerical work [32, 74, 80, 145–149] on surfactants has utilized the sharp interface models with an equilibrium equation of state relating dynamic interfacial tension to local surfactant concentration. The sharp interface models are built upon the conservation laws at the macroscopic level for interfacial dynamics, which have been developed from the original model proposed by Stone and Leal [32]. The models have been successfully applied to simulate interfacial flows in an oil/water/surfactant system. However, these sharp interface models suffer from several drawbacks: (i) dynamic interfacial tension relies on an asserted equilibrium equation of state, which is also assumed to be valid beyond the equilibrium state; (ii) for interfacial flows with soluble surfactants, mass transfer between the interface and the bulk fluids requires an external boundary condition, which cannot uniquely arise from the model itself; (iii) model extension for more complicated systems, such as ionic surfactant solutions, is not easy [33]; (iv) numerical stability becomes a problem for the flows with large topological changes, such as droplet breakup and coalescence.

In contrast to the sharp interface model, the phase-field method, which can resolve the interface structure via an appropriate free energy functional, has shown great potential to simulate the multiphase flow problems [21, 121, 133, 150–153]. In a phase-field model, the free energy not only determines the equilibrium properties, but also strongly influences the dynamics of the multiphase system. The transport of physical quantities can be linked to the free energy by a generalized hydrodynamic theory [154]. Hence, the phase-field models have a firm physical basis for multiphase flows, which is contrast to the traditional computational fluid dynamics (CFD) methods, e.g. the volume-of-fluid, level-set and front-tracking methods. Although phase-field models have shown promise for computation of binary mixture with surfactants [90, 155, 156], significant effort is still required to improve the model for realistic oil/water/surfactant systems. In this chapter, a generalized phase-field model, which is numerically solved in a lattice Boltzmann

(LB) framework, is presented to simulate the adsorption of surfactants at the interface and its effect on droplet dynamics.

7.2 Phase-field model for immiscible fluids containing surfactants

The ternary system we consider consists of a non-ionic surfactant solute and two immiscible solvents, say, oil and water. We aim to develop an improved phase-field model that is able to capture both thermodynamic and hydrodynamic effects associated with surfactants in realistic ternary systems.

7.2.1 Free energy theory

The thermodynamics of a system is determined by its free energy functional. The Landau-Ginzburg free energy functional has been commonly used to describe a binary mixture, which has been given in Chapter 3, i.e.

$$\mathscr{F} = \int \mathrm{d}\vec{x} \left[-\frac{A}{2}\phi^2 + \frac{B}{4}\phi^4 + \frac{\kappa}{2}(\nabla\phi)^2 \right], \tag{7.1}$$

where $\phi = (\rho_w - \rho_o)/\rho$ represents the relative concentration of the local compositions. As we aim to deal with two immiscible fluids, and oil and water are most commonly used in microfluidic applications, we use oil and water to represent two immiscible fluids here. $\rho = \rho_o + \rho_w$ is the total density, while ρ_o and ρ_w are the densities of oil and water phases respectively. The first two terms in Eq.(7.1) correspond to the bulk phase behaviour, with minima $\phi = \pm\phi_b = \pm\sqrt{A/B}$ for the oil and water respectively. The last term reflects the cost of sustaining the oil/water interface. Hereafter, the subscripts ‘b’ and ‘0’ denote the bulk phases and interface, and the superscripts ‘+’ and ‘-’ represent the oil and water bulk phases, respectively.

As surfactants favor adherence to the oil/water interface and lower the interfacial tension, and the interfacial tension lowering scale depends on the local surfactant concentration. To account for the surfactant effect, additional terms are introduced to the original Landau-Ginzburg free energy functional. Laradji et al. [157] proposed the free energy functional in the form of

$$\mathscr{F} = \int \mathrm{d}\vec{x} \left[-\frac{A}{2}\phi^2 + \frac{B}{4}\phi^4 + \frac{\kappa}{2}(\nabla\phi)^2 + \frac{C}{2}\psi^2 + \frac{W}{2}\psi^2\phi^2 - \frac{D}{2}\psi(\nabla\phi)^2 \right], \quad (7.2)$$

where ψ is the surfactant local concentration in an oil/water/surfactant system. The term $\frac{C}{2}\psi^2$ prevents the surfactants from forming clusters. The local coupling term $\frac{W}{2}\psi^2\phi^2$ guarantees small local surfactant concentration in the bulk phases, which is introduced to numerically stabilise the diffuse interface model for microemulsions. The last nonlocal coupling term $-\frac{D}{2}\psi(\nabla\phi)^2$ accounts for the energetic preference of surfactants when they are absorbed at the oil/water interface, favoring the lowering of interfacial tension.

Theissen and Gompper [155] chose a slightly different form of free energy functional to study the dynamics of spontaneous emulsification, where the local coupling term is replaced by $\frac{W}{2}\psi\phi^2$ to deal with the same solubility of surfactant in the bulk phases. Recently, Furtado et al. [156] applied a simpler form of free energy functional to phenomenologically describe the surfactant effect. In contrast to Eq. (7.2), the local coupling term vanishes and κ is expressed as a function of ψ to relate the interfacial tension to the surfactant concentration. We have derived the equilibrium equation of state following the free energy functional presented by Theissen and Gompper [155] (the details are shown in Appendix B), i.e.

$$\sigma(\psi_0) = \frac{4\phi_b^2}{3\xi}(\kappa - D\psi_0), \quad (7.3)$$

where ξ is a parameter proportional to the interface thickness, which is given by

$$\xi^2 = \frac{2(\kappa - D\psi_0)}{\phi_b^2(B - \frac{W^2}{2C})} = \frac{2[\kappa - D(\psi_b + \frac{\phi_b^2 W}{2C})]}{\phi_b^2(B - \frac{W^2}{2C})}. \quad (7.4)$$

We note that the condition $Ex = \frac{D}{W\xi^2} \ll 1$ should be satisfied to analytically obtain Eqs. (7.3) and (7.4). Obviously, the free energy model proposed by Theissen and Gompper [155] cannot exhibit realistic adsorption isotherms such as the Langmuir/Frumkin adsorption isotherms. Similarly, we can show that the models proposed by Laradji et al. [157] and Furtado et al. [156] fail to recover the Langmuir/Frumkin adsorption isotherms. As both Langmuir/Frumkin adsorption isotherms are well developed for adsorption of non-ionic surfactants under the equilibrium state with the bulk surfactant concentrations below the CMC. It is important for any realistic model to recover these adsorption isotherms under the thermodynamical equilibrium state.

Diamant and Andelman [33] developed a sharp interface free energy model to describe the surfactant adsorption at the interface between an aqueous solution and another fluid phase. They introduced the ideal entropy of mixing into the model and treated the bulk solution and the interface as two coupled subsystems. The model can lead to the Frumkin adsorption isotherm in thermodynamic equilibrium. However, hydrodynamics was not considered in their model, so it cannot be applied to simulate droplet dynamic behavior with soluble surfactants.

Recently, van der Sman and van der Graaf [90] developed a diffuse interface model for surfactant adsorption onto the interface of two immiscible fluids. The free energy functional is partly adapted from the sharp interface model of Diamant and Andelman [33]. The model couples the surfactant adsorption to hydrodynamics, which demonstrates promising potential for phase-field model to simulate droplet dynamics in the presence of surfactants. However, the model is restricted to the Langmuir adsorption with equal solubility of the surfactants in both bulk phases. Although the model showed that the interfacial tension lowering $\Delta\sigma$ is proportional to $k_BT\ln(1-\psi_0)$ due to surfactant adsorption onto the interface, the dependence of the proportionality factor on the parameters used in the model is still unclear. Finally, the model capability is required to be further examined and demonstrated by simulating droplet dynamics with large topology changes.

To describe a ternary system including a non-ionic surfactant solute, we propose to extend the free energy functional given by van der Sman and van der Graaf [90] to incorporate additional functionalities, e.g. the Frumkin adsorption isotherm, and different solubility of the surfactants. Therefore, our free energy functional becomes:

$$\begin{aligned}\mathscr{F} = & \int \mathrm{d}\vec{x} \left\{ -\frac{A}{2}\phi^2 + \frac{B}{4}\phi^4 + \frac{\kappa}{2}(\nabla\phi)^2 + \frac{W}{2}\psi\phi^2 - \frac{D}{2}\psi(\nabla\phi)^2 \right. \\ & \left. + k_BT\left[\psi\ln\psi + (1-\psi)\ln(1-\psi)\right] - \frac{C}{2}\psi^2 - E\phi\psi + \rho T\ln\rho \right\}, \quad (7.5)\end{aligned}$$

where the term involving the Boltzmann constant k_B is the ideal entropy of mixing of surfactant and solvent (i.e. steric effects), and solute and solvent molecules are assumed to have the same size [158]. The term $-\frac{C}{2}\psi^2$ is the energy of lateral interaction between two adjacent surfactants, where $C > 0$ is assumed to express an overall attractive interaction [33]. Note that this term plays a different role here as it appears in Eq. (7.2). The value of C cannot be 0 in Eq. (7.2), whereas in Eq. (7.5) C can be 0 when the lateral interaction is absent. The asymmetric term proportional to E accounts for different solubility of surfactants in the oil and water phases. The final term does not affect the phase behavior, but it is required to enforce incompressibility of the fluid in the lattice Boltzmann model [111]. A suitable choice, based on improving numerical stability and accuracy, is temperature $T = 1/3$.

The chemical potentials μ_ϕ and μ_ψ can then be obtained via the variational derivatives of the free energy functional Eq. (7.5) with respect to ϕ and ψ:

$$\mu_\phi = \frac{\delta \mathscr{F}}{\delta \phi} = B\phi^3 - A\phi - (\kappa - D\psi)\nabla^2\phi + D\nabla\phi \cdot \nabla\psi + W\phi\psi - E\psi, \tag{7.6}$$

$$\mu_\psi = \frac{\delta \mathscr{F}}{\delta \psi} = k_B T[\ln\psi - \ln(1-\psi)] - C\psi + \frac{W}{2}\phi^2 - \frac{D}{2}(\nabla\phi)^2 - E\phi. \tag{7.7}$$

Excess chemical potential gradients give rise to a thermodynamic force (per unit volume) that can be expressed as the divergence of pressure tensor from the Gibbs-Duhem equality:

$$\vec{f_V} = -\nabla \cdot \mathbf{P} = -\phi\nabla\mu_\phi - \psi\nabla\mu_\psi, \tag{7.8}$$

with the pressure tensor $\mathbf{P}$ given by

$$\mathbf{P} = p_0\mathbf{I} + (\kappa - D\psi)(\nabla\phi)(\nabla\phi)^{\mathrm{T}}, \tag{7.9}$$

where $\mathbf{I}$ is the second-order unit tensor, p_0 is the scalar part of the pressure tensor which can be calculated by the thermodynamic relation as [155]

$$p_0 = \rho\frac{\delta \mathscr{F}}{\delta \rho} + \phi\mu_\phi + \psi\mu_\psi - f(\rho, \phi, \nabla\phi, \psi). \tag{7.10}$$

Here, $f(\rho, \phi, \nabla\phi, \psi)$ is the free energy density, i.e. the integrand in Eq. (7.5). Using Eqs. (7.5) and (7.10), we can get

$$\begin{aligned} p_0 \;=\; & \rho T - \frac{A}{2}\phi^2 + \frac{3B}{4}\phi^4 - \frac{\kappa}{2}(\nabla\phi)^2 - k_B T\ln(1-\psi) - \frac{C}{2}\psi^2 \\ & -(\kappa - D\psi)\phi\nabla^2\phi + D\phi\nabla\phi\cdot\nabla\psi + W\psi\phi^2 - E\phi\psi. \end{aligned} \tag{7.11}$$

7.2.2 Hydrodynamics

A dynamic multiphase system needs to be described by not only thermodynamics but also hydrodynamics. Local conservation of fluid mass and momentum leads to the Navier-Stokes equations for Newtonian fluids:

$$\begin{aligned} \partial_t \rho + \nabla \cdot (\rho \vec{u}) &= 0, & (7.12)\\ \partial_t (\rho \vec{u}) + \nabla \cdot (\rho \vec{u}\vec{u}) &= \nabla \cdot \left[\rho\nu(\nabla \vec{u} + (\nabla \vec{u})^{\mathrm{T}})\right] + \vec{f}_V, & (7.13) \end{aligned}$$

which describe the time evolution of the hydrodynamic variables, i.e. the fluid density ρ and the fluid velocity $\vec{u}$. Here, $\nu = \eta/\rho$ is the kinematic viscosity and $\vec{f}_V$ is the thermodynamic force given by Eq. (7.8). In principle, this model can introduce a composition-dependent viscosity [21, 133].

The evolution of the solvent composition ϕ and the local concentration of surfactant solute ψ are described by the Cahn-Hilliard equations, where the diffusion of ϕ and ψ is driven by gradients of chemical potentials μ_ϕ and μ_ψ:

$$\begin{aligned} \partial_t \phi + \nabla \cdot (\phi \vec{u}) &= \nabla \cdot (M_\phi \nabla \mu_\phi), & (7.14)\\ \partial_t \psi + \nabla \cdot (\psi \vec{u}) &= \nabla \cdot (M_\psi \nabla \mu_\psi), & (7.15) \end{aligned}$$

where M_ϕ and M_ψ are the respective mobilities of the two order parameters, which are taken to be constants. Following Eq. (7.15), the surfactant flux $\vec{j}_\psi$ can be written as

$$\vec{j}_\psi = -M_\psi \nabla \mu_\psi. \tag{7.16}$$

To obtain the surfactant diffusion coefficient D_ψ, we can rewrite Eq. (7.16) into

$$\vec{j}_\psi = -M_\psi \frac{\partial \mu_\psi}{\partial \psi} \nabla \psi = -M_\psi \left[\frac{k_B T}{\psi(1-\psi)} - C\right] \nabla \psi, \tag{7.17}$$

with $D_\psi = M_\psi \left[\frac{k_B T}{\psi_b(1-\psi_b)} - C\right]$ in the bulk phases. Here, ψ_b is the surfactant concentration in the bulk phase. Once D_ψ is defined, Eq. (7.15) can recover the usual convection-diffusion equation

$$\partial_t \psi + \nabla \cdot (\psi \vec{u}) = \nabla \cdot (D_\psi \nabla \psi), \tag{7.18}$$

which has been widely used for bulk surfactant transport in the sharp interface model [143, 149, 159].

Similarly, the diffusivity of the interface can be defined as

$$D_\phi = M_\phi A(3\phi^2 - 1 + W\psi) \approx -M_\phi A, \tag{7.19}$$

with $\phi \approx 0$ and $W\psi \ll 1$ near the interface, as the relevant diffusion only takes place at the phase interface. Note that this "negative diffusion" maintains the solvent composition jump across the interface.

7.2.3 Thermodynamic equilibrium

In equilibrium, the thermodynamic force $\vec{f}_V$ becomes zero, and thereby the chemical potentials are equal throughout the entire system. We analyze whether the model can predict the equilibrium properties of the surfactant adsorption in oil/water solvents as described by the Langmuir and Frumkin isotherms. In a dilute solution, the bulk surfactant concentration is much smaller than unity, i.e. $\psi_b \ll 1$. We assume that the solvent composition profile is independent of the surfactant loading in equilibrium, which can be represented as

$$\phi(x) = \phi_b \tanh\left(\frac{x}{\xi}\right), \tag{7.20}$$

where ξ is a measure of the interface thickness as described by Eq. (B.14).

From Eq. (7.7), we can obtain the chemical potentials $\mu^+_{\psi,b}$ and $\mu^-_{\psi,b}$ in the oil and water bulk phases respectively:

$$\begin{aligned} \mu^+_{\psi,b} &\approx k_BT\ln\psi^+_b + \frac{1}{2}W\phi_b^2 - E\phi_b, &(7.21)\\ \mu^-_{\psi,b} &\approx k_BT\ln\psi^-_b + \frac{1}{2}W\phi_b^2 + E\phi_b, &(7.22)\end{aligned}$$

where the magnitude of C is up to $\mathcal{O}(k_BT)$ [33]. The chemical potential at the interface is:

$$\mu_{\psi,0} = k_BT[\ln\psi_0 - \ln(1-\psi_0)] - C\psi_0 - \frac{D}{2\xi^2}\phi_b^2, \tag{7.23}$$

where we have used $\partial_x\phi = \phi_b/\xi$ at the interface $x = 0$ following Eq. (7.20).

In equilibrium, we have $\mu^+_{\psi,b} = \mu^-_{\psi,b} = \mu_{\psi,0}$. So from Eqs. (7.21), (7.22) and (7.23) for the chemical potentials, we can obtain the surfactant concentration ratio β in the oil and water bulk phases

$$\beta = \frac{\psi_b^+}{\psi_b^-} = \mathrm{e}^{\frac{2E\phi_b}{k_BT}}, \tag{7.24}$$

and the equilibrium adsorption isotherm

$$\psi_0 = \frac{\psi_b^\pm}{\psi_b^\pm + \psi_c^\pm \mathrm{e}^{-\frac{C}{k_BT}\psi_0}}, \tag{7.25}$$

with

$$\psi_c^\pm = \exp\left\{-\frac{1}{2k_BT}\left(\frac{D}{\xi^2} + W\right)\phi_b^2 \pm \frac{E}{k_BT}\phi_b\right\}. \tag{7.26}$$

Therefore, our model can recover the Frumkin adsorption isotherm (see Eq. (7.25)), which reduces to the well-known Langmuir adsorption isotherm if $C = 0$. Also, it can be clearly seen from Eq. (7.24) that we can use the parameter E to control the solubility of surfactant in oil-rich phase and water-rich phase. For the sake of simplicity, we assume the same solubility of surfactant in both phases, i.e. $E = 0$, in the following analysis.

In Appendix B, the equilibrium solvent composition profile is analytically demonstrated to be independent of the surfactant loading when the suitable constraints are satisfied. With the solvent composition profile ϕ given by Eq. (7.20), we can obtain an analytical expression for the surfactant concentration at an arbitrary position x from Eq. (7.7)

$$\psi(x) = \frac{1}{1 + \mathrm{e}^{-\frac{1}{k_BT}\left[\mu_\psi - \frac{W}{2}\phi^2 + \frac{D}{2}(\partial_x\phi)^2\right]}\mathrm{e}^{-\frac{C}{k_BT}\psi}}, \tag{7.27}$$

where μ_ψ is determined by Eq. (7.21) or Eq. (7.22).

In the sharp interface models, the equilibrium equation of state can be derived via integration of the Gibbs equation:

$$\mathrm{d}\sigma = -\psi_0 \mathrm{d}\mu_\psi. \tag{7.28}$$

For the diffuse interface model, the excess surfactant concentration has to be obtained by the integration over the whole diffuse interface [160], and thus the equilibrium equation of state cannot be analytically obtained. Following van der Sman and van der Graaf [90], we also assume that the excess surfactant concentration is proportional to ψ_0, so that the interfacial tension lowering is proportional to that of the sharp interface with a coefficient α, i.e.

$$\mathrm{d}\sigma = -\alpha\psi_0 \mathrm{d}\mu_{\psi,0}. \tag{7.29}$$

Substituting Eq. (7.23) into Eq. (7.29), we can obtain the equilibrium equation of state:

$$\Delta\sigma = \sigma - \sigma_0 = \alpha[k_B T \ln(1-\psi_0) + \frac{C}{2}\psi_0^2], \tag{7.30}$$

where $\sigma_0 = 4\kappa\phi_b^2/3\xi$ is the interfacial tension of "clean" droplet i.e. $\psi = 0$. We find that the coefficient α is a model-dependent constant in Eq. (7.30). In the sharp interface model, $\alpha = 1$, whereas in the diffuse interface model, $\alpha \neq 1$, due to the finite interface thickness. Therefore, α should depend on the excess of surfactant, while it is independent of ψ_0 and $C/k_B T$. For the given values of ψ_c and β, the excess surfactant concentration ψ_{ex} is a function of Ex, ψ_0 and ξ. As α is independent of ψ_0, α only depends on $Ex = \frac{D}{W\xi^2}$ once ξ is specified. Note, unlike the widely used sharp interface model proposed by Stone and Leal [32], the phase-field method can also describe non-equilibrium effect of surfactant adsorption.

7.3 Lattice Boltzmann method

Lattice Boltzmann (LB) method has been widely used by researchers [98–100,161] to model multiphase flows. As a pseudo-molecular method, it solves a discretized version of the Boltzmann equation to track evolution of the distribution function of an assembly of molecules [97]. Here, we will use LB method to simulate multiphase flows described by Eqs. (7.12)-(7.15). For a ternary fluid, we define three particle distribution functions f_i, g_i and h_i on each site of a two-dimensional square lattice with spacing δ_x. The subscript i denotes a particular lattice velocity vector $\vec{e}_i$, defined by $\vec{e}_0 = (0,0)$, $\vec{e}_{1,3} = (\pm c, 0)$, $\vec{e}_{2,4} = (0, \pm c)$, $\vec{e}_{5,7} = (\pm c, \pm c)$ and $\vec{e}_{6,8} = (\mp c, \pm c)$. The lattice velocity parameter c is defined as $c = \delta_x/\delta_t$ with δ_t being the simulation time step.

The macroscopic physical variables are obtained as moments of the PDFs

$$\phi = \sum_i g_i, \quad \psi = \sum_i h_i,$$
$$\rho = \sum_i f_i, \quad \rho\vec{u} = \sum_i f_i \vec{e}_i. \tag{7.31}$$

The time evolution equation for the particle distribution functions, using the standard Bhatnagar-Gross-Krook (BGK) approximation, can be written as

$$f_i(\vec{x}+\vec{e}_i\delta_t, t+\delta_t) - f_i(\vec{x},t) = \frac{1}{\tau_f}[f_i^{eq}(\vec{x},t) - f_i(\vec{x},t)], \tag{7.32}$$

$$g_i(\vec{x}+\vec{e}_i\delta_t, t+\delta_t) - g_i(\vec{x},t) = \frac{1}{\tau_g}[g_i^{eq}(\vec{x},t) - g_i(\vec{x},t)], \tag{7.33}$$

$$h_i(\vec{x}+\vec{e}_i\delta_t, t+\delta_t) - h_i(\vec{x},t) = \frac{1}{\tau_h}[h_i^{eq}(\vec{x},t) - h_i(\vec{x},t)], \tag{7.34}$$

where τ_f, τ_g and τ_h are independent scalar relaxation parameters, and f_i^{eq}, g_i^{eq} and h_i^{eq} are the equilibrium distribution functions for each distribution function.

The equilibrium distribution functions satisfy the conditions of mass and momentum conservation, as well as the additional constraints with the higher order moments:

$$\begin{aligned}
&\sum_i f_i^{eq} = \rho, \quad \sum_i g_i^{eq} = \phi, \quad \sum_i h_i^{eq} = \psi, \\
&\sum_i f_i^{eq}\vec{e}_i = \rho\vec{u}, \quad \sum_i g_i^{eq}\vec{e}_i = \phi\vec{u}, \quad \sum_i h_i^{eq}\vec{e}_i = \psi\vec{u}, \\
&\sum_i f_i^{eq}\vec{e}_i\vec{e}_i^{\mathrm{T}} = \mathbf{P} + \rho\vec{u}\vec{u}^{\mathrm{T}}, \\
&\sum_i g_i^{eq}\vec{e}_i\vec{e}_i^{\mathrm{T}} = \Gamma_\phi\mu_\phi\mathbf{I} + \phi\vec{u}\vec{u}^{\mathrm{T}}, \\
&\sum_i h_i^{eq}\vec{e}_i\vec{e}_i^{\mathrm{T}} = \Gamma_\psi\mu_\psi\mathbf{I} + \psi\vec{u}\vec{u}^{\mathrm{T}}.
\end{aligned} \tag{7.35}$$

Therefore, the dynamics of system is governed by the appropriate set of continuum equations. Explicit expressions for f_i^{eq}, g_i^{eq} and h_i^{eq} are given in Appendix C.

Using the Chapman-Enskog expansion, the lattice Boltzmann model Eqs.(7.32)-(7.34) can lead to Eqs. (7.12)-(7.15) in the long-wavelength and low-frequency limit. The relaxation parameters τ_f, τ_g and τ_h are related to the kinematic viscosity and mobilities through

$$\nu = c_s^2(\tau_f - 1/2)\delta_t, \tag{7.36}$$

$$M_\phi = \Gamma_\phi(\tau_g - 1/2)\delta_t, \quad M_\psi = \Gamma_\psi(\tau_h - 1/2)\delta_t, \tag{7.37}$$

where c_s is the speed of sound which is $c/\sqrt{3}$. Note that we set $\tau_g = \tau_h =$

$1/(3-\sqrt{3})$ to minimize numerical errors of the convection-diffusion scheme [115]. So Γ_ϕ (Γ_ψ) can act as a tunable parameter to control M_ϕ (M_ψ).

In our lattice Boltzmann multiphase model, the calculations of gradient and Laplacian operators are required to evaluate the chemical potentials in Eqs. (7.6) and (7.7) as well as the pressure tensor in Eq. (7.9). To minimize the discretization error, these operators are calculated using 9-point finite difference stencils as follows:

$$\begin{aligned} \nabla\phi(\vec{x}) &= \frac{1}{c_s^2\delta_t}\sum_i w_i\phi(\vec{x}+\vec{e}_i\delta_t)\vec{e}_i, \\ \nabla^2\phi(\vec{x}) &= \frac{2}{c_s^2\delta_t^2}\sum_i w_i[\phi(\vec{x}+\vec{e}_i\delta_t)-\phi(\vec{x})], \end{aligned} \tag{7.38}$$

where w_i is the weight factor with $w_0 = 4/9$, $w_{1-4} = 1/9$ and $w_{5-8} = 1/36$.

7.4 Model validation and applications

7.4.1 Equilibrium properties

First, we will numerically test the present phase-field model's capability for prediction of the profile of surfactant concentration at a planar oil-water interface. The flow domain contains 201×3 square lattices in the xy-plane with an oil phase initially located at $51 \le x \le 150$. The periodic boundary conditions are imposed at all the boundaries. We run our simulations with these parameters: $\sigma_0 = 0.02$, $\xi = 3\delta_x$, $\psi_c = 0.017$, $Ex = 0.17$, $D = \kappa$, $M_\phi = 0.2$, $M_\psi = 0.02$, $\psi_b = \{10^{-4}, 10^{-3}, 5\times10^{-3}\}$, $C = 0$ for the Langmuir adsorption, and $2k_BT$ for the Frumkin adsorption.

Fig. 7.1 (a) shows excellent agreement between our numerical results and the analytical solution given by Eq. (7.27). For the two different adsorption isotherms, the profiles of surfactant concentration exhibit a large difference only when the value of ψ_0 is large. As seen in Fig. 7.1 (b), the predicted solvent composition profile $\phi(x)$ agrees well with the analytical solution, $\phi(x) = \phi_b\tanh(x/\xi)$, in all the cases. Therefore, the results confirm that the solvent composition profile is independent of the surfactant loading, which is assumed in obtaining our analytical solution. However, our numerical prediction will deviate from the analytical solution when ψ_0 is sufficiently large, which may attribute to two factors. The first one is that we cannot obtain Eq. (B.13) with χ approximated by $k_BT(\frac{1}{\psi_b}+\frac{1}{1-\psi_b})-C$

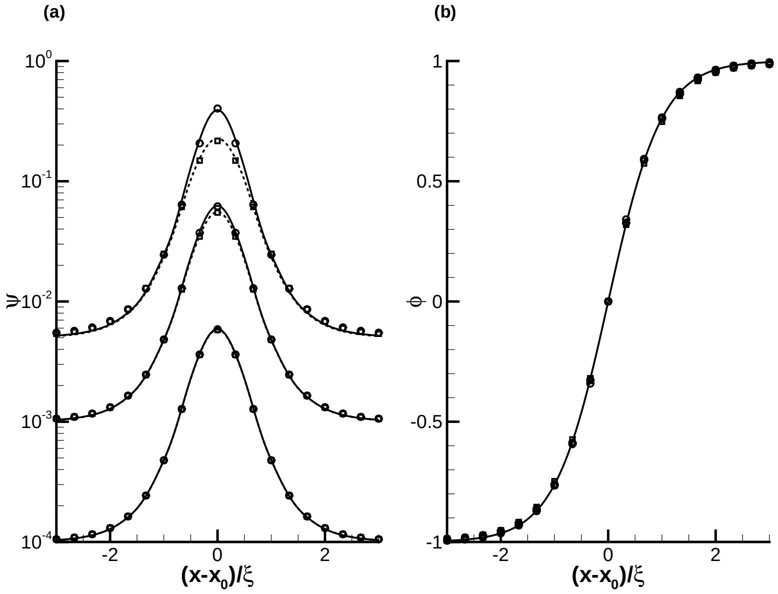

Figure 7.1: (a) Profile of the surfactant concentration for a planar oil-water interface located at $x_0 = 50$ (or $x_0 = 151$) with various parameters listed in the text. Square and circle symbols represent numerical predictions for $C = 0$ and $C = 2k_BT$ respectively, and the dashed and solid lines are the corresponding analytical solutions. (b) Profile of the solvent composition ϕ: the square symbols and circle symbols represent numerical predictions corresponding to $C = 0$ and $C = 2k_BT$ respectively; the solid line is the analytical solution of $\phi(x) = \phi_b \tanh(x/\xi)$.

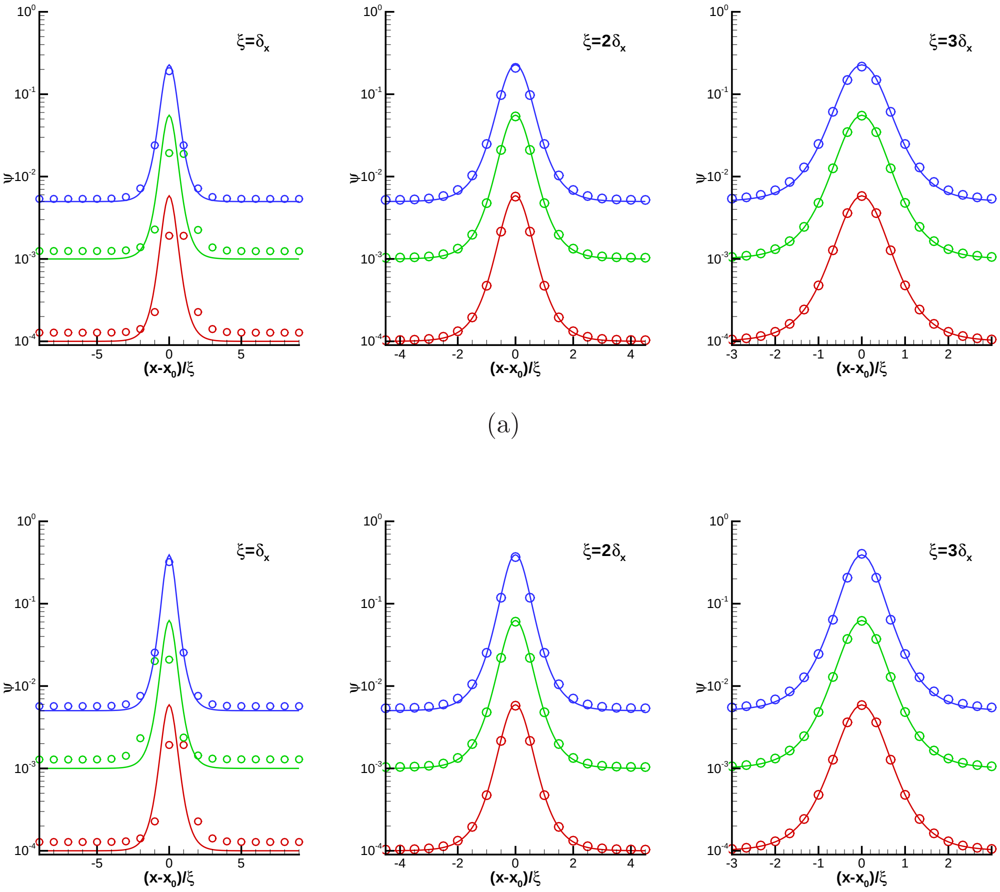

(a)

(b)

Figure 7.2: The effect of ξ on the profile of the surfactant concentration: (a) $C = 0$; (b) $C = 2k_BT$. Simulation results are represented by the discrete symbols, and the solid lines are the analytical solutions.

due to the large surfactant excess at the interface, whereas the analytical solution Eq. (7.27) is derived on the basis of the parameter of the interface thickness satisfying $\xi^2 = \frac{2\kappa}{B\phi_b^2}$. Consequently, the predicted solvent composition profile cannot follow $\phi(x) = \phi_b \tanh(x/\xi)$ with $\xi = 3\delta_x$ as in the present simulation. The other factor may be due to the discretization error for the approximation of $\nabla\psi$, which increases rapidly as ψ_0 becomes large. We have also examined the influence of parameter ξ on the simulation results, which is shown in Fig. 7.2 for $\xi = \delta_x$ and $\xi = 2\delta_x$. It suggests that $\xi = 2\delta_x$ is still acceptable but $\xi = \delta_x$ is not a good choice. To correctly capture the sharp profile of surfactant concentration across the interface, a reasonably thick interface ($\xi \geq 2\delta_x$) is important. Considering the numerical accuracy, we choose $\xi \geq 2\delta_x$ in the following simulations.

Understanding the interfacial tension modification due to the presence of surfactants is practically important. Here, we will perform numerical simulations in a 121 × 121 domain with a droplet whose radius R is 30 lattices centred in the middle of the flow domain. We choose $D = \kappa$, $\psi_c = 0.017$, $\xi/\delta_x = 2$, $M_\phi = 0.1$, $M_\psi = 0.02$, and different values for σ_0, Ex, C and ψ_b. The profiles of ϕ and ψ are initialized with the analytical solutions given by Eqs. (7.20) and (7.27). When the droplet reaches its equilibrium, we calculate the interfacial tension σ by the Laplace law:

$$\Delta p = \frac{\sigma}{R}, \tag{7.39}$$

where Δp is the pressure difference across the droplet interface with the pressure p defined by $p = \frac{1}{2}P_{\alpha\alpha}$.

Eq. (7.30) shows the relation between the lowering of the interfacial tension $\Delta\sigma$ and the surfactant concentration at the interface. To validate this equilibrium relation, seven numerical simulation cases are performed with the following parameters: (1) $\sigma_0 = 0.02$, $Ex = 2$ and $C = 0$, (2) $\sigma_0 = 0.02$, $Ex = 1$ and $C = 0$, (3) $\sigma_0 = 0.01$, $Ex = 0.5$ and $C = 0$, (4) $\sigma_0 = 0.01$, $Ex = 0.5$ and $C = 2k_BT$, (5) $\sigma_0 = 0.01$, $Ex = 0.25$ and $C = 0$, (6) $\sigma_0 = 0.01$, $Ex = 0.25$ and $C = 2k_BT$, (7) $\sigma_0 = 0.01$, $Ex = 0.25$ and $C = 3k_BT$. In Fig. 7.3, we plot $\Delta\sigma/\sigma_0$ as a function of ψ_0, where the coefficient α in Eq. (7.30) is determined by the best fitting of our simulation results. In all these cases, it can be observed that the lowering of the interfacial tension follows the equation of state given by Eq. (7.30) when ψ_0 is not large ($\psi_0 < 0.5$). As we expect, the coefficient α is only dependent on Ex. Specifically, when $Ex = \{0.25, 0.5, 1.0, 2.0\}$, the corresponding values of α are $\{2.0, 2.2, 2.4, 2.8\}$. For a large ψ_0, our simulation results deviate from the analytical solutions of Eq. (7.30), which is also caused by the two factors as discussed in Fig. 7.1. Nevertheless, the intrinsic dependence of $\Delta\sigma$ on ψ_0 still holds.

A numerical artifact observed in many numerical methods is the existence of spurious velocities at the phase interface. Based on the analysis of the flowfield for a clean droplet in quiescent fluid, van der Sman and van der Graaf [121] have shown that the magnitude of the spurious velocities is proportional to the interfacial tension. It is interesting to study the influence of the interfacial tension σ_0 and the surfactant concentration ψ_b on the spurious velocities. Fig. 7.4 shows the maximal spurious velocities as a function of σ_0 for different C and ψ_b at a fixed Ex which is 0.25. It can be clearly seen that the addition of surfactant can decrease the spurious velocities, and the large surfactant concentration leads to

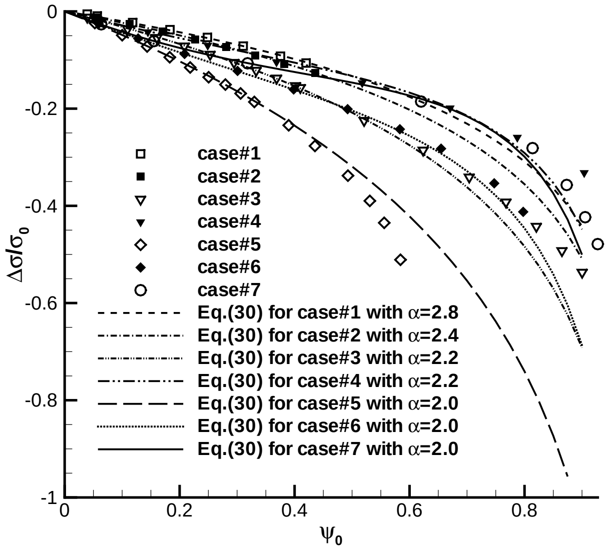

Figure 7.3: The lowering of interfacial tension $\Delta\sigma/\sigma_0$ as a function of the surfactant concentration at the interface ψ_0. The parameters are described in the text. Simulation results are indicated by the discrete symbols, and the lines are the solutions of Eq. (7.30) with the coefficient α determined by the best fitting of the simulation data.

bigger reduction of spurious velocities. For the same C and ψ_b, the magnitude of spurious velocities is also proportional to σ_0, which is similar to the case of a clean droplet. Additionally, a multiphase system is always evolving towards the direction of free energy decreasing in phase-field model. It has been found that small droplets are prone to dissolve in a surfactant-free finite system [121]. This is also observed in the surfactant-contaminated finite systems in our simulations. We also find that the addition of surfactants has negligible effect on dissolution of droplets.

7.4.2 Adsorption dynamics

Ward and Tordai [91] theoretically considered the adsorption dynamics of surfactant molecules from a semi-infinite bulk surfactant solution to an interface. The bulk phase and interface are assumed to have an initial surfactant concentration ψ_b and $\psi_0 = 0$ respectively. Surfactant molecules will diffuse from the bulk phase to the interface due to the concentration gradient. Consequently, the surfactant concentration at the interface will rise, while depleting the surfactants in the layer

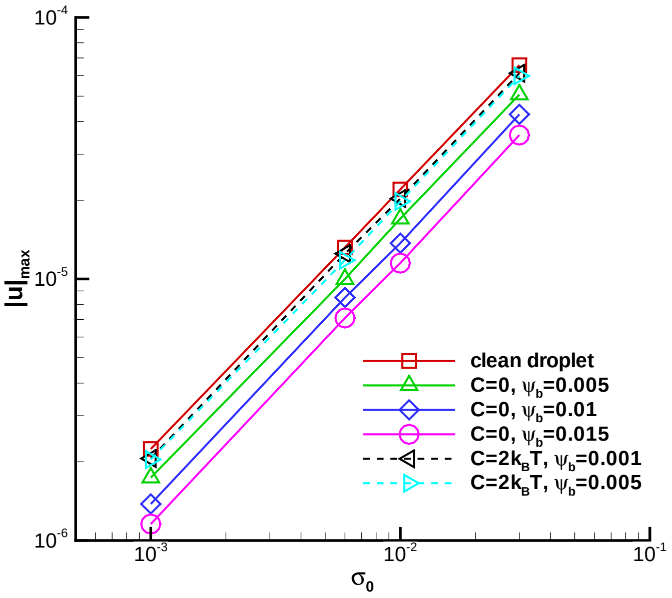

Figure 7.4: The maximal value of spurious velocities $|\vec{u}|$ as a function of σ_0 for both clean and contaminated droplets.

of fluid adjacent to the interface (termed as the subsurface). Soon, the interface is in local equilibrium with the subsurface, and the adsorption process slows down as the surfactant molecules have to transport over longer distances from the bulk phase to the interface. The time-dependent adsorption process can be expressed by [91]

$$\psi_0(t) = 2\sqrt{\frac{D_\psi}{\pi}}\left[\psi_b\sqrt{t} - \int_0^{\sqrt{t}} \psi_s(u)\mathrm{d}\sqrt{t-u}\right], \tag{7.40}$$

where t is time, u is a dummy time-delay variable, and $\psi_s(u)$ is the surfactant concentration at the subsurface. We note that Eq. (7.40) is the analytical solution of the classical Ward and Tordai problem with the governing equation Eq. (7.18) in the sharp interface model, and it can be numerically solved with a given adsorption isotherm which relates the interface excess ψ_0 to ψ_s [162].

We apply the present phase-field model to investigate the Ward and Tordai problem, where an oil-water planar interface with an equal surfactant diffusion coefficient D_ψ in both bulk phases. We adopt the previously used definition of adsorption length $L_{ad} = \psi_{eq}/\psi_b$ [163, 164], where ψ_{eq} is determined by the

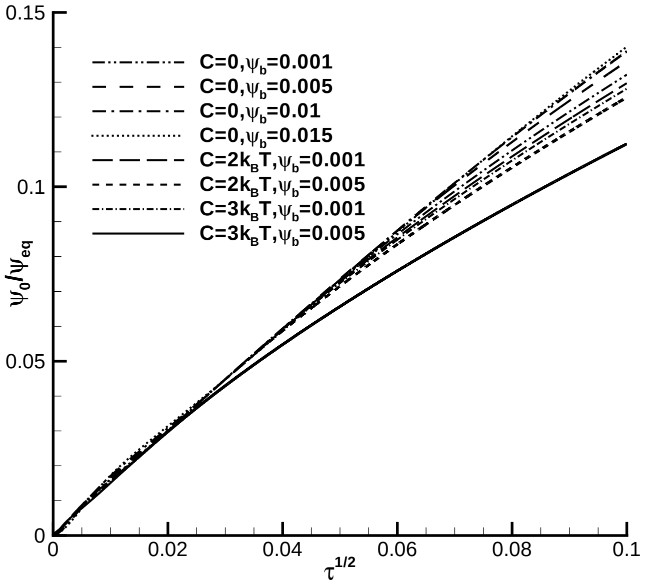

Figure 7.5: Short-time behavior of the surfactant concentration at the interface.

adsorption isotherm:

$$\psi_{eq} = \frac{\psi_b}{\psi_b + \psi_c \mathrm{e}^{-\frac{C}{k_B T}\psi_{eq}}}. \tag{7.41}$$

And we choose the characteristic time as L_{ad}^2/D_ψ, so that the nondimensional time, τ, is tD_ψ/L_{ad}^2 [163, 164]. Therefore, the original dimensional Eq. (7.40), when cast into dimensionless form, becomes

$$\frac{\psi_0(\tau)}{\psi_{eq}} = \frac{2}{\sqrt{\pi}}\sqrt{\tau}, \tag{7.42}$$

for the short-time ($t \to 0$) adsorption behavior in the Ward and Tordai problem. This behavior is independent of the adsorption isotherm and the bulk surfactant concentration. The short-time adsorption behavior is examined using the model in a 400×3 lattices domain with the following parameters: $\psi_c = 0.017$, $Ex = 0.23$, $\xi = 3\delta_x$ and $D = \kappa$. The Langmuir adsorption ($C = 0$) and Frumkin adsorption ($C/k_B T = \{2, 3\}$) are considered with $\psi_b = \{10^{-3}, 5\times10^{-3}, 10^{-2}, 1.5\times10^{-2}\}$ and $\psi_b = \{10^{-3}, 5\times10^{-3}\}$ respectively. Halfway bounce-back boundary conditions [95] are applied at $x = \pm 200$. The simulation results are shown in Fig. 7.5, and we can

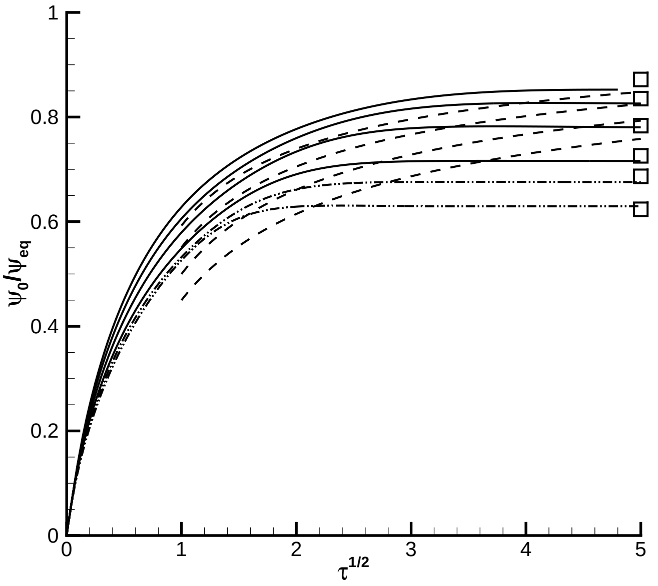

Figure 7.6: Evolution of surfactant concentration at the interface for the Langmuir adsorption with the initial bulk surfactant concentration $\psi_b = \{10^{-3}, 5 \times 10^{-3}, 10^{-2}, 1.5 \times 10^{-2}\}$ (the solid lines from bottom to top), as well as the Frumkin adsorption with $C = 2k_BT$ and $\psi_b = \{10^{-3}, 5 \times 10^{-3}\}$ (the dash-dot-dot lines from top to bottom). The dashed lines show the limiting behavior at $\tau \to \infty$ for the Langmuir adsorption, and the square symbols represent the analytical surfactant loadings in equilibrium.

observe that all the adsorption curves collapse into a single curve for $\sqrt{\tau} < 0.025$:

$$\frac{\psi_0(\tau)}{\psi_{eq}} \approx \frac{2.6}{\sqrt{\pi}}\sqrt{\tau}, \tag{7.43}$$

which is indeed independent of the choice of adsorption isotherm and ψ_b. However, the $\sqrt{\tau}$ behavior follows a different proportionality constant from the sharp interface model, which attributes to a finite thickness of the diffuse interface. It can also be found that the $\sqrt{\tau}$ behavior lasts shorter for $C/k_BT = 3$ and $\psi_b = 5 \times 10^{-3}$ compared to the other adsorption curves. This displays a stronger nonlinear adsorption process for large value of C/k_BT.

In the Ward and Tordai problem, the long-time adsorption behavior should be obtained numerically by solving Eq. (7.40) with a given adsorption isotherm. For the Langmuir adsorption, the long-time adsorption behavior can be approximated by [163]

$$\frac{\psi_0(\tau)}{\psi_{eq}} \approx 1 - \frac{\psi_c}{\psi_c\sqrt{\pi\tau} - \psi_b(1-\sqrt{\pi\tau})}. \tag{7.44}$$

We note that the approximation of Eq. (7.44) corresponds to the long-time behavior in an infinite domain. Fig. 7.6 shows the simulation results of the whole adsorption process in the finite domain with $C = 0$, which are represented by the solid lines. It can be easily seen that the long-time adsorption behavior in a finite domain is different from an infinite domain. Compared with an infinite system, the finite system can equilibrate faster, which is more significant for a lower ψ_b. In a finite system, the initial ψ_b will change as the surfactants are adsorbed to the interface, leading to reduction of ψ_b, which will be more significant for a system with lower initial ψ_b. As the diffusion coefficient is ψ-dependent in our free energy model, the diffusion coefficient D_ψ cannot be accurately approximated by the initial bulk surfactant concentration ψ_b if it is small, whereas it is assumed a constant in obtaining Eq. (7.44). As the initial ψ_b increases, it can be expected that the adsorption behavior in a finite domain becomes closer to the approximation of Eq. (7.44), which is also reflected in Fig. 7.6. In addition, Fig. 7.6 also shows the whole adsorption processes in the finite domain with $C = 2k_BT$ and $\psi_b = \{10^{-3}, 5\times10^{-3}\}$, which are represented by dash-dot-dot lines. In contrast to the Langmuir adsorption, the Frumkin adsorption can equilibrate faster due to more surfactants absorbed to the interface. Finally, we compare the simulation results with the analytical solution of Eq. (7.27) when the finite system is in equilibrium. However, we cannot directly solve Eq. (7.27) to obtain the profile of surfactant concentration because the equilibrium bulk surfactant concentration ψ_b is unknown. For a closed system, the total mass of surfactant m_s should be conserved during the process of surfactant adsorption, i.e.

$$\int \psi \mathrm{d}x = m_s. \tag{7.45}$$

By satisfying the constraint of Eq. (7.45), we can use the two-step Newton's method to solve the nonlinear equation Eq. (7.27) to obtain the concentration profile. Details are given in Appendix D. Fig. 7.6 shows good agreement between simulation data and analytical solution for the equilibrium values of ψ_0/ψ_{eq}.

7.4.3 Surfactant effect on droplet dynamics

We have examined our model equilibrium behavior and surfactant adsorption dynamics. In this section, we apply the present phase-field model to investigate the droplet deformation, breakup and coalescence with the presence of surfactants in shear flows. All simulations are performed in a 2D rectangular domain with periodic boundary conditions on the left and right sides of the domain. The velocity boundary conditions [165] on the top and bottom sides of the domain are prescribed to introduce simple shear flow. The droplet is initially circular with the radius R, while the system is initially at rest. The surfactant concentration starts with the analytical prediction of $\psi(\vec{x})$ for a given ψ_b. The characteristic length and velocity of simulation are chosen to be the droplet radius R and γR respectively, where γ is the shear rate. We introduce the following dimensionless numbers to classify the droplet dynamical behaviour:

$$\lambda = \frac{\eta_d}{\eta_m}, \quad Re = \frac{\rho \gamma R^2}{\eta_m}, \quad Ca = \frac{\gamma R \eta_m}{\sigma_0}, \tag{7.46}$$

where λ is the viscosity ratio of the droplet to the carrier fluid, which we set to be 1 here; Re is the Reynolds number; and Ca is the capillary number. When there are surfactants, interfacial tension will vary. In this case, we use the interfacial tension without surfactants to calculate Ca. In addition, we define the Peclet numbers Pe_ϕ and Pe_ψ, which are associated with the Cahn-Hilliard equations Eq. (7.14) and Eq. (7.15) respectively, as

$$Pe_\phi = \frac{\gamma R \xi}{|D_\phi|}, \quad Pe_\psi = \frac{\gamma R^2}{D_\psi}. \tag{7.47}$$

In the following simulations, we choose $\psi_c = 0.017$, $\xi = 2\delta_x$, $Pe_\phi = 2$ and $Pe_\psi = 100$ so that the physical behavior of droplets in a typical oil/water/surfactant system can be reasonably reproduced.

Droplet deformation and breakup under shear

Here, we perform 2D simulation to examine the surfactant effect on droplet deformation and breakup under a shear flow. Initially, the droplet is circular with the radius $R = 32$, which is placed in the center of a 256×128 lattice flow domain. To study small deformation, we choose $Ca = 0.1$, $Re = 0.1$ and $\sigma_0 = 10^{-3}$. We investigate the effects of surfactant concentration and interac-

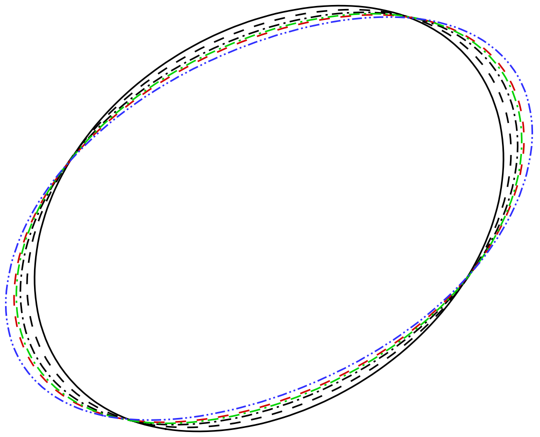

Figure 7.7: The stable shape of a droplet in the simple shear flow ($Ca = 0.1$, $Re = 0.1$ and $\sigma_0 = 10^{-3}$) with the presence of surfactants ($C = 0,\ \psi_b = 5 \times 10^{-3}$, the black dashed line; $C = 0,\ \psi_b = 10^{-2}$, the black dash-dot line; $C = 0,\ \psi_b = 1.5 \times 10^{-2}$, the red dashed line; $C = k_BT,\ \psi_b = 10^{-2}$, the green dash-dot line; $C = 2k_BT,\ \psi_b = 10^{-2}$, the blue dash-dot-dot line) and in the absence of surfactants (the black solid line).

tion coefficient c on droplet formation with two groups of parameters: $C = 0$ and $\psi_b = \{5 \times 10^{-3}, 10^{-2}, 1.5 \times 10^{-2}\}$; and $C/k_BT = \{0, 1, 2\}$ and $\psi_b = 10^{-2}$. For all the chosen parameters, it can be observed that the droplet deforms and eventually evolves to a stable elliptic shape, which is usually characterized by the Taylor deformation parameter, $Df = (a - b)/(a + b)$ with a and b being the major and minor axis of the ellipse. In Fig. 7.7, we have depicted the steady state shapes at $Ca = 0.1$, $Re = 0.1$ and $\sigma_0 = 10^{-3}$ for the clean droplet and the droplets with surfactants. For the droplet with surfactants, we have various ψ_b and C. For the Langmuir adsorption ($C = 0$), increasing surfactant concentration can lead to a more prolate droplet. In addition, with the same surfactant concentration i.e. $\psi_b = 10^{-2}$, a large interaction coefficient C can also produce a highly enlongated droplet. The corresponding time evolution of Taylor deformation parameter is plotted in Fig. 7.8, which reveals the same observations.

During the droplet deformation, surfactant dilution due to the local interfacial stretching will counter the lowering of interfacial tension, and thus preventing the droplet from further deformation. Meanwhile, the surfactants are gradually swept towards the droplet tips under the action of shear flow, resulting in the non-uniform distribution of the interfacial tension where the smallest interfacial

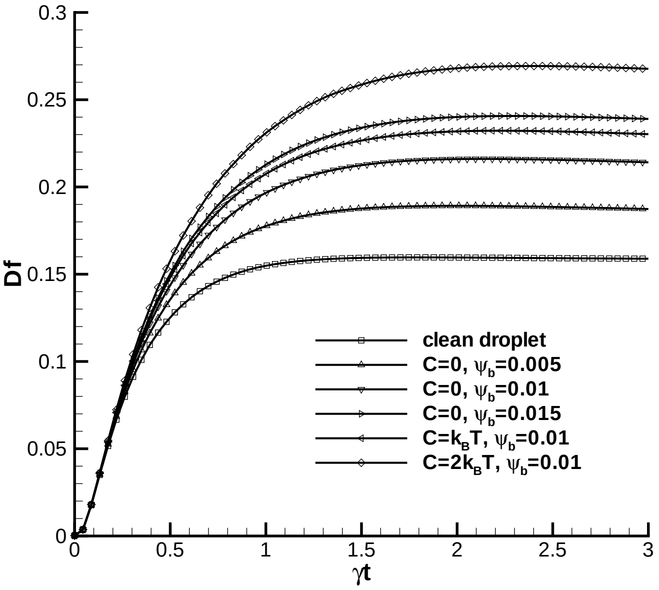

Figure 7.8: The time evolution of Taylor deformation parameter for a droplet in the shear flow with $Ca = 0.1$, $Re = 0.1$ and $\sigma_0 = 10^{-3}$.

tension occurs at the droplet tips. The Marangoni force will arise due to the gradient of interfacial tension, which resists the further migration of surfactants. Consequently, the droplet may have a stable deformed shape. For the stable droplet, we also calculate the droplet inclination angle θ (the angle between the orientation of the major ellipse axis and the horizontal axis) using the method of moments [121]. The calculated inclination angles are: $\theta = 35.58$ degrees for the clean droplet, for the droplet with surfactants, θ is 32.76 degrees ($C = 0,\ \psi_b = 5\times 10^{-3}$), 31.21 degrees ($C = 0,\ \psi_b = 10^{-2}$), 30.03 degrees ($C = 0,\ \psi_b = 1.5\times 10^{-2}$), 30.33 degrees ($C = k_BT,\ \psi_b = 10^{-2}$), and 28.70 degrees ($C = 2k_BT,\ \psi_b = 10^{-2}$), respectively. The presence of surfactants acts to promote the droplet deformation and reduce the droplet inclination angle.

When we increase the capillary number and the Reynolds number, the droplet cannot evolve to a steady shape. Fig. 7.9 shows the time evolution plots of droplet deformation in the simple shear flow with $Ca = 0.5$, $Re = 1.0$ and $\sigma_0 = 10^{-3}$. The other parameters are kept to be the same as the above. As expected, the droplet deforms more significantly when ψ_b and C increase, which is consistent with the cases of small Ca and Re. If we continue to increase the capillary number and Reynolds number, a critical droplet state may appear, i.e. the droplet

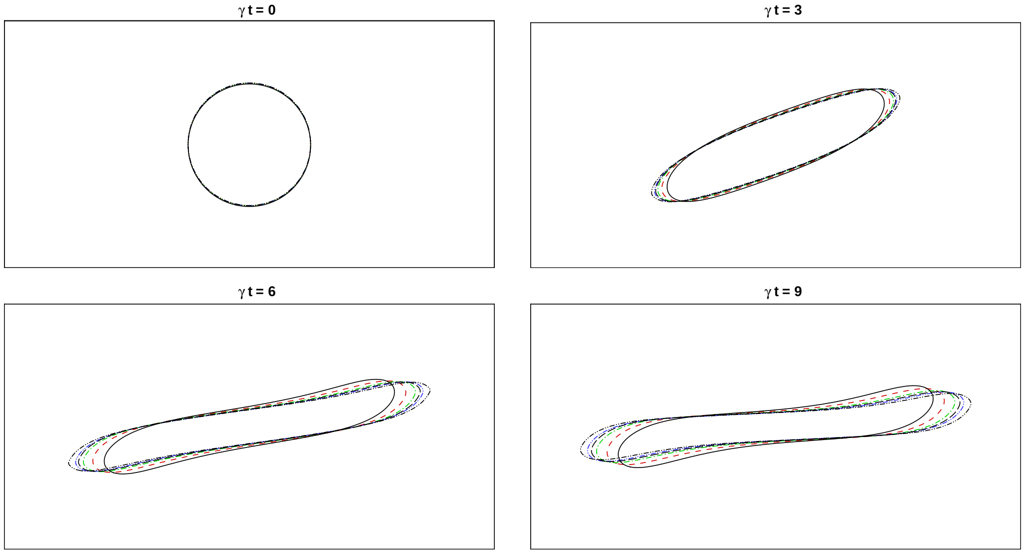

Figure 7.9: The time evolution of a droplet in the shear flow ($Ca = 0.5$, $Re = 1.0$ and $\sigma_0 = 10^{-3}$) with the presence of surfactants ($C = 0,\ \psi_b = 5 \times 10^{-3}$, the red dashed line; $C = 0,\ \psi_b = 10^{-2}$, the green dash-dot line; $C = 0,\ \psi_b = 1.5 \times 10^{-2}$, the blue dash-dot-dot line; $C = k_BT,\ \psi_b = 10^{-2}$, the black long-dash line; $C = 2k_BT,\ \psi_b = 10^{-2}$, the black dash-dot-dot line) and in the absence of surfactants (the black solid line).

will breakup as the surfactant concentration exceeds a critical value. In order to capture the underlying physics of droplet breakup, we consider a 640 × 160 computational domain with a droplet of initial radius $R = 40$ lattices. The simulation starts with the clean droplet ($Ca = 0.6$, $Re = 2.4$ and $\sigma_0 = 10^{-3}$). As the surfactant concentration increases, Fig. 7.10 shows that the droplet breakup begins at some critical value for both $C = 0$ and $C = 2k_BT$. When the droplet breakup occurs, the increasing of ψ_b or C can accelerate the droplet breakup process, and smaller daughter droplets will be generated. In addition, we notice that the droplet will shrink again once the maximal deformation is not enough to "pinch-off" the droplet.

Collision of two equal-sized droplets

We consider the effect of surfactant dynamics on droplet-droplet interactions in the simple shear flow with $Ca = 0.1$, $Re = 0.4$ and $\sigma_0 = 10^{-3}$. We consider two initially circular droplets with the radius of 40 lattices and located at (101, 141) and (261, 101). The 2D computational domain is $[1, 361] \times [1, 241]$. In Fig. 7.11, the droplet evolution is shown at the times (γt) of 0, 2.5, 5.0, 5.5, 7.5 and 8.0.

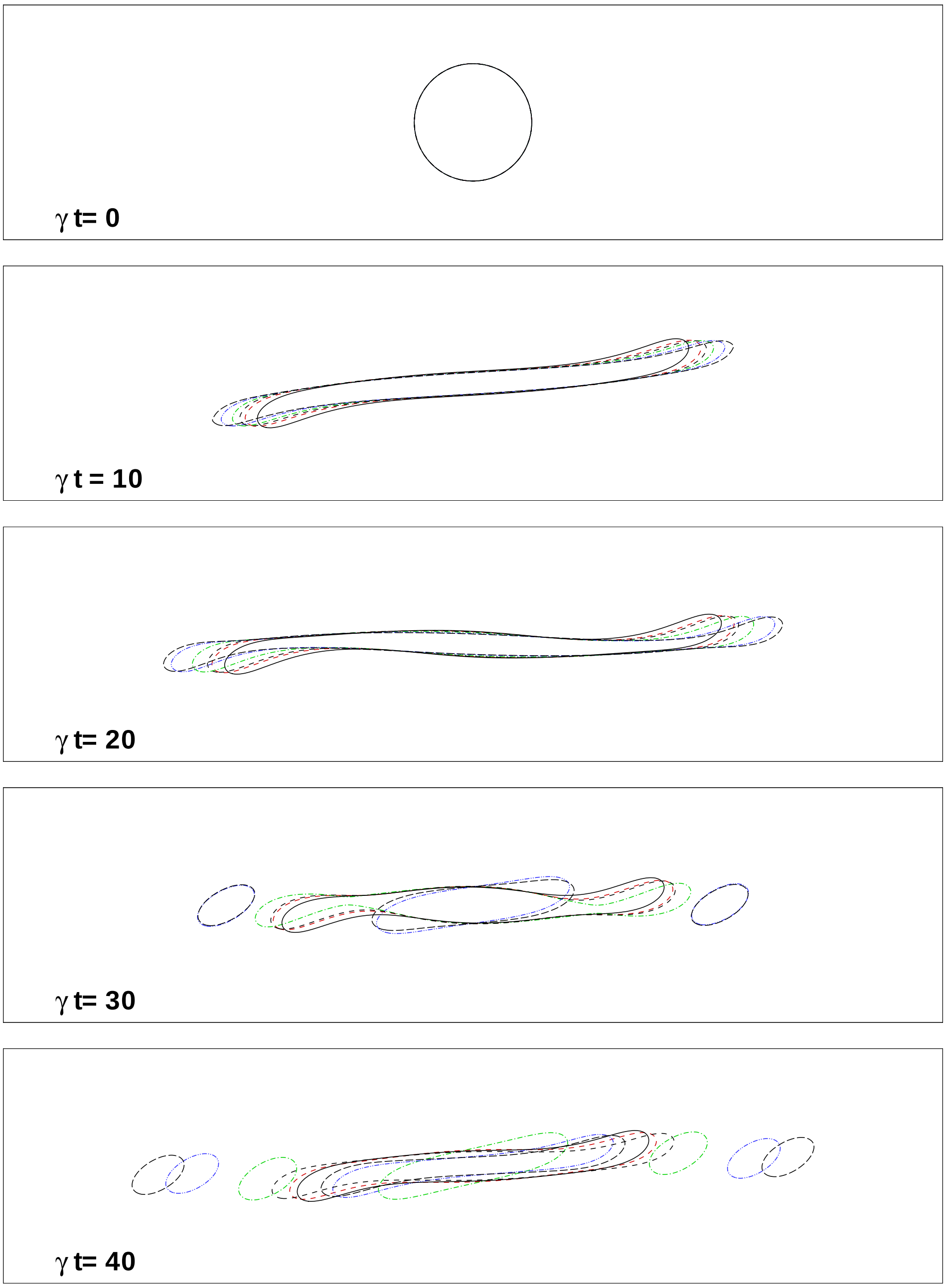

Figure 7.10: Evolution of droplet breakup in the shear flow ($Ca = 0.6$, $Re = 2.4$ and $\sigma_0 = 10^{-3}$) with the presence of surfactants ($C = 0,\ \psi_b = 5 \times 10^{-3}$, the red dashed line; $C = 0,\ \psi_b = 10^{-2}$, the green dash-dot line; $C = 0,\ \psi_b = 1.5 \times 10^{-2}$, the blue dash-dot-dot line; $C = 2k_BT,\ \psi_b = 5 \times 10^{-3}$, the black dashed line; $C = 2k_BT,\ \psi_b = 10^{-2}$, the black long-dash line.) and in the absence of surfactants (the black solid line).

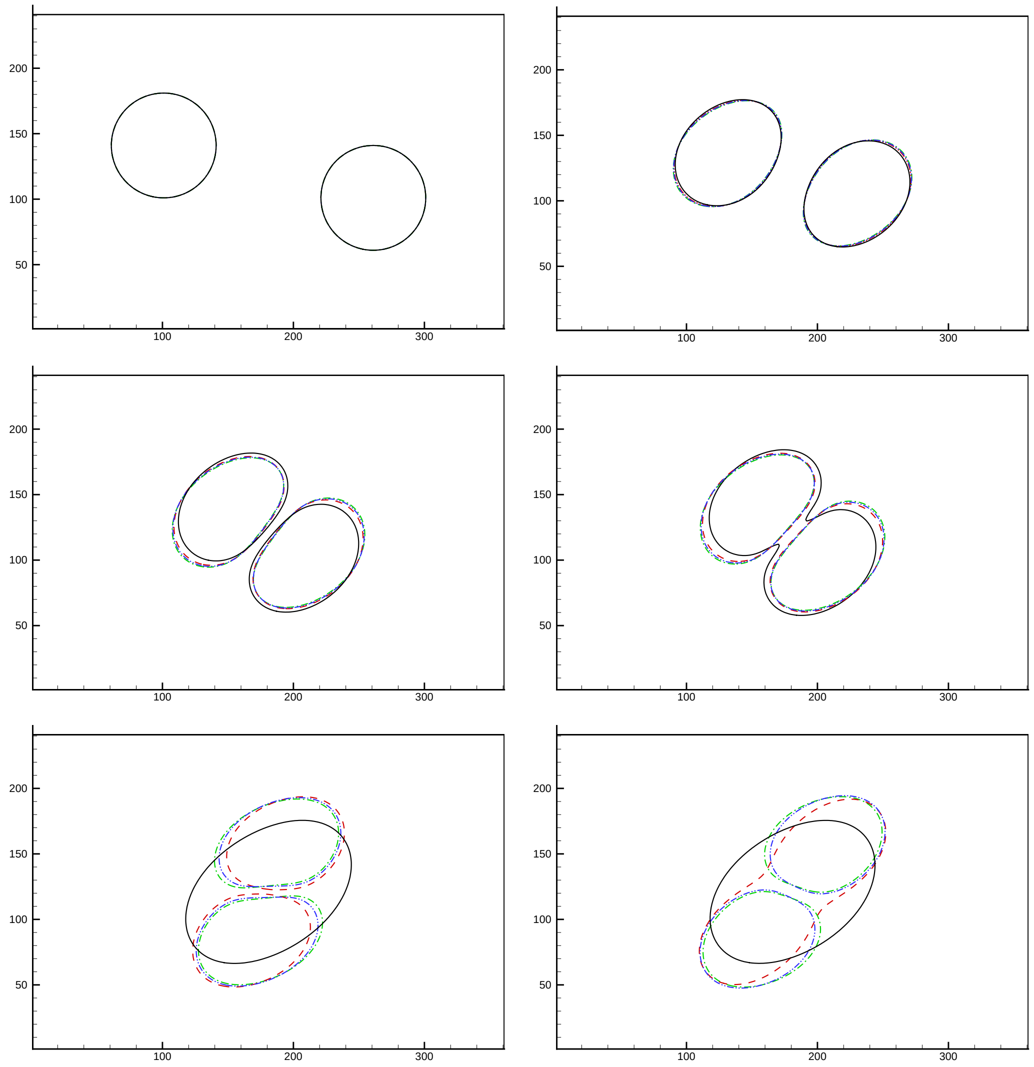

Figure 7.11: The glancing collision of two droplets in the shear flow ($Ca = 0.1$, $Re = 0.4$ and $\sigma_0 = 10^{-3}$) with the presence of surfactants ($C = 0,\ \psi_b = 5 \times 10^{-3}$, the red dashed line; $C = 0,\ \psi_b = 10^{-2}$, the green dash-dot line; $C = 2k_BT,\ \psi_b = 5 \times 10^{-3}$, the blue dash-dot-dot line) and in the absence of surfactants (the black solid line).

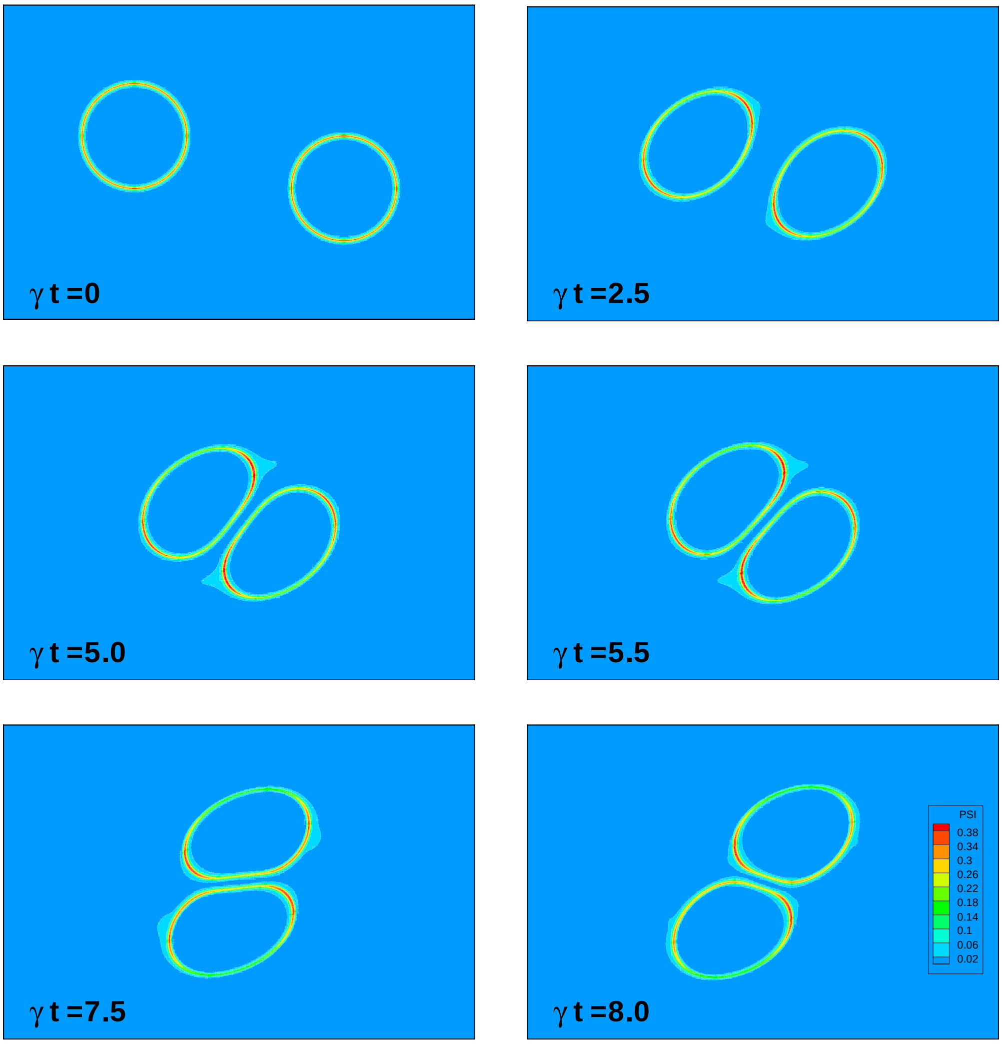

Figure 7.12: Evolution of surfactant concentration of two colliding droplets in the simple shear flow ($Ca = 0.1$, $Re = 0.4$, $\sigma_0 = 10^{-3}$, $C = 0$, and $\psi_b = 10^{-2}$).

We find that the droplet coalescence due to collision is dramatically hindered by the presence of surfactant molecules, which has also been experimentally observed [139, 166–168]. The surfactants have little effect on the droplet behavior, until the two droplets move close to each other. When the two droplets are in close contact, the surfactant concentration and the adsorption isotherm have significant influence on droplet coalescence. The increase of ψ_b or C prevents the droplets from merging.

Fig. 7.12 shows the contour plot of surfactant concentration of two colliding droplets in the simple shear flow ($\psi_b = 10^{-2}$ and $C = 0$). At the beginning, the surfactant molecules are convected towards the droplet tips. As the two droplets approach each other, the increased pressure in the gap between the two droplets pushes surfactants away from the near-contact region. We can clearly see that the surfactant concentrations are unevenly distributed along the interfaces, thus generating the Marangoni stress that affects the droplet-droplet interaction. In addition, the reduction of interfacial tension due to the presence of surfactants can enhance droplet deformation, and thus affect droplet-droplet interaction as well. The dimple forming in the near-contact region, which has been observed during the collision of two droplets using the sharp interface model with insoluble surfactant [80, 142], is not clear in our simulations. It is because the dimple is produced by the a high repulsive lubrication pressure at $d \ll R$ (d is the gap between two droplets), whereas the diffuse interface model underpredicts the lubrication pressure when $d/\xi < 1.5$ [108].

As we know, the increase of the effective capillary number (Ca_e) due to the presence of surfactants can inhibit the droplet coalescence. However, what is the role of Marangoni stress during the droplet coalescence? To answer this question, we have simulated two cases where the effective capillary number is the same, i.e. $Ca_e = 0.1$, for the droplets with surfactants ($C = 0, \psi_b = 10^{-2}$) and the clean droplet. The other parameters are kept the same as the above. The effective capillary number is defined by

$$Ca_e = \frac{\gamma R \eta_m}{\sigma_e}, \tag{7.48}$$

where σ_e is the initial equilibrium interfacial tension, which is the same as σ_0 for the clean droplet and smaller than σ_0 for the droplets with surfactants. To ensure the two cases having the same effective interfacial tension, we need to calculate the required σ_0 for the droplets with surfactants as

$$\sigma_0 = \frac{\sigma_e}{1 - \frac{0.375\alpha}{\xi \ln \psi_c}(1 + \frac{1}{Ex})[\ln(1 - \psi_0) + \frac{1}{2}\tilde{C}\psi_0^2]}. \tag{7.49}$$

where $\tilde{C} = \frac{C}{k_B T}$. Therefore, the σ_0 is different for the two cases.

In the present simulation, α is 2.0 for $Ex = 0.25$. Fig. 7.13 shows the evolution of droplet collision with $Ca_e = 0.1$, $Re = 0.4$ and $\sigma_e = 10^{-3}$ (in the presence of surfactants, $C = 0$ and $\psi_b = 10^{-2}$). Although the two cases have the same effective capillary number, it can be found that the Marangoni stress induced by non-uniform interfacial tension acts as an additional repulsive force to prevent droplet coalescence.

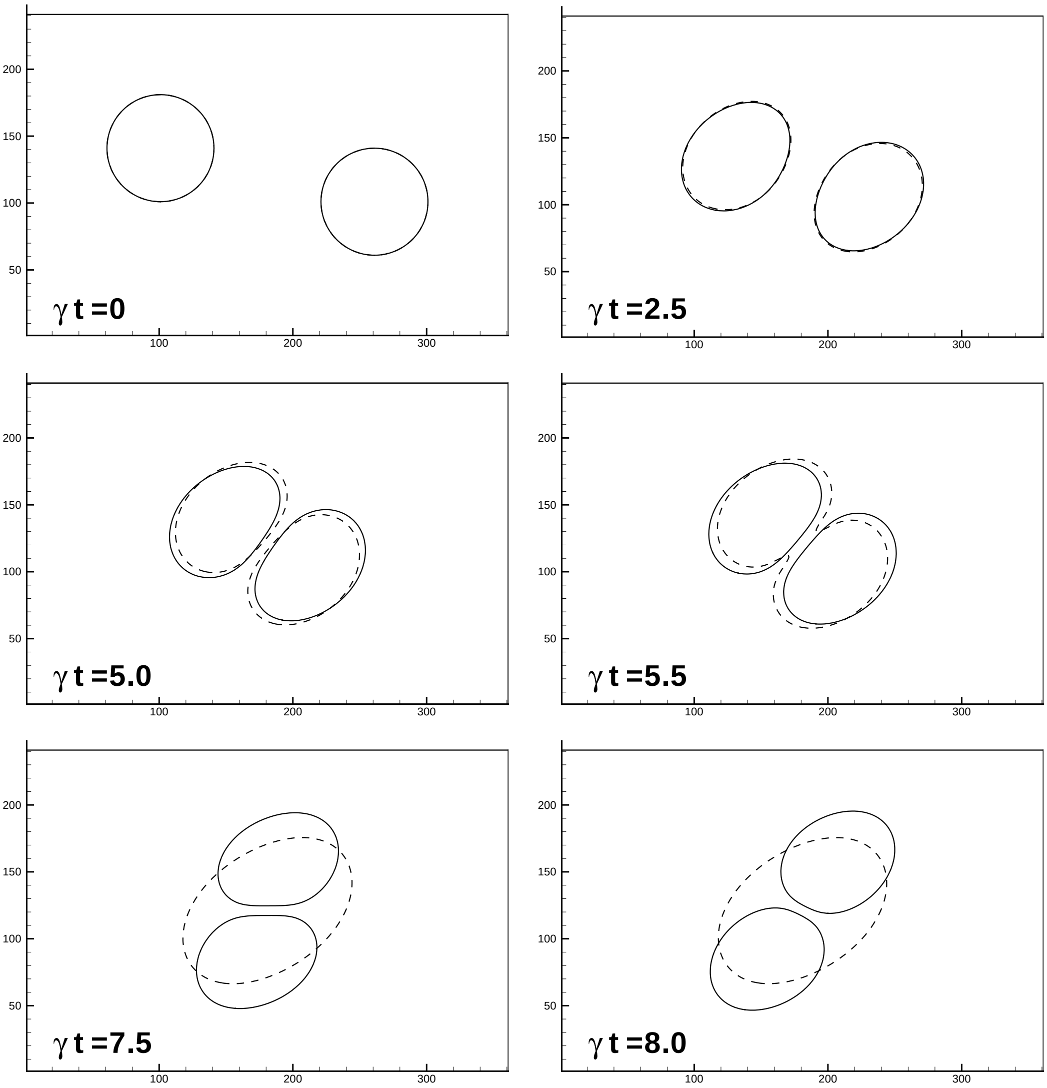

Figure 7.13: The glancing collision of two droplets in the shear flow ($Ca_e = 0.1$, $Re = 0.4$ and $\sigma_e = 10^{-3}$) with the presence of surfactants ($C = 0,\ \psi_b = 10^{-2}$, the solid line.) and in the absence of surfactants (the dashed line).

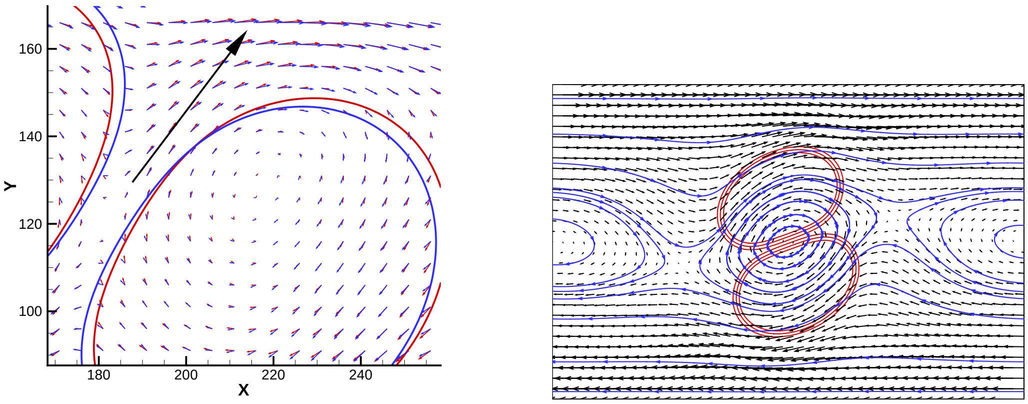

(a)

(b)

Figure 7.14: (a) Velocity vectors are shown at every fifth grid point in the vicinity of the gap at $\gamma t = 4.0$ ($Ca_e = 0.1$, $Re = 0.4$ and $\sigma_e = 10^{-3}$). The red line is the droplet interface with the surfactants while the blue line is the interface of the clean droplet. (b) The flowfield is shown at every eighth grid point ($\gamma t = 7.0$) for droplets collision-separation in the presence of surfactants ($C = 0$ and $\psi_b = 10^{-2}$). The red solid lines are ϕ contours of 0 and ± 0.8, the blue lines are the streamlines.

To show the effect of Marangoni stress on the flowfield, Fig. 7.14(a) gives the comparison of the velocity vectors in the vicinity of the gap at the drainage time $\gamma t = 4.0$ with surfactants ($C = 0$ and $\psi_b = 10^{-2}$, the red arrows) and without surfactants (the blue arrows). It can be clearly seen that the gap between the two droplets without surfactants is narrower, which indicates that the presence of surfactants does slow down the film drainage process and thus increases the required drainage time prior to coalescence. It has been demonstrated that the surfactants can immobilize the bubble interface due to the effect of Marangoni stress during the motion of buoyancy-driven bubbles in a circular tube [143]. The Marangoni stress can also lead to reduction of the interface mobility during the droplet-droplet interaction, though the reduction is not as significant as that in the bubble deformation, where the viscosity ratio of bubble to carrier fluid is small. The Peclet number will increase as the mobility decreases, which can lead to droplet collision-separation [110]. Fig. 7.14(b) shows the flowfield at $\gamma t = 7.0$ ($C = 0$ and $\psi_b = 10^{-2}$), where the streamlines are self-closed circle-like with the two droplets rotating like rigid bodies, which was also observed by Yu and Zhou [110].

As found from the above, the presence of surfactants can increase the droplet deformation and reduce the droplet inclination angle. We also know that the presence of surfactants leads to the increase of Ca_e, which can increase the droplet deformation and reduce the droplet inclination angle. To understand the mechanism of droplet deformation when the surfactants are present, we re-examine the droplet deformation with three groups of different parameters: (1) clean droplet with $Ca = Ca_e = 0.1$, $Re = 0.1$ and $\sigma_0 = \sigma_e = 10^{-3}$; (2) contaminated droplet with $Ca = 0.1$, $Re = 0.1$, $\sigma_0 = 10^{-3}$, $\psi_b = 10^{-2}$ and $C = 0$, so that $Ca_e = 0.127$ and $\sigma_e = 7.87 \times 10^{-4}$; and (3) clean droplet with $Ca = Ca_e = 0.127$, $Re = 0.1$ and $\sigma_0 = \sigma_e = 7.87 \times 10^{-4}$. The group 3 has the same effective capillary number as the group 2, which is designed to single out the effect of the increase of Ca_e on droplet deformation when the surfactants are added. Fig. 7.15 gives the evolutions of the Taylor deformation parameter for the above three groups of data. The total amount of deformation Δ has two parts: Δ_1, due to the Marangoni stresses induced by redistribution of the surfactants, and Δ_2, stemming from the increase of Ca_e due to the surfactant adsorption. For the present case, it is clear that the effect of Marangoni stresses is significant. We expect that the Marangoni stresses are smaller for the soluble surfactants than the insoluble ones due to the bulk diffusion, which can redistribute the surfactants through desorption from the droplet tips and adsorption in the middle regions of the droplet. The steady inclination angle is obtained with $\theta = 33.23$ degrees for the group 3 in contrast to $\theta = 35.58$ degrees for the group 1 and $\theta = 31.21$ degrees for the group 2. Therefore, when the surfactants are presented, the Marangoni stresses and the increase of Ca_e are responsible for the increase of the droplet deformation and the reduction of the droplet inclination angle.

7.5 Conclusions

We have proposed a generalized free energy functional to enable the phase-field model to capture surfactant dynamics in a multiphase system with the bulk surfactant concentration below CMC. In comparison with the other multiphase/surfactant models, the present model can describe evolution of the interface and the surfactant concentration automatically. In equilibrium, this model can lead to the commonly-used surfactant adsorption isotherms, i.e. the Langmuir and Frumkin isotherms. In addition, our model can deal with different solubility of surfactants in the bulk phases. The lowering of interfacial tension caused by the surfactant concentration at the interface, is theoretically and numerically

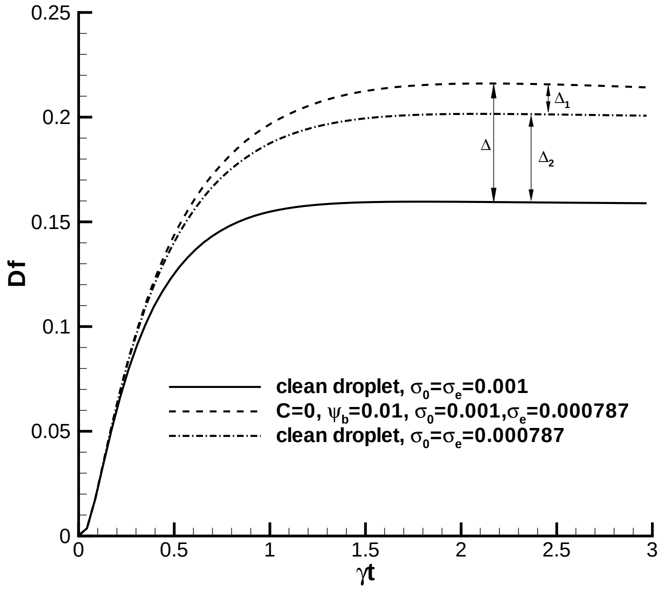

Figure 7.15: The time evolution of Taylor deformation parameter for a droplet in the shear flow with $Ca = 0.1$, $Re = 0.1$ and $\sigma_e = 10^{-3}$.

analysed.

For the Ward and Tordai problem, the interface surfactant loading ψ_0/ψ_{eq} follows $\sqrt{\tau}$ behavior for short time period. For long time period, we find that the surfactant adsorption behavior in a finite system is significantly different from an infinite system as the finite system can equilibrate faster. The surfactant concentration ψ_b and the interaction coefficient C have been found to have big impact on the droplet formation, breakup and collision in a simple shear flow. The increase of ψ_b and C can promote the droplet deformation, decrease the droplet inclination angle, and accelerate the droplet breakup. Smaller daughter droplets are expected to emit for large ψ_b or C. The droplets will less likely merge when the surfactants are introduced, and the increase of ψ_b and C makes the droplet coalescence more difficult. The reasons are that the effective capillary number is increased due to the reduction of interfacial tension, and the time required for film drainage to the point of film rupture is increased due to the Marangoni effect.

Chapter 8

Summary and Conclusions

8.1 Introduction

In this thesis, the lattice Boltzmann phase-field models have been developed and applied to investigate droplet dynamical behavior in microfluidic devices. First, we have introduced a LB phase-field model for a binary fluid, which is built upon the Cahn-Hilliard free energy theory. The model has been validated against a series of test cases including stationary droplet, static contact angle, single droplet deformation and breakup in a simple shear flow, coalescence of two equal-sized droplets induced by the interfacial tension and a simple shear flow, and contact line dynamics of a droplet attached on a substrate subject to a shear flow. This model was then applied to investigate the droplet formation in a microfluidic T-junction and subsequently in a microfluidic cross-junction. The influences of various dimensionless parameters (including the wettability of channel walls), which control the droplet breakup in the confined geometries, have been systematically studied, revealing some new flow physics. Finally, a novel phase-field model was proposed to model interfacial flows with soluble surfactants. Its feasibility and capability have been extensively examined for the problems with analytical solutions and the classical Ward and Tordai problem [91]. This model was then used to investigate the influence of surfactant adsorption on the droplet deformation, breakup and coalescence, showing great potential for simulating surfactant adsorption dynamics in an oil/water/surfactant system.

8.2 Summary

The major contributions of this work are:

1. Development and evaluation of a lattice Boltzmann phase-field model for a binary fluid, which significantly reduces unphysical velocities at the interface and incorporates the wetting of solid walls in a simple and efficient way. Noticeably, this model can still produce correct results for static contact angles when the two phases have different viscosities. However, the Swift's free energy model with the wetting boundary condition proposed by Briant et al. [119] fails to do this due to strong spurious velocities in the steady state [36].

2. Development of a stress-free outlet boundary condition, which introduces a mass modification for the rest particle distribution function by considering the effect of velocity profile. This boundary treatment can conserve the total mass of an incompressible flow system and improve numerical stability for the flows with low Reynolds number. Also, it can be directly applied at the outlet boundary with an arbitrarily given contact angle, whereas the pressure boundary condition proposed by Zou & He [165] has to be carried out with an expansion section where the fluid has to be only one pure single-component [169, 170].

3. Simulations of contact line motion of a droplet sitting on a stationary substrate subject to a shear flow, which indicate that, for a fixed mobility in the slip mode, the advancing and receding contact angles both exhibit a linear dependence on the moving velocity of upper wall, and the advancing contact angle θ_A can be related to the static contact angle θ_S and the contact line capillary number Ca_{cl} by $\cos(\theta_A) = \cos(\theta_S) - Ca_{cl}\ln(KL/l_s)$ [127].

4. Direct numerical simulations of droplet formation in a microfluidic T-junction. The influence of various dimensionless parameters has been systematically investigated, verifying some existing numerical and experimental findings and revealing some new flow physics.

5. Direct numerical simulations of droplet formation in a microfluidic cross-junction, showing that two different regimes, namely the squeezing-like regime and the dripping regime, are clearly identified with the transition occurring at a critical capillary number $Ca_{cr} = 0.01$. In squeezing-like

regime ($Ca \leq Ca_{cr}$), our simulation results reproduced the experimental observations of Tan et al. [15]. Also, we identified that in the dripping regime ($Ca \leq Ca_{cr}$), the viscous force is dominant and the droplet size quickly becomes independent of the flow rate ratio as the capillary number increases. At small flow rate ratios, the squeezing-to-dripping transition becomes indistinguishable for various viscosity ratios, leading the scaling law (which correlates the generated droplet size to the flow rate ratio and capillary number) in the squeezing-like regime to be still valid for the cases with small flow rate ratio.

6. Development and evaluation of a novel phase-field model for interfacial flows with soluble surfactant, showing that the model can recover the Langmuir and Frumkin adsorption isotherms in equilibrium, and the surfactant can have different solubility in both phases. From the equilibrium equation of state, one can determine the interfacial tension lowering scale according to the interface surfactant concentration. The model is able to capture short-time and long-time adsorption dynamics of surfactants. The model has been applied to examine the effect of soluble surfactants on droplet deformation, breakup and coalescence in a simple shear flow. The increase of surfactant concentration and attractive lateral interaction can enhance droplet deformation, promote droplet breakup, and inhibit droplet coalescence. It has also been demonstrated that the Marangoni stresses can reduce the interface mobility and slow down the film drainage process, thus acting as an additional repulsive force to prevent the droplet coalescence.

8.3 Future Work

In this thesis, the potential of the LB phase-field models to simulate a wide range of droplet dynamical problems has been demonstrated. The underlying physical mechanisms of droplet dynamics are found to be well captured by these models. However, the current simulations have only been conducted in 2D. For realistic microfluidic devices, “3D effects” have significant effect on droplet behavior due to large surface-to-volume ratio. For example, the experiment of Garstecki et al. [20] and a recent numerical study of Gupta & Kumar [131] found that the channel depth plays an important role for the generation of plugs in T-junctions, and small channel depth can promote the squeezing mechanism, leading to smaller droplets. To quantitatively describe droplet dynamics in microchannels, 3D numerical simulations are required. Our current simulations are also limited to the microchannel with specific dimensions, so 3D simulations would also be necessary to understand the influence of the channel geometry (e.g. various groups of h/w_c and w_d/w_c in T-junctions) on the droplet formation.

Since the phase-field models resolve the interface structure, a few grid points are required to accurately describe smooth variation of the order parameter across the interface. However, for example, for a droplet of 10 μm diameter with an interface thickness of 10 nm (a typical liquid-liquid interface is less than 10 nm), if the geometry channel is 1000 μm long with a 200 μm^2 cross-sectional area we would need more than 10^{13} grid points for uniform lattice grids if the interface is to span 5 lattices. Even worse, the time step for droplet motion needs to be sufficiently small to avoid divergence of the solution. This is clearly beyond the reach of today's computer technology. Therefore, the current phase-field simulations have to artificially enlarge the interface thickness. In this sense, it is very desirable to incorporate some sophisticated mesh adaptation techniques for the study of interfacial flows. When the grid is refined in interfacial regions, both accuracy and efficiency of the simulations can be improved.

The current study of surfactant effect on the droplet dynamical behavior is still preliminary and it would be interesting to investigate the influence of surfactants and surfactant concentration on droplet formation in a microchannel. Although our novel phase-field model is able to model different solubility of surfactants in the bulk phases, numerical studies are required to examine its feasibility. It would be desirable to apply the present model to investigate the influence of surfactant solubility on the droplet formation in a microchannel. The neutral wetting of walls is only considered in the simulations of the contact line motion, and it will be interesting to simulate how wettability affects slip velocity of the contact line and the contact angle hysteresis. Also, it deserves further study on displacement of the contact line of a droplet on an inhomogeneous surface.

The models and computations in this thesis are limited to a binary fluid with the same densities for both fluids. To model and simulate realistic multiphase systems, the multiphase models with high density ratio are also required, e.g. the density ratio of liquid-gas systems is usually larger than 100, and the density ratio of water to air is about 1000. Modelling and simulation of multiphase flows with high density ratio is a challenging task due to large density jump across the interface. In recent years, several LB multiphase models [151, 171, 172] have been developed to simulate the multiphase flows with high density ratio, and the wetting boundary treatment has been included in these models [173–175]. It will be desirable to apply these models for complex droplet dynamical behavior (e.g. bubble formation in microchannels) and test their instability and accuracy. Another serious limitation is that the present models cannot simulate a fluid with low viscosity ($\nu \leq 0.01$). Due to the use of the BGK collision approximation, the present models are sensitive to the choice of relaxation time, τ. Smaller τ, which implies lower viscosity, can lead to numerical instability. Multiple relaxation time lattice Boltzmann model [176] may help extend the lower limit of viscosity. This model is based upon using several relaxation times instead of the single relaxation time employed in the BGK models. By using additional relaxation times, different physical parameters can be independently adjusted. In this manner the bulk viscosity can be adjusted independently from the shear viscosity, which can lead to numerically stable results at lower relaxation times if selected properly.

To conclude, modelling small scale multiphase flows in confined geometries becomes more and more important as the rapid development of micro- and nano-fluidic technologies. It is an exciting opportunity to explore this field, but it is also challenging due to its multidisciplinary nature, across the boundaries of condensed matter, electronics, magnetism and optics, physical chemistry, fluid dynamics, and numerical computation. More efforts are required to improve our understanding of the small world so that the unique physics at these scales can be utilized to develop future flow technologies.

Appendix A

Chapman-Enskog expansion

The Chapman-Enskog multiscale expansion procedure is applied to derive the macroscopic governing equations for a binary fluid.

Recall that for the LB phase-field model for a binary fluid, two sets of LB equations are given by Eqs. (3.18)–(3.21), i.e.

$$f_i(\vec{x}+\vec{e}_i\delta_t, t+\delta_t) - f_i(\vec{x},t) = -\frac{1}{\tau_f}[f_i(\vec{x},t) - f_i^{eq}(\vec{x},t)] + F_i(\vec{x},t), \tag{A.1}$$

$$g_i(\vec{x}+\vec{e}_i\delta_t, t+\delta_t) - g_i(\vec{x},t) = -\frac{1}{\tau_g}[g_i(\vec{x},t) - g_i^{eq}(\vec{x},t)]. \tag{A.2}$$

The following expansions are applied based on the Chapman-Enskog method:

$$f_i(\vec{x}+\vec{e}_i\delta_t, t+\delta_t) = f_i(\vec{x},t) + \epsilon(\partial_t + e_{i\alpha}\partial_\alpha)f_i + \frac{1}{2}\epsilon^2(\partial_t + e_{i\alpha}\partial_\alpha)(\partial_t + e_{i\beta}\partial_\beta)f_i + \mathcal{O}(\epsilon^3) \tag{A.3}$$

$$f_i = f_i^{eq} + \epsilon f_i^{(1)} + \epsilon^2 f_i^{(2)} + \mathcal{O}(\epsilon^3) \tag{A.4}$$

$$g_i(\vec{x}+\vec{e}_i\delta_t, t+\delta_t) = g_i(\vec{x},t) + \epsilon(\partial_t + e_{i\alpha}\partial_\alpha)g_i + \frac{1}{2}\epsilon^2(\partial_t + e_{i\alpha}\partial_\alpha)(\partial_t + e_{i\beta}\partial_\beta)g_i + \mathcal{O}(\epsilon^3) \tag{A.5}$$

$$g_i = g_i^{eq} + \epsilon g_i^{(1)} + \epsilon^2 g_i^{(2)} + \mathcal{O}(\epsilon^3) \tag{A.6}$$

where $\epsilon = \delta_t$, which is small compared to the macroscopic time scales.

The LB equation for the PDF f_i used for the flowfield is studied first. After the expansion, the LHS of Eq. (A.1) becomes

$$\epsilon(\partial_t + e_{i\alpha}\partial_\alpha)f_i + \frac{1}{2}\epsilon^2(\partial_t + e_{i\alpha}\partial_\alpha)(\partial_t + e_{i\beta}\partial_\beta)f_i + \mathcal{O}(\epsilon^3),$$

and the RHS,

$$\frac{1}{\tau_f}\left(\epsilon f_i^{(1)} + \epsilon^2 f_i^{(2)}\right) + \epsilon F_i^{(0)} + \mathcal{O}(\epsilon^3),$$

where $F_i = \epsilon F_i^{(0)} = \epsilon\left(1 - \frac{1}{2\tau_f}\right) w_i \left(\frac{\vec{e}_i - \vec{u}}{c_s^2} + \frac{\vec{e}_i \cdot \vec{u}}{c_s^4}\vec{e}_i\right) \cdot \vec{F}_S$.

By matching the terms at different orders of ϵ, one can obtain

$$(\partial_{t_0} + e_{i\alpha}\partial_\alpha) f_i^{eq} = -\frac{1}{\tau_f} f_i^{(1)} + F_i^{(0)} \quad \text{at } \mathcal{O}(\epsilon), \tag{A.7}$$

$$\partial_{t_1} f_i^{eq} + (\partial_{t_0} + e_{i\alpha}\partial_\alpha) f_i^{(1)} + \frac{1}{2}(\partial_{t_0} + e_{i\alpha}\partial_\alpha)(\partial_{t_0} + e_{i\beta}\partial_\beta) f_i^{eq} = -\frac{1}{\tau_f} f_i^{(2)} \quad \text{at } \mathcal{O}(\epsilon^2). \tag{A.8}$$

Substituting (A.7) into (A.8) yields

$$\partial_{t_1} f_i^{eq} + (1 - \frac{1}{2\tau_f})(\partial_{t_0} + e_{i\alpha}\partial_\alpha) f_i^{(1)} + \frac{1}{2}(\partial_{t_0} + e_{i\alpha}\partial_\alpha) F_i^{(0)} = -\frac{1}{\tau_f} f_i^{(2)}. \tag{A.9}$$

Note that one can use the following solvability conditions for $f_i^{(k)}$ $(k = 1, 2, \cdots)$,

$$\sum_i f_i^{(k)} = 0 \quad (k = 1, 2, \cdots), \tag{A.10}$$

$$\sum_i f_i^{(1)} \vec{e}_i = -\frac{1}{2}\vec{F}_S, \quad \sum_i f_i^{(k)} \vec{e}_i = 0 \quad (k = 2, 3, \cdots), \tag{A.11}$$

and the conditions for the equilibrium distributions f_i^{eq}, as given by Eq. (3.22),

$$\begin{aligned} &\sum_i f_i^{eq} = \rho, \quad \sum_i f_i^{eq} e_{i\alpha} = \rho u_\alpha, \quad \sum_i f_i^{eq} e_{i\alpha} e_{i\beta} = \rho u_\alpha u_\beta + p\delta_{\alpha\beta}, \\ &\sum_i f_i^{eq} e_{i\alpha} e_{i\beta} e_{i\gamma} = \rho c_s^2 (\delta_{\alpha\beta} u_\gamma + \delta_{\alpha\gamma} u_\beta + \delta_{\beta\gamma} u_\alpha), \end{aligned}$$

with the equilibrium PDF f_i^{eq} given by Eq. (3.25).

The zeroth and first order moments of Eq. (A.7) lead to

$$\partial_{t_0}\rho + \partial_\alpha(\rho u_\alpha) = 0, \tag{A.12}$$

$$\partial_{t_0}(\rho u_\alpha) + \partial_\beta[(\rho c_s^2 + \phi\mu)\delta_{\alpha\beta} + \rho u_\alpha u_\beta] = F_{S\alpha}. \tag{A.13}$$

It is straightforward to prove that Eq. (A.13) is equivalent to

$$\partial_{t_0}(\rho u_\alpha) + \partial_\beta(\rho c_s^2 \delta_{\alpha\beta} + \rho u_\alpha u_\beta) = -\phi\partial_\alpha\mu. \tag{A.14}$$

The moments of Eq. (A.9) lead to

$$\partial_{t_1}\rho = 0, \tag{A.15}$$

$$\partial_{t_1}(\rho u_\alpha) + \left(1 - \frac{1}{2\tau_f}\right)\partial_\beta \Pi_{\alpha\beta}^{(1)} + \frac{1}{2}\left(1 - \frac{1}{2\tau_f}\right)[\partial_\beta(u_\alpha F_{S\beta}) + \partial_\beta(u_\beta F_{S\alpha})] = 0, \tag{A.16}$$

where the second order tensor $\Pi^{(1)}_{\alpha\beta}$ is defined as

$$\Pi^{(1)}_{\alpha\beta} = \sum_i f_i^{(1)} e_{i\alpha} e_{i\beta}, \tag{A.17}$$

and can be calculated by

$$\begin{aligned}
\Pi^{(1)}_{\alpha\beta} &= \sum_i f_i^{(1)} e_{i\alpha} e_{i\beta} = -\tau_f \sum_i e_{i\alpha} e_{i\beta} [(\partial_{t_0} + e_{i\gamma}\partial_\gamma) f_i^{eq} - F_i^{(0)}] \\
&= -\tau_f \left[\partial_{t_0} \sum_i (f_i^{eq} e_{i\alpha} e_{i\beta}) + \partial_\gamma \sum_i (f_i^{eq} e_{i\alpha} e_{i\beta} e_{i\gamma}) - \sum_i (F_i^{(0)} e_{i\alpha} e_{i\beta}) \right] \\
&= -\tau_f \left\{ \partial_{t_0} \left[\rho u_\alpha u_\beta + (\rho c_s^2 + \phi\mu)\delta_{\alpha\beta} \right] + \partial_\gamma \left[\rho c_s^2 (\delta_{\alpha\beta} u_\gamma + \delta_{\alpha\gamma} u_\beta + \delta_{\beta\gamma} u_\alpha) \right] \right\} \\
&\quad + \left(\tau_f - \frac{1}{2} \right) (u_\alpha F_{S\beta} + u_\beta F_{S\alpha}) \\
&= -\tau_f \left\{ [\partial_{t_0}\rho + \partial_\gamma(\rho u_\gamma)] c_s^2 \delta_{\alpha\beta} + u_\beta \left[\partial_{t_0}(\rho u_\alpha) + \partial_\alpha(\rho c_s^2) \right] \right. \\
&\quad \left. + u_\alpha \left[\partial_{t_0}(\rho u_\beta) + \partial_\beta(\rho c_s^2) \right] + \rho c_s^2 \left(\partial_\alpha u_\beta + \partial_\beta u_\alpha \right) + \partial_{t_0} \left(\phi\mu\delta_{\alpha\beta} \right) \right\} \\
&\quad + \left(\tau_f - \frac{1}{2} \right) (u_\alpha F_{S\beta} + u_\beta F_{S\alpha}) \\
&= -\tau_f \left\{ u_\beta \left[F_{S\alpha} - \partial_\gamma(\rho u_\alpha u_\gamma) - \partial_\alpha(\phi\mu) \right] + u_\alpha \left[F_\beta - \rho u_\gamma \partial_\gamma(u_\beta) - \partial_\beta(\phi\mu) \right] \right. \\
&\quad \left. + \rho c_s^2 \left(\partial_\alpha u_\beta + \partial_\beta u_\alpha \right) + \partial_{t_0} \left(\phi\mu\delta_{\alpha\beta} \right) \right\} + \left(\tau_f - \frac{1}{2} \right) (u_\alpha F_{S\beta} + u_\beta F_{S\alpha}) \\
&= -\frac{1}{2} \left(u_\alpha F_{S\beta} + u_\beta F_{S\alpha} \right) + \tau_f \left[u_\alpha \partial_\beta(\phi\mu) + u_\beta \partial_\alpha(\phi\mu) \right] + \tau_f \partial_\gamma(\rho u_\alpha u_\beta u_\gamma) \\
&\quad - \tau_f \rho c_s^2 \left(\partial_\alpha u_\beta + \partial_\beta u_\alpha \right) - \tau_f \partial_{t_0} \left(\phi\mu \right) \delta_{\alpha\beta}.
\end{aligned}$$

Then, Eq. (A.16) becomes

$$\begin{aligned}
&\partial_{t_1}(\rho u_\alpha) - \partial_\beta \left[\rho c_s^2 \left(\tau_f - \tfrac{1}{2} \right) \left(\partial_\alpha u_\beta + \partial_\beta u_\alpha \right) \right] + \partial_\beta \left[\left(\tau_f - \tfrac{1}{2} \right) \partial_\gamma \left(\rho u_\alpha u_\beta u_\gamma \right) \right] \\
&\quad + \partial_\beta \left\{ \left(\tau_f - \tfrac{1}{2} \right) \left[u_\alpha \partial_\beta(\phi\mu) + u_\beta \partial_\alpha(\phi\mu) \right] \right\} - \partial_\beta \partial_{t_0} \left[\left(\tau_f - \tfrac{1}{2} \right) \phi\mu\delta_{\alpha\beta} \right] = 0.
\end{aligned} \tag{A.18}$$

To obtain the macroscopic governing equations, one simply sums the equations at different orders together. When Eq. (A.15) is multiplied by $\delta_t = \epsilon$ and added to Eq. (A.12), it is easy to find

$$\partial_t \rho + \partial_\alpha(\rho u_\alpha) = 0, \tag{A.19}$$

which is the exactly the continuity equation.

Similarly, when Eq. (A.18) is multiplied by δ_t and added to Eq. (A.13), one can get

$$\begin{aligned}\partial_t(\rho u_\alpha) + \partial_\beta(\rho c_s^2\delta_{\alpha\beta} + \rho u_\alpha u_\beta) - \partial_\beta\left[\rho c_s^2\left(\tau_f - \tfrac{1}{2}\right)\delta_t\left(\partial_\alpha u_\beta + \partial_\beta u_\alpha\right)\right] \\ +\delta_t\partial_\beta\left\{\left(\tau_f - \tfrac{1}{2}\right)\left[u_\alpha\partial_\beta(\phi\mu) + u_\beta\partial_\alpha(\phi\mu)\right]\right\} - \delta_t\partial_\alpha\partial_{t_0}\left[\left(\tau_f - \tfrac{1}{2}\right)\phi\mu\right] \\ +\partial_\beta\left[\left(\tau_f - \tfrac{1}{2}\right)\delta_t\partial_\gamma\left(\rho u_\alpha u_\beta u_\gamma\right)\right] = -\phi\partial_\alpha\mu. \qquad \text{(A.20)}\end{aligned}$$

The term $\rho u_\alpha u_\beta u_\gamma$ in Eq. (A.20) is of order $\mathcal{O}(Ma^3)$, where Ma is the Mach number and given by $Ma = u/c_s$. The term $\delta_t\partial_\alpha\partial_{t_0}\left[\left(\tau_f - \frac{1}{2}\right)\phi\mu\right]$ is multiplied by δ_t, and the chemical potential μ is a small quantity. Therefore, it may be neglected. The similar arguments can be applied for $\delta_t\partial_\beta\left\{\left(\tau_f - \frac{1}{2}\right)\left[u_\alpha\partial_\beta(\phi\mu) + u_\beta\partial_\alpha(\phi\mu)\right]\right\}$ and besides $u_\alpha\partial_\beta(\phi\mu) + u_\beta\partial_\alpha(\phi\mu)$ is of order $\mathcal{O}(Ma)$ as compared with $\phi\partial_\alpha\mu$ on the RHS. Hence, they may all be neglected and Eq. (A.20) approximately becomes

$$\partial_t(\rho u_\alpha) + \partial_\beta(\rho c_s^2\delta_{\alpha\beta} + \rho u_\alpha u_\beta) - \partial_\beta\left[\rho c_s^2\left(\tau_f - \frac{1}{2}\right)\delta_t\left(\partial_\alpha u_\beta + \partial_\beta u_\alpha\right)\right] = -\phi\partial_\alpha\mu. \tag{A.21}$$

If the dynamic viscosity is expressed as $\eta = \rho c_s^2\left(\tau_f - \frac{1}{2}\right)\delta_t$, Eq. (A.21) becomes

$$\partial_t(\rho u_\alpha) + \partial_\beta(\rho c_s^2\delta_{\alpha\beta} + \rho u_\alpha u_\beta) - \partial_\beta\left[\eta\left(\partial_\alpha u_\beta + \partial_\beta u_\alpha\right)\right] = -\phi\partial_\alpha\mu. \tag{A.22}$$

This is just the momentum equation.

Next, the LB equation for the PDF g_i used for the order parameter is studied. After the expansion of Eq. (A.2) and the match of terms at different orders, one can obtain

$$(\partial_{t_0} + e_{i\alpha}\partial_\alpha)g_i^{eq} = -\frac{1}{\tau_g}g_i^{(1)} \quad \text{at } \mathcal{O}(\epsilon), \tag{A.23}$$

$$\partial_{t_1}g_i^{eq} - \left(\tau_g - \frac{1}{2}\right)(\partial_{t_0} + e_{i\alpha}\partial_\alpha)(\partial_{t_0} + e_{i\beta}\partial_\beta)g_i^{eq} = -\frac{1}{\tau_f}g_i^{(2)} \quad \text{at } \mathcal{O}(\epsilon^2). \tag{A.24}$$

The zeroth moments of Eqs. (A.23) and (A.24) are

$$\partial_{t_0}\phi + \partial_\alpha(\phi u_\alpha) = 0, \tag{A.25}$$

$$\begin{aligned}\partial_{t_1}\phi - \left(\tau_g - \frac{1}{2}\right)\left[\partial_{t_0}\partial_{t_0}\phi + \partial_\alpha\partial_{t_0}\left(\phi u_\alpha\right)\right] \\ - \left(\tau_g - \frac{1}{2}\right)\left[\partial_\beta\partial_{t_0}\left(\phi u_\beta\right) + \partial_\alpha\partial_\beta\left(\Gamma\mu\delta_{\alpha\beta} + \phi u_\alpha u_\beta\right)\right] = 0 \qquad \text{(A.26)}\end{aligned}$$

where the following solvability conditions for $g_i^{(k)}$ $(k = 1, 2, \cdots)$,

$$\sum_i g_i^{(k)} = 0 \quad (k = 1, 2, \cdots), \tag{A.27}$$

$$\sum_i g_i^{(k)} e_{i\alpha} = 0 \quad (k = 1, 2, \cdots), \tag{A.28}$$

and the conditions for g_i^{eq}, as given by Eq. (3.23), i.e.

$$\sum_i g_i^{eq} = \phi, \quad \sum_i g_i^{eq} e_{i\alpha} = \phi u_\alpha, \quad \sum_i g_i^{eq} e_{i\alpha} e_{i\beta} = \phi u_\alpha u_\beta + \Gamma \mu \delta_{\alpha\beta}, \tag{A.29}$$

have been used. From Eq. (A.25), one can get

$$\partial_{t_0} \partial_{t_0} \phi + \partial_\alpha \partial_{t_0} (\phi u_\alpha) = \partial_{t_0} \left[\partial_{t_0} \phi + \partial_\alpha (\phi u_\alpha) \right] = 0. \tag{A.30}$$

Then, Eq. (A.26) is simplified as

$$\partial_{t_1} \phi = \left(\tau_g - \frac{1}{2} \right) \Gamma \partial_{\alpha\alpha} \mu + \left(\tau_g - \frac{1}{2} \right) \partial_\beta \left[\partial_{t_0} (\phi u_\beta) + \partial_\alpha (\phi u_\alpha u_\beta) \right]. \tag{A.31}$$

By using Eqs. (A.12), (A.14) and (A.25),one can get

$$\partial_{t_0} (\phi u_\beta) + \partial_\alpha (\phi u_\alpha u_\beta) = \frac{\phi}{\rho} \left[-\partial_\beta (\rho c_s^2) - \phi \partial_\beta \mu \right], \tag{A.32}$$

which are the two terms after the differential operator ∂_β in Eq. (A.31). Assuming that these high order derivatives can be neglected, one can simply Eq. (A.31) as

$$\partial_{t_1} \phi = \left(\tau_g - \frac{1}{2} \right) \Gamma \partial_{\alpha\alpha} \mu. \tag{A.33}$$

When Eq. (A.33) is multiplied by δ_t and added to Eq. (A.25), one gets

$$\partial_t \phi + \partial_\alpha (\phi u_\alpha) = \left(\tau_g - \frac{1}{2} \right) \Gamma \delta_t \partial_{\alpha\alpha} \mu. \tag{A.34}$$

If the mobility is expressed as $M = \left(\tau_g - \frac{1}{2} \right) \Gamma \delta_t$, Eq. (A.34) becomes

$$\partial_t \phi + \partial_\alpha (\phi u_\alpha) = M \partial_{\alpha\alpha} \mu. \tag{A.35}$$

This is the approximate Cahn-Hilliard equation for order parameter ϕ.

To summarize, the continuity equation, the momentum equation and the Cahn-Hilliard equation have been obtained as given by Eqs. (A.19), (A.22) and (A.35), respectively.

Appendix B

Analysis on the equilibrium properties

The free energy functional is chosen as Eq. (7.5). The excess free energy per unit interface area can be defined by

$$w(\phi,\psi) = f(\phi,\psi) - f(\phi_b,\psi_b) - \frac{\partial f(\phi_b,\psi_b)}{\partial \phi_b}(\phi-\phi_b) - \frac{\partial f(\phi_b,\psi_b)}{\partial \psi_b}(\psi-\psi_b), \quad \text{(B.1)}$$

which satisfies the Euler-Lagrange minimization equations:

$$\frac{\partial w}{\partial \phi} - \frac{\mathrm{d}}{\mathrm{d}x}\left(\frac{\partial w}{\partial \nabla\phi}\right) = 0, \quad \text{(B.2)}$$

$$\frac{\partial w}{\partial \psi} - \frac{\mathrm{d}}{\mathrm{d}x}\left(\frac{\partial w}{\partial \nabla\psi}\right) = 0. \quad \text{(B.3)}$$

Defining $\eta(x) = \phi(x)/\phi_b$, and with Eqs. (B.1), (B.2) and (B.3), we obtain:

$$\begin{aligned} w \;=\; & k_B T\left[\psi\ln\left(\frac{\psi}{\psi_b}\right) + (1-\psi)\ln\left(\frac{1-\psi}{1-\psi_b}\right)\right] - \frac{C}{2}(\psi-\psi_b)^2 \\ & + \frac{W}{2}\phi_b^2(\psi-\psi_b)(\eta^2-1) + \frac{B}{4}\phi_b^4(\eta^2-1)^2 + \frac{1}{2}\left(\kappa - D\psi\right)\phi_b^2\eta_x^2, \end{aligned} \quad \text{(B.4)}$$

$$B\phi_b^3(\eta^3-\eta) + W\phi_b\eta(\psi-\psi_b) = (\kappa - D\psi)\phi_b\eta_{xx} - D\phi_b\eta_x\psi_x, \quad \text{(B.5)}$$

$$k_B T\left[\psi\ln\left(\frac{\psi}{\psi_b}\right) - \ln\left(\frac{1-\psi}{1-\psi_b}\right)\right] - C(\psi-\psi_b) + \frac{W}{2}\phi_b^2(\eta^2-1) - \frac{D}{2}\phi_b^2\eta_x^2 = 0. \quad \text{(B.6)}$$

When the surfactant excess is not quite large at the interface, we can rewrite Eq. (B.6) using a linear approximation for the logarithmic part as the following form:

$$\chi(\psi-\psi_b) + \frac{W}{2}\phi_b^2(\eta^2-1) - \frac{D}{2}\phi_b^2\eta_x^2 \approx 0, \quad \text{(B.7)}$$

where $\chi = k_B T\left(\frac{1}{\psi_b} + \frac{1}{1-\psi_b}\right) - C$.

From Eq. (B.7), we obtain

$$\begin{aligned}
\psi - \psi_b &= \frac{\phi_b^2}{2\chi}[W(1-\eta^2) + D\eta_x^2], && \text{(B.8)}\\
\psi_x &= \frac{1}{\chi}\phi_b^2\eta_x(D\eta_{xx} - W\eta). && \text{(B.9)}
\end{aligned}$$

Substituting Eqs. (B.8) and (B.9) into Eq. (B.5), we have

$$\begin{aligned}
&B\phi_b^3(\eta^3-\eta) + \frac{W\phi_b^3}{2\chi}\eta[W(1-\eta^2)+D\eta_x^2] = -\frac{D\phi_b^3}{\chi}\eta_x^2(D\eta_{xx} - W\eta)\\
&+\left\{\kappa - D\psi_b - \frac{\phi_b^2 D}{2\chi}[W(1-\eta^2)+D\eta_x^2]\right\}\phi_b\eta_{xx}. \qquad \text{(B.10)}
\end{aligned}$$

The interfacial profile $\eta(x)$ can be obtained by the solution of Eq. (B.10). Unfortunately, Eq. (B.10) cannot be analytically solved. To obtain an expression for the interfacial tension σ, we omit all the high-order terms in Eq. (B.10), so that the equation is simplified as:

$$B\phi_b^3(\eta^3-\eta) + \frac{W\phi_b^3}{2\chi}W\eta(1-\eta^2) = \left(\kappa - D\psi_b - \frac{1}{2\chi}DW\phi_b^2\right)\phi_b\eta_{xx}. \qquad \text{(B.11)}$$

Therefore, we can obtain

$$\eta(x) = \tanh(x/\xi), \qquad \text{(B.12)}$$

where

$$\xi^2 = \frac{2\left[\kappa - D\left(\psi_b + \frac{\phi_b^2 W}{2\chi}\right)\right]}{\phi_b^2\left(B - \frac{W^2}{2\chi}\right)}. \qquad \text{(B.13)}$$

In our free energy model given by Eq. (7.5), χ can be approximated by $\chi \approx k_BT/\psi_b$ due to C is up to $\mathcal{O}(k_BT)$ and $\psi_b \ll 1$. Therefore, Eq. (B.13) can be approximated by:

$$\xi^2 = \frac{2\kappa}{B\phi_b^2}, \qquad \text{(B.14)}$$

which accords with our assumption that the solvent composition profile is independent of the surfactant loading in equilibrium. When $\chi = C$, the free energy model proposed by Theissen and Gompper [155] can be recovered with the interface thickness defined by Eq. (7.4). By integrating the excess free energy per unit interface area i.e. Eq. (B.4) in the whole domain, we can obtain the interfacial tension i.e. Eq. (7.3) for $\chi = C$.

Appendix C

Equilibrium distributions

Following the constraints of Eqs.(7.31) and (7.35), the equilibrium distributions, which are assumed to be a power series in the local velocity, can be written as:

$$\begin{aligned} f_i^{eq} &= F_i + w_i \rho \left[\frac{\vec{e}_i \cdot \vec{u}}{c_s^2} + \frac{(\vec{e}_i \cdot \vec{u})^2}{2c_s^4} - \frac{\vec{u} \cdot \vec{u}}{2c_s^2} \right], \\ g_i^{eq} &= G_i + w_i \phi \left[\frac{\vec{e}_i \cdot \vec{u}}{c_s^2} + \frac{(\vec{e}_i \cdot \vec{u})^2}{2c_s^4} - \frac{\vec{u} \cdot \vec{u}}{2c_s^2} \right], \\ h_i^{eq} &= H_i + w_i \psi \left[\frac{\vec{e}_i \cdot \vec{u}}{c_s^2} + \frac{(\vec{e}_i \cdot \vec{u})^2}{2c_s^4} - \frac{\vec{u} \cdot \vec{u}}{2c_s^2} \right]. \end{aligned} \tag{C.1}$$

for $i = 1, ..., 8$, where

$$F_i = \begin{cases} \vec{e}_i^{\mathrm{T}} \mathbf{P} \vec{e}_i / 2c^4 - (P_{xx} + P_{yy})/12c^2 & i = 1 - 4, \\ \vec{e}_i^{\mathrm{T}} \mathbf{P} \vec{e}_i / 8c^4 - (P_{xx} + P_{yy})/6c^2 & i = 5 - 8. \end{cases} \tag{C.2}$$

and

$$G_i = \frac{1}{c_s^2} w_i \Gamma_\phi \mu_\phi, \quad H_i = \frac{1}{c_s^2} w_i \Gamma_\psi \mu_\psi. \tag{C.3}$$

The stationary values i.e. $i = 0$ are chosen to conserve the mass of each species,

$$f_0^{eq} = \rho - \sum_{i=1}^{8} f_i^{eq}, \quad g_0^{eq} = \phi - \sum_{i=1}^{8} g_i^{eq}, \quad h_0^{eq} = \psi - \sum_{i=1}^{8} h_i^{eq}. \tag{C.4}$$

Appendix D

Newton method for equilibrium surfactant concentration in a closed system

We use a two-step Newton's method to solve the equilibrium surfactant concentration in a closed system with a given total surfactant concentration m_s. In equilibrium, the surfactant concentration follows Eq. (7.27), which can be rewritten as

$$\psi(x) = \frac{1}{1 + y\mathrm{e}^{-\tilde{C}\psi(x)}\vartheta(x)}, \tag{D.1}$$

where $\vartheta(x) = \exp\left\{\frac{1}{k_B T}\left[\frac{W}{2}\phi^2 - \frac{\kappa}{2}(\partial_x\phi)^2 - E\phi\right]\right\}$, $y = \mathrm{e}^{-\frac{1}{k_B T}\mu_\psi}$, and $\tilde{C} = \frac{C}{k_B T}$. Meanwhile, the surfactant concentration must satisfy the constraint of Eq. (7.45), which can be expressed in a discrete form:

$$\sum_i \psi(x_i)\delta_x = m_s. \tag{D.2}$$

We introduce the notations: $\psi_i = \psi(x_i)$, $\vartheta_i = \vartheta(x_i)$, and directly substitute Eq. (D.1) into Eq. (D.2). Therefore, Eqs. (D.1) and (D.2) become

$$\psi_i = \frac{1}{1 + y\mathrm{e}^{-\tilde{C}\psi_i}\vartheta_i}, \tag{D.3}$$

$$\sum_i \frac{1}{1 + y\mathrm{e}^{-\tilde{C}\psi_i}\vartheta_i}\delta_x = m_s. \tag{D.4}$$

In the above equations, ψ_i and y are unknowns. We can use the following algorithm to obtain the unknowns.

1. Set $m = 0$, and give y an initial guess y^0.
2. Set $y = y^m$, and use the Newton-Raphson method to iteratively solve Eq. (D.3) until a converged solution ψ_i^m is obtained at all the lattice points.

3. Set $\psi_i = \psi_i^m$ for all the lattice points, and then use the Newton-Raphson method to iteratively solve Eq. (D.4) until a converged solution y^{m+1} is obtained. Update $m = m + 1$.

4. Repeat the solution steps (2) and (3) until the solutions satisfy the given conditions.

References

[1] N. Bontoux, A. Pépin, Y. Chen, A. Ajdari, H. A. Stone, Experimental characterization of hydrodynamic dispersion in shallow microchannels, Lab Chip 6 (2006) 930–935.

[2] J. D. Tice, H. Song, A. D. Lyon, R. F. Ismagilov, Formation of droplets and mixing in multiphase microfluidics at low values of the Reynolds and the capillary numbers, Langmuir 19 (2003) 9127–9133.

[3] G. F. Christopher, S. L. Anna, Microfluidic methods for generating continuous droplet streams, J. Phys. D-Appl. Phys. 40 (2007) R319–R336.

[4] B. Zheng, L. S. Roach, R. F. Ismagilov, Screening of protein crystallization conditions on a microfluidic chip using nanoliter-size droplets, J. Am. Chem. Soc. 125 (2003) 11170–11171.

[5] H. Song, D. L. Chen, R. F. Ismagilov, Reactions in droplets in microfluidic channels, Angew. Chem. Int. Ed. 45 (2006) 7336–7356.

[6] S. Sugiura, M. Nakajima, H. Itou, M. Seki, Synthesis of polymeric microspheres with narrow size distributions employing microchannel emulsification, Macromol. Rapid Commun. 22 (2001) 773–778.

[7] D. Dendukuri, K. Tsoi, T. A. Hatton, P. S. Doyle, Controlled synthesis of nonspherical microparticles using microfluidics, Langmuir 21 (2005) 2113–2116.

[8] V. Srinivasan, V. K. Pamula, R. B. Fair, Droplet-based microfluidic lab-on-a-chip for glucose detection, Anal. Chim. Acta 507 (2004) 145 – 150.

[9] J. Khandurina, T. E. McKnight, S. C. Jacobson, L. C. Waters, R. S. Foote, J. M. Ramsey, Integrated system for rapid PCR-based DNA analysis in microfluidic devices, Anal. Chem. 72 (2000) 2995–3000.

[10] M. Yasuno, S. Sugiura, S. Iwamoto, M. Nakajima, A. Shono, K. Satoh, Monodispersed microbubble formation using microchannel technique, AIChE J. 50 (2004) 3227–3233.

[11] S. Sugiura, M. Nakajima, M. Seki, Prediction of droplet diameter for microchannel emulsification: Prediction model for complicated microchannel geometries, Ind. Eng. Chem. Res. 43 (2004) 8233–8238.

[12] S. L. Anna, N. Bontoux, H. A. Stone, Formation of dispersions using “flow focusing” in microchannels, Appl. Phys. Lett. 82 (2003) 364–366.

[13] T. Cubaud, M. Tatineni, X. Zhong, C.-M. Ho, Bubble dispenser in microfluidic devices, Phys. Rev. E 72 (2005) 037302.

[14] P. Garstecki, H. A. Stone, G. M. Whitesides, Mechanism for flow-rate controlled breakup in confined geometries: A route to monodisperse emulsions, Phys. Rev. Lett. 94 (2005) 164501.

[15] J. Tan, J. Xu, S. Li, G. Luo, Drop dispenser in a cross-junction microfluidic device: Scaling and mechanism of break-up, Chem. Eng. J. 136 (2008) 306 – 311.

[16] T. Fu, Y. Ma, D. Funfschilling, H. Z. Li, Bubble formation and breakup mechanism in a microfluidic flow-focusing device, Chem. Eng. Sci. 64 (10) (2009) 2392 – 2400.

[17] T. Thorsen, R. W. Roberts, F. H. Arnold, S. R. Quake, Dynamic pattern formation in a vesicle-generating microfluidic device, Phys. Rev. Lett. 86 (2001) 4163–4166.

[18] T. Nisisako, T. Torii, T. Higuchi, Droplet formation in a microchannel network, Lab Chip 2 (2002) 24–26.

[19] P. Guillot, A. Colin, Stability of parallel flows in a microchannel after a T junction, Phys. Rev. E 72 (2005) 066301.

[20] P. Garstecki, M. J. Fuerstman, H. A. Stone, G. M. Whitesides, Formation of droplets and bubbles in a microfluidic T-junction–scaling and mechanism of break-up, Lab Chip 6 (2006) 437–446.

[21] S. van der Graaf, T. Nisisako, C. G. P. H. Schroën, R. G. M. van der Sman, R. M. Boom, Lattice Boltzmann simulations of droplet formation in a T-shaped microchannel, Langmuir 22 (2006) 4144–4152.

[22] M. D. Menech, P. Garstecki, F. Jousse, H. A. Stone, Transition from squeezing to dripping in a microfluidic T-shaped junction, J. Fluid Mech. 595 (2008) 141–161.

[23] G. F. Christopher, N. N. Noharuddin, J. A. Taylor, S. L. Anna, Experimental observations of the squeezing-to-dripping transition in T-shaped microfluidic junctions, Phys. Rev. E 78 (2008) 036317.

[24] P. B. Umbanhowar, V. Prasad, D. A. Weitz, Monodisperse emulsion generation via drop break off in a coflowing stream, Langmuir 16 (2000) 347–351.

[25] J. Hua, B. Zhang, J. Lou, Numerical simulation of microdroplet formation in coflowing immiscible liquids, AIChE J. 53 (2007) 2534–2548.

[26] D. Juric, G. Tryggvason, A front-tracking method for dendritic solidification, J. Comput. Phys. 123 (1) (1996) 127–148.

[27] R. Scardovelli, S. Zalesk, Direct numerical simulation of free-surface and interfacial flow, Annu. Rev. Fluid Mech. 31 (1999) 567–603.

[28] X. Yang, A. J. James, J. Lowengrub, X. Zheng, V. Cristini, An adaptive coupled level-set/volume-of-fluid interface capturing method for unstructured triangular grids, J. Comput. Phys. 217 (2) (2006) 364–394.

[29] H. Stone, A. Stroock, A. Ajdari, Engineering flows in small devices microfluidics toward a lab-on-a-chip, Annu. Rev. Fluid Mech. 36 (2004) 381–411.

[30] S. L. Anna, H. C. Mayer, Microscale tipstreaming in a microfluidic flow focusing device, Phys. Fluids 18 (2006) 121512.

[31] J. H. Xu, S. W. Li, J. Tan, Y. J. Wang, G. S. Luo, Controllable preparation of monodisperse o/w and w/o emulsions in the same microfluidic device, Langmuir 22 (19) (2006) 7943–7946.

[32] H. A. Stone, L. G. Leal, The effects of surfactants on drop deformation and breakup, J. Fluid Mech. 220 (1990) 161–186.

[33] H. Diamant, D. Andelman, Kinetics of surfactant adsorption at fluid-fluid interfaces, J. Phys. Chem. 100 (1996) 13732.

[34] H.-Y. Chen, D. Jasnow, J. Viñals, Interface and contact line motion in a two phase fluid under shear flow, Phys. Rev. Lett. 85 (2000) 1686–1689.

[35] M. R. Swift, E. Orlandini, W. R. Osborn, J. M. Yeomans, Lattice Boltzmann simulations of liquid-gas and binary fluid systems, Phys. Rev. E 54 (5) (1996) 5041–5052.

[36] C. M. Pooley, H. Kusumaatmaja, J. M. Yeomans, Contact line dynamics in binary lattice Boltzmann simulations, Phys. Rev. E 78 (5) (2008) 056709.

[37] L. Yobas, S. Martens, W.-L. Ong, N. Ranganathan, High-performance flow-focusing geometry for spontaneous generation of monodispersed droplets, Lab Chip 6 (2006) 1073–1079.

[38] I. Kobayashi, K. Uemura, M. Nakajima, Formulation of monodisperse emulsions using submicron-channel arrays, Colloids Surf. A 296 (1-3) (2007) 285–289.

[39] B. Zheng, J. D. Tice, L. S. Roach, R. F. Ismagilov, A droplet-based, composite PDMS/glass capillary microfluidic system for evaluating protein crystallization conditions by microbatch and vapor-diffusion methods with on-chip x-ray diffraction, Angew. Chem. Int. Ed. 43 (2004) 2508–2511.

[40] B. Zheng, J. D. Tice, R. F. Ismagilov, Formation of droplets of alternating composition in microfluidic channels and applications to indexing of concentrations in droplet-based assays, Anal. Chem. 76 (2004) 4977–4982.

[41] V. Cristini, Y.-C. Tan, Theory and numerical simulation of droplet dynamics in complex flows–a review, Lab Chip 4 (2004) 257–264.

[42] C. Cramer, P. Fischer, E. J. Windhab, Drop formation in a co-flowing ambient fluid, Chem. Eng. Sci. 59 (15) (2004) 3045–3058.

[43] M. Zagnoni, J. Anderson, J. M. Cooper, Hysteresis in multiphase microfluidics at a T-junction, Langmuir 26 (12) (2010) 9416–9422.

[44] T. M. Squires, S. R. Quake, Microfluidics: Fluid physics at the nanoliter scale, Rev. Mod. Phys. 77 (3) (2005) 977–1026.

[45] T. Cubaud, C.-M. Ho, Transport of bubbles in square microchannels, Phys. Fluids 16 (2004) 4575–4585.

[46] T. Nisisako, T. Torii, T. Higuchi, Novel microreactors for functional polymer beads, Chem. Eng. J. 101 (2004) 23–29.

[47] J. H. Xu, S. W. Li, G. G. Chen, G. S. Luo, Formation of monodisperse microbubbles in a microfluidic device, AIChE J. 52 (2006) 2254–2259.

[48] S. van der Graaf, M. L. J. Steegmans, R. G. M. van der Sman, C. G. P. H. Schroën, R. M. Boom, Droplet formation in a T-shaped microchannel junction: A model system for membrane emulsification, Colloids Surf. A 266 (2005) 106–116.

[49] Y. Zhao, G. Chen, Q. Yuan, Liquid-liquid two-phase flow patterns in a rectangular microchannel, AIChE Journal 52 (12) (2006) 4052–4060.

[50] Z. Yu, O. Hemminger, L.-S. Fan, Experiment and lattice Boltzmann simulation of two-phase gas-liquid flows in microchannels, Chem. Eng. Sci. 62 (2007) 7172 – 7183.

[51] A. S. Utada, E. Lorenceau, D. R. Link, P. D. Kaplan, H. A. Stone, D. A. Weitz, Monodisperse double emulsions generated from a microcapillary device, Science 308 (5721) (2005) 537–541.

[52] J. Tan, S. Li, K. Wang, G. Luo, Gas-liquid flow in T-junction microfluidic devices with a new perpendicular rupturing flow route, Chem. Eng. J. 146 (3) (2009) 428 – 433.

[53] J. Xu, S. Li, J. Tan, G. Luo, Correlations of droplet formation in T-junction microfluidic devices: from squeezing to dripping, Microfluid. Nanofluid. 5 (2008) 711–717.

[54] J. H. Xu, G. S. Luo, S. W. Li, G. G. Chen, Shear force induced monodisperse droplet formation in a microfluidic device by controlling wetting properties, Lab Chip 6 (2006) 131–136.

[55] J. H. Xu, S. W. Li, J. Tan, Y. J. Wang, G. S. Luo, Preparation of highly monodisperse droplet in a T-junction microfluidic device, AIChE J. 52 (9) (2006) 3005–3010.

[56] B. Dollet, W. van Hoeve, J.-P. Raven, P. Marmottant, M. Versluis, Role of the channel geometry on the bubble pinch-off in flow-focusing devices, Phys. Rev. Lett. 100 (3) (2008) 034504.

[57] T. Fu, D. Funfschilling, Y. Ma, H. Z. Li, Scaling the formation of slug bubbles in microfluidic flow-focusing devices, Microfluid. Nanofluid. 8 (2010) 467–475.

[58] C. Zhou, P. Yue, J. J. Feng, Formation of simple and compound drops in microfluidic devices, Phys. Fluids 18 (2006) 092105.

[59] A. R. Abate, A. Poitzsch, Y. Hwang, J. Lee, J. Czerwinska, D. A. Weitz, Impact of inlet channel geometry on microfluidic drop formation, Phys. Rev. E 80 (2) (2009) 026310.

[60] R. Xiong, M. Bai, J. N. Chung, Formation of bubbles in a simple co-flowing micro-channel, J. Micromech. Microeng. 17 (5) (2007) 1002–1011.

[61] M. J. Jensen, H. A. Stone, H. Bruus, A numerical study of two-phase Stokes flow in an axisymmetric flow-focusing device, Phys. Fluids 18 (2006) 077103.

[62] S. van der Graaf, C. G. P. H. Schron, R. G. M. van der Sman, R. M. Boom, Influence of dynamic interfacial tension on droplet formation during membrane emulsification, J. Colloid Interface Sci. 277 (2) (2004) 456 – 463.

[63] K. Wang, Y. C. Lu, J. H. Xu, G. S. Luo, Determination of dynamic interfacial tension and its effect on droplet formation in the T-shaped microdispersion process, Langmuir 25 (4) (2009) 2153–2158.

[64] M. L. J. Steegmans, A. Warmerdam, K. G. P. H. Schroën, R. M. Boom, Dynamic interfacial tension measurements with microfluidic Y-junctions, Langmuir 25 (17) (2009) 9751–9758.

[65] S. Quan, D. P. Schmidt, A moving mesh interface tracking method for 3D incompressible two-phase flows, J. Comput. Phys. 221 (2) (2007) 761–780.

[66] G. Tryggvason, B. Bunner, A. Esmaeeli, D. Juric, N. Al-Rawahi, W. Tauber, J. Han, S. Nas, Y.-J. Jan, A front-tracking method for the computations of multiphase flow, J. Comput. Phys. 169 (2) (2001) 708–759.

[67] S. Osher, R. P. Fedkiw, Level Set Methods and Dynamic Implicit Surfaces, Springer, 2003.

[68] D. M. Anderson, G. B. McFadden, Diffuse-interface methods in fluid mechanics, Annu. Rev. Fluid Mech. 30 (1998) 139–165.

[69] C. Hirt, B. Nichols, Volume of fluid (VOF) method for the dynamics of free boundaries, J. Comput. Phys. 39 (1981) 201–225.

[70] D. Gueyffier, J. Li, A. Nadim, R. Scardovelli, S. Zaleski, Volume-of-fluid interface tracking with smoothed surface stress methods for three-dimensional flows, J. Comput. Phys. 152 (2) (1999) 423–456.

[71] J. U. Brackbill, D. B. Kothe, C. Zemach, A continuum method for modeling surface tension, J. Comput. Phys. 100 (2) (1992) 335–354.

[72] M. Renardy, Y. Renardy, J. Li, Numerical simulation of moving contact line problems using a volume-of-fluid method, J. Comput. Phys. 171 (1) (2001) 243–263.

[73] Y. Y. Renardy, M. Renardy, V. Cristini, A new volume-of-fluid formulation for surfactants and simulations of drop deformation under shear at a low viscosity ratio, Eur. J. Mech. B Fluid 21 (1) (2002) 49–59.

[74] A. J. James, J. Lowengrub, A surfactant-conserving volume-of-fluid method for interfacial flows with insoluble surfactant, J. Comput. Phys. 201 (2) (2004) 685 – 722.

[75] H. A. Stone, A simple derivation of the time-dependent convective-diffusion equation for surfactant transport along a deforming interface, Phys. Fluids A 2 (1990) 111–112.

[76] S. Osher, J. A. Sethian, Fronts propagating with curvature-dependent speed: Algorithms based on hamilton-jacobi formulations, J. Comput. Phys. 79 (1) (1988) 12–49.

[77] M. Sussman, E. Fatemi, An efficient, interface-preserving level set redistancing algorithm and its application to interfacial incompressible fluid flow, SIAM J. Sci. Comput. 20 (4) (1999) 1165–1191.

[78] P. D. M Spelt, A level-set approach for simulations of flows with multiple moving contact lines with hysteresis, J. Comput. Phys. 207 (2) (2005) 389–404.

[79] P. D. M. Spelt, Shear flow past two-dimensional droplets pinned or moving on an adhering channel wall at moderate Reynolds numbers: A numerical study, J. Fluid Mech. 561 (2006) 439–463.

[80] J.-J. Xu, Z. Li, J. Lowengrub, H. Zhao, A level-set method for interfacial flows with surfactant, J. Comput. Phys. 212 (2) (2006) 590 – 616.

[81] J. W. Cahn, J. E. Hilliard, Free energy of a nonuniform system. I. Interfacial free energy, J. Chem. Phys. 28 (2) (1958) 258–267.

[82] C. Liu, J. Shen, A phase field model for the mixture of two incompressible fluids and its approximation by a fourier-spectral method, Physica D 179 (3-4) (2003) 211–228.

[83] D. Enright, S. Marschner, R. Fedkiw, Animation and rendering of complex water surfaces, ACM Trans. Graph. 21 (3) (2002) 736–744.

[84] D. Enright, F. Losasso, R. Fedkiw, A fast and accurate semi-lagrangian particle level set method, Comput. Struct. 83 (6-7) (2005) 479–490.

[85] P. G. de Gennes, Wetting: Statics and dynamics, Rev. Mod. Phys. 57 (3) (1985) 827–863.

[86] D. Jacqmin, Calculation of two-phase Navier-Stokes flows using phase-field modeling, J. Comput. Phys. 155 (1999) 96–127.

[87] D. Jacqmin, Contact-line dynamics of a diffuse fluid interface, J. Fluid Mech. 402 (2000) 57–88.

[88] V. V. Khatavkar, P. D. Anderson, H. E. H. Meijer, Capillary spreading of a droplet in the partially wetting regime using a diffuse-interface model, J. Fluid Mech. 572 (2007) 367–387.

[89] V. V. Khatavkar, P. D. Anderson, P. C. Duineveld, H. E. H. Meijer, Diffuse-interface modelling of droplet impact, J. Fluid Mech. 581 (2007) 97–127.

[90] R. van der Sman, S. van der Graaf, Diffuse interface model of surfactant adsorption onto flat and droplet interfaces, Rheol. Acta 46 (2006) 3–11.

[91] A. F. H. Ward, L. Tordai, Time-dependence of boundary tensions of solutions I. The role of diffusion in time-effects, J. Chem. Phys. 14 (7) (1946) 453–461.

[92] M. Steegmans, C. Schron, R. Boom, Generalised insights in droplet formation at T-junctions through statistical analysis, Chem. Eng. Sci. 64 (13) (2009) 3042 – 3050.

[93] C. K. Aidun, J. R. Clausen, Lattice-Boltzmann method for complex flows, Annu. Rev. Fluid Mech. 42 (1) (2010) 439–472.

[94] D. A. Wolf-Gladrow, Lattice-Gas Cellular Automata and Lattice Boltzmann Models, Berlin: Springer Verlag, 2000.

[95] S. Succi, The Lattice Boltzmann Equation for Fluid Dynamics and Beyond, Oxford: Oxford University Press, 2001.

[96] Y. H. Qian, D. D'Humières, P. Lallemand, Lattice BGK models for Navier-Stokes equation, Europhys. Lett. 17 (1992) 479–484.

[97] S. Chen, G. D. Doolen, Lattice Boltzmann method for fluid flows, Annu. Rev. Fluid Mech. 30 (1) (1998) 329–364.

[98] A. K. Gunstensen, D. H. Rothman, S. Zaleski, G. Zanetti, Lattice Boltzmann model of immiscible fluids, Phys. Rev. A 43 (8) (1991) 4320–4327.

[99] X. Shan, H. Chen, Lattice Boltzmann model for simulating flows with multiple phases and components, Phys. Rev. E 47 (3) (1993) 1815–1819.

[100] X. He, S. Chen, R. Zhang, A lattice Boltzmann scheme for incompressible multiphase flow and its application in simulation of Rayleigh-Taylor instability, J. Comput. Phys. 152 (2) (1999) 642–663.

[101] M. R. S. E. Orlandini, J. M. Yeomans, A lattice Boltzmann model of binary-fluid mixtures, Europhysics Letters 32 (6) (1995) 463.

[102] R. R. Nourgaliev, T. N. Dinh, T. G. Theofanous, D. Joseph, The lattice Boltzmann equation method: Theoretical interpretation, numerics and implications, Int. J. Multiph. Flow 29 (1) (2003) 117–169.

[103] G. Rannou, Lattice Boltzmann method and immiscible two-phase flow, Master's thesis, Georgia Institute of Technology (2008).

[104] J. W. Cahn, Critical point wetting, J. Chem. Phys. 66 (1977) 3667–3672.

[105] C. Huh, L. Scriven, Hydrodynamic model of steady movement of a solid/liquid/fluid contact line, J. Colloid Interface Sci. 35 (1) (1971) 85 – 101.

[106] V. E. Badalassi, H. D. Ceniceros, S. Banerjee, Computation of multiphase systems with phase field models, J. Comput. Phys. 190 (2) (2003) 371–397.

[107] V. V. Khatavkar, P. D. Anderson, P. C. Duineveld, H. H. E. Meijer, Diffuse interface modeling of droplet impact on a pre-patterned solid surface, Macromol. Rapid Commun. 26 (2005) 298–303.

[108] P. Yue, J. J. Feng, C. Liu, J. Shen, Diffuse-interface simulations of drop coalescence and retraction in viscoelastic fluids, J. Non-Newton. Fluid Mech. 129 (3) (2005) 163 – 176.

[109] H. Ding, P. D. M. Spelt, Inertial effects in droplet spreading: A comparison between diffuse-interface and level-set simulations, J. Fluid Mech. 576 (2007) 287–296.

[110] W. Yu, C. Zhou, Coalescence of droplets in viscoelastic matrix with diffuse interface under simple shear flow, J. Polym. Sci. Part B: Polym. Phys. 45 (14) (2007) 1856–1869.

[111] V. M. Kendon, M. E. Cates, I. Pagonabarraga, J. C. Desplat, P. Bladon, Inertial effects in three-dimensional spinodal. decomposition of a symmetric binary fluid mixture: A lattice Boltzmann study, J. Fluid Mech. 440 (2001) 147–203.

[112] J. S. Rowlinson, B. Widom, Molecular Theory of Capillarity, London: Clarendon Press, 1989.

[113] D. Jamet, D. Torres, J. U. Brackbill, On the theory and computation of surface tension: The elimination of parasitic currents through energy conservation in the second-gradient method, J. Comput. Phys. 182 (1) (2002) 262–276.

[114] Z. Guo, C. Zheng, B. Shi, Discrete lattice effects on the forcing term in the lattice Boltzmann method, Phys. Rev. E 65 (2002) 046308.

[115] R. G. M. van der Sman, Galilean invariant lattice Boltzmann scheme for natural convection on square and rectangular lattices, Phys. Rev. E 74 (2006) 026705.

[116] A. J. C. Ladd, Numerical simulations of particulate suspensions via a discretized Boltzmann equation. (Part I & II), J. Fluid Mech. 271 (1994) 285–339.

[117] D. Iwahara, H. Shinto, M. Miyahara, K. Higashitani, Liquid drops on homogeneous and chemically heterogeneous surfaces: A two-dimensional lattice Boltzmann study, Langmuir 19 (2003) 9086–9093.

[118] C. M. Pooley, K. Furtado, Eliminating spurious velocities in the free-energy lattice Boltzmann method, Phys. Rev. E 77 (2008) 046702.

[119] A. J. Briant, J. M. Yeomans, Lattice Boltzmann simulations of contact line motion. II. Binary fluids, Phys. Rev. E 69 (2004) 031603.

[120] S. V. Lishchuk, C. M. Care, I. Halliday, Lattice Boltzmann algorithm for surface tension with greatly reduced microcurrents, Phys. Rev. E 67 (2003) 036701.

[121] R. van der Sman, S. van der Graaf, Emulsion droplet deformation and breakup with lattice Boltzmann model, Comput. Phys. Commun. 178 (2008) 492–504.

[122] T. Roths, C. Friedrich, M. Marth, J. Honerkamp, Dynamics and rheology of the morphology of immiscible polymer blends–on modeling and simulation, Rheol. Acta 41 (3) (2002) 211–222.

[123] H. Zhou, C. Pozrikidis, The flow of suspensions in channels: Single files of drops, Phys. Fluids A 5 (2) (1993) 311–324.

[124] H. Yang, C. C. Park, Y. T. Hu, L. G. Leal, The coalescence of two equal-sized drops in a two-dimensional linear flow, Phys. Fluids 13 (5) (2001) 1087–1106.

[125] A. Zdravkov, G. Peters, H. Meijer, Film drainage and interfacial instabilities in polymeric systems with diffuse interfaces, J. Colloid Interface Sci. 296 (1) (2006) 86–94.

[126] J. Berthier, Microdroplets and Digital Microfluidics, William Andrew Inc., 2008.

[127] M. Latva-Kokko, D. H. Rothman, Scaling of dynamic contact angles in a lattice-Boltzmann model, Phys. Rev. Lett. 98 (25) (2007) 254503.

[128] R. Dreyfus, P. Tabeling, H. Willaime, Ordered and disordered patterns in two-phase flows in microchannels, Phys. Rev. Lett. 90 (2003) 144505.

[129] J. H. Xu, G. S. Luo, G. G. Chen, J. D. Wang, Experimental and theoretical approaches on droplet formation from a micrometer screen hole, J. Membr. Sci. 266 (2005) 121–131.

[130] H. J. Butt, K. Graf, M. Kappl, Physics and Chemistry of Interfaces, Wiley-VCH, 2003.

[131] A. Gupta, R. Kumar, Effect of geometry on droplet formation in the squeezing regime in a microfluidic T-junction, Microfluid. Nanofluid. 8 (6) (2009) 799–812.

[132] L. Wu, M. Tsutahara, L. S. Kim, M. Ha, Three-dimensional lattice Boltzmann simulations of droplet formation in a cross-junction microchannel, Int. J. Multiphase Flow 34 (2008) 852–864.

[133] H. Liu, Y. Zhang, Droplet formation in a T-shaped microfluidic junction, J. Appl. Phys. 106 (2009) 034906.

[134] H. A. Stone, Dynamics of drop deformation and breakup in viscous fluids, Annu. Rev. Fluid Mech. 26 (1994) 65–102.

[135] S. Tomotika, On the instability of a cylindrical thread of a viscous liquid surrounded by another viscous fluid, Proc. R. Soc. London, Ser. A 150 (1935) 322–337.

[136] J. Sjöblom, Emulsions and Emulsion Stability, Taylor & Francis, 2006.

[137] J.-C. Baret, F. Kleinschmidt, A. El Harrak, A. D. Griffiths, Kinetic aspects of emulsion stabilization by surfactants: A microfluidic analysis, Langmuir 25 (11) (2009) 6088–6093.

[138] P. Tabeling, Introduction to microfluidics, Oxford: Oxford University Press, 2005.

[139] U. Sundararaj, C. Macosko, Drop breakup and coalescence in polymer blends - the effects of concentration and compatibilization, Macromolecules 28 (1995) 2647–2657.

[140] P. V. Puyvelde, S. Velankar, J. Mewis, P. Moldenaers, K. U. Leuven, Effect of Marangoni stresses on the deformation and coalescence in compatibilized immiscible polymer blends, Polym. Eng. Sci. 42 (10) (2002) 1956–1964.

[141] L. G. Leal, Flow induced coalescence of drops in a viscous fluid, Phys. Fluids 16 (6) (2004) 1833–1851.

[142] B. Dai, L. G. Leal, The mechanism of surfactant effects on drop coalescence, Phys. Fluids 20 (4) (2008) 040802.

[143] S. Tasoglu, U. Demirci, M. Muradoglu, The effect of soluble surfactant on the transient motion of a buoyancy-driven bubble, Phys. Fluids 20 (4) (2008) 040805.

[144] J. Eastoe, J. S. Dalton, Dynamic surface tension and adsorption mechanisms of surfactants at the air-water interface, Adv. Colloid Interface Sci. 85 (2-3) (2000) 103 – 144.

[145] H. D. Ceniceros, The effects of surfactants on the formation and evolution of capillary waves, Phys. Fluids 15 (1) (2003) 245–256.

[146] M. A. Drumright-Clarke, Y. Renardy, The effect of insoluble surfactant at dilute concentration on drop breakup under shear with inertia, Phys. Fluids 16 (1) (2004) 14–21.

[147] J. Lee, C. Pozrikidis, Effect of surfactants on the deformation of drops and bubbles in Navier-Stokes flow, Comput. Fluids 35 (1) (2006) 43 – 60.

[148] M.-C. Lai, Y.-H. Tseng, H. Huang, An immersed boundary method for interfacial flows with insoluble surfactant, J. Comput. Phys. 227 (15) (2008) 7279 – 7293.

[149] M. Muradoglu, G. Tryggvason, A front-tracking method for computation of interfacial flows with soluble surfactants, J. Comput. Phys. 227 (4) (2008) 2238–2262.

[150] K. N. Premnath, J. Abraham, Simulations of binary drop collisions with a multiple-relaxation-time lattice-Boltzmann model, Phys. Fluids 17 (12) (2005) 122105.

[151] H. Zheng, C. Shu, Y. Chew, A lattice Boltzmann model for multiphase flows with large density ratio, J. Comput. Phys. 218 (1) (2006) 353–371.

[152] T. Lee, P. F. Fischer, Eliminating parasitic currents in the lattice Boltzmann equation method for nonideal gases, Phys. Rev. E 74 (4) (2006) 046709.

[153] J. Huang, C. Shu, Y. Chew, Numerical investigation of transporting droplets by spatiotemporally controlling substrate wettability, J. Coll. Interf. Sci. 328 (1) (2008) 124–133.

[154] P. M. Chaikin, T. C. Lubensky, Principles of Condensed Matter Physics, Cambridge: Cambridge University Press, 2000.

[155] O. Theissen, G. Gompper, Lattice-Boltzmann study of spontaneous emulsification, Eur. Phys. J. B 11 (1) (1999) 91–100.

[156] K. Furtado, C. M. Pooley, J. M. Yeomans, Lattice Boltzmann study of convective drop motion driven by nonlinear chemical kinetics, Phys. Rev. E 78 (2008) 046308.

[157] M. Laradji, H. Guo, M. Grant, M. J. Zuckermann, The effect of surfactants on the dynamics of phase separation, J. Phys. Condens. Matter 4 (1992) 6715–6728.

[158] A. Halperin, P. Pincus, Polymers at a liquid-liquid interface, Macromolecules 19 (1) (1986) 79–84.

[159] B. Cuenot, J. Magnaudet, B. Spennato, The effects of slightly soluble surfactants on the flow around a spherical bubble, J. Fluid Mech. 339 (1997) 25–53.

[160] G. B. McFadden, A. A. Wheeler, On the Gibbs adsorption equation and diffuse interface models, Proc. R. Soc. Lond. A 458 (2021) (2002) 1129–1149.

[161] M. R. Swift, W. R. Osborn, J. M. Yeomans, Lattice Boltzmann simulation of nonideal fluids, Phys. Rev. Lett. 75 (5) (1995) 830–833.

[162] X. Li, R. Shaw, G. M. Evans, P. Stevenson, A simple numerical solution to the Ward-Tordai equation for the adsorption of non-ionic surfactants, Comput. Chem. Eng. In Press.

[163] K. J. Mysels, Diffusion-controlled adsorption on a plane: Non-ideal isotherms, Colloids Surf. 16 (1) (1985) 21 – 29.

[164] Y.-C. Liao, E. I. Franses, O. A. Basaran, Computation of dynamic adsorption with adaptive integral, finite difference, and finite element methods, J. Colloid Interface Sci. 258 (2) (2003) 310 – 321.

[165] Q. Zou, X. He, On pressure and velocity boundary conditions for the lattice Boltzmann BGK model, Phys. Fluids 9 (1997) 1591–1598.

[166] Y. T. Hu, D. J. Pine, L. G. Leal, Drop deformation, breakup, and coalescence with compatibilizer, Phys. Fluids 12 (3) (2000) 484–489.

[167] S. Lyu, T. D. Jones, F. S. Bates, C. W. Macosko, Role of block copolymers on suppression of droplet coalescence, Macromolecules 35 (20) (2002) 7845–7855.

[168] Y. Yoon, A. Hsu, L. Leal, Experimental investigation of the effects of copolymer surfactants on flow-induced coalescence of drops, Phys. Fluids 19 (2) (2007) 023102.

[169] E. van der Zwan, R. van der Sman, K. Schroën, R. Boom, Lattice Boltzmann simulations of droplet formation during microchannel emulsification, J. Colloid Interface Sci. 335 (2009) 112 – 122.

[170] L. Hao, P. Cheng, Lattice Boltzmann simulations of liquid droplet dynamic behavior on a hydrophobic surface of a gas flow channel, J. Power Sources 190 (2009) 435 – 446.

[171] T. Inamuro, T. Ogata, S. Tajima, N. Konishi, A lattice Boltzmann method for incompressible two-phase flows with large density differences, J. Comput. Phys. 198 (2) (2004) 628–644.

[172] T. Lee, C.-L. Lin, A stable discretization of the lattice Boltzmann equation for simulation of incompressible two-phase flows at high density ratio, J. Comput. Phys. 206 (1) (2005) 16 – 47.

[173] Y. Yan, Y. Zu, A lattice Boltzmann method for incompressible two-phase flows on partial wetting surface with large density ratio, J. Comput. Phys. 227 (1) (2007) 763 – 775.

[174] J. J. Huang, C. Shu, Y. T. Chew, Lattice Boltzmann study of droplet motion inside a grooved channel, Phys. Fluids 21 (2009) 022103.

[175] T. Lee, L. Liu, Lattice Boltzmann simulations of micron-scale drop impact on dry surfaces, J. Comput. Phys. 229 (20) (2010) 8045–8063.

[176] P. Lallemand, L.-S. Luo, Theory of the lattice Boltzmann method: Dispersion, dissipation, isotropy, Galilean invariance, and stability, Phys. Rev. E 61 (6) (2000) 6546–6562.